Fabrication of near-ultraviolet light-emitting diodes for white light source applications using fluorescent-silicon carbide

Lin, Li

Publication date:
2018

Document Version
Publisher's PDF, also known as Version of record

Link back to DTU Orbit

Citation (APA):
Lin, L. (2018). Fabrication of near-ultraviolet light-emitting diodes for white light source applications using fluorescent-silicon carbide. Technical University of Denmark.

Fabrication of near-ultraviolet light-emitting diodes for white light source applications using fluorescent-silicon carbide

PhD thesis

Li Lin
林立

October, 2018

DTU Fotonik
Department of Photonics Engineering
Technical University of Denmark

DTU Fotonik
Department of Photonics Engineering

“A journey of a thousand miles begins with a single step.”

– Lao Tzu

Preface

The work presented in this thesis has been carried out as my Ph.D. project in the period of September 1st 2015–October 31st 2018. The work took place at Department of Photonics Engineering (DTU Fotonik), Technical University of Denmark. The project was financed by Innovation Fund Denmark through project “A new type of white light-emitting diode using fluorescent silicon carbide (LEDSiC)” (project No. 4106-00018B). Main supervisor of my Ph.D. project is Dr. Haiyan Ou, Associate Professor at DTU Fotonik, Technical University of Denmark. Co-supervisors are Dr. Flemming Jensen, Associate Professor and Head of Process Engineering at DTU Danchip, Technical University of Denmark and Berit Herstrøm, Process Specialist at DTU Danchip, Technical University of Denmark.

Acknowledgement

During the past three years, I have been working as a Ph.D. student at DTU Fotonik with many wonderful people. I have learned from them and got help from them. Hereby I would like to express my gratitude to them. Without collaboration with them and help from them, this work cannot be completed.

Firstly I would like to express my a lot of gratitude to my main supervisor Prof. Haiyan Ou, who has been supervising me since the first day I started in DTU as a master student, and my co-supervisors Prof. Flemming Jensen and Berit Herstrøm for their patient guidance, powerful support, generous share of knowledge and inspiring suggestions. It has been a great honor for me to have them all to be my supervisors. This is an unforgettable and very beneficial experience in my life.

In addition, I am very grateful to Prof. Yiyu Ou, who was also my co-supervisor when I was a master student. Prof. Yiyu Ou offers not only great help in my research work but also inspiring encouragement as an excellent friend during my Ph.D. study. I have been learning a lot from Prof. Yiyu Ou. Therefore I would like to deliver many thanks to Prof. Yiyu Ou.

Furthermore, I would like to thank Dr. Ahmed Fadil, who was my colleague when I just started my Ph.D. study. He was the person who introduced the fabrication process of LED devices to me and designed the mask that was employed in the lithography process.

Warm gratitude is given to Prof. Meng Liang, Prof. Zhiqiang Liu and Prof. Xiaoyan Yi from Institute of Semiconductors, CAS and Dr. Valdas Jokubavicius, Prof. Mikael Syväjärvi from Linköping University. Thank them for growing good-quality NUV LED epi-wafers and f-SiC wafers for me in the last three years.

Special thanks to all the Danchip staff for the great help they offered whenever I asked for equipment training or advising on processing. Your contribution to my experiments is highly appreciated.

Sincere thanks to all my friends and colleagues. I will remember all the good time we spent together.

Innovation Fund Denmark is acknowledged for the financial support through LEDSiC project.

Last but not least, I would like to express my deepest gratitude to my dearest parents, thank you for your love, trust, support and encouragement. Without these, I couldn’t have enough power to persist and accomplish my study abroad.

PhD. Publication List

Journal articles

1. **L. Lin**, Y. Ou, X. Zhu, E. Stamate, K. Wu, M. Liang, Z. Liu, X. Yi, B. Herstrøm, A. Boisen, F. Jensen, and H. Ou, "InGaN/GaN ultraviolet LED with a graphene/AZO transparent current spreading layer," Optical Materials Express **8**(7), 1818-1826 (2018). (related to the LEDSiC project)

2. **L. Lin**, Y. Ou, V. Jokubavicius, M. Syväjärvi, M. Liang, Z. Liu, X. Yi, P. Schuh, P. Wellmann, B. Herstrøm, F. Jensen, and H. Ou, "An adhesive bonding approach by hydrogen silsesquioxane for silicon carbide-based LED applications," Materials Science in Semiconductor Processing **91**, 9-12 (2019). (related to the LEDSiC project)

3. **L. Lin**, Y. Ou, M. Aagesen, F. Jensen, B. Herstrøm, and H. Ou, "Time-efficient high-resolution large-area nano-patterning of silicon dioxide," Micromachines **8**(1), 13 (2017).

4. K. Guo, **L. Lin**, J. B. Christensen, E. N. Christensen, X. Shi, Y. Ding, K. Rottwitt, and H. Ou, "Broadband wavelength conversion in a silicon vertical-dual-slot waveguide," Optics Express **25**(26), 32964-32971 (2017).

5. K. Guo, J. B. Christensen, X. Shi, E. N. Christensen, **L. Lin**, Y. Ding, H. Ou, and K. Rottwitt, "Experimentally validated dispersion tailoring in a silicon strip waveguide with alumina thin-film coating," IEEE Photonics Journal **10**(1), 1-8 (2018).

Conference contributions

1. **L. Lin**, Y. Ou, X. Zhu, B. Herstrøm, F. Jensen, and H. Ou, "Electroluminescence enhancement for near-ultraviolet light emitting diodes with graphene/AZO-based current spreading layers," 6th International Conference on Light-Emitting Devices and Their Industrial Applications, Kanagawa, Japan (2018). (related to the LEDSiC project)

2. **L. Lin,** F. Jensen, B. Herstrøm, and H. Ou, "Current Spreading Layer with High Transparency and Conductivity for near-ultraviolet light emitting diodes," 5th International Workshop on LEDs and Solar Application, Kgs. Lyngby, Denmark (2017). (related to the LEDSiC project)

3. **L. Lin**, F. Jensen, B. Herstrøm, and H. Ou, "Luminescence enhancement of near ultraviolet light-emitting diodes," Asia Communications and Photonics Conference 2016, Wuhan, China (2016). (related to the LEDSiC project)

4. H. Ou, and **L. Lin**, "A new type of white LED light source by bonding fluorescent SiC and a near-UV LED," 6th International Workshop on Wide Bandgap Semiconductor Materials and Devices, Pingtan, China (2018). (related to the LEDSiC project)

5. Y. Ou, **L. Lin**, P. M. Petersen, and H. Ou, "Enhanced emission from NUV-LED with highly-reflective p-(Al)GaN layer," submitted to the 7th International Conference on Light-Emitting Devices and Their Industrial Applications, Japan (2019).

Abstract

This thesis focuses on the fabrication of a hybrid fluorescent silicon carbide (f-SiC) based warm white light-emitting diode (LED). This type of white LED employs a near-ultraviolet (NUV) LED as the excitation source and a donor-acceptor-pair (DAP) co-doped f-SiC substrate as the wavelength-conversion material. In comparison with the commonly used wavelength-conversion material like phosphors, the f-SiC based white LED does not contain any rare-earth element and has a longer material lifetime.

This work starts with the fabrication of the NUV LED device which functions as the excitation source in the f-SiC based white LED. Then, to enhance the electroluminescence (EL) output of the NUV LED, the work of performance optimization on aluminum-doped zinc oxide (AZO) as a current spreading layer (CSL) is demonstrated. In the end, to produce a hybrid f-SiC based warm white LED, a bonding method for combination of the NUV LED and a nitrogen (N)-boron (B) co-doped f-SiC epi-layer is presented.

To make a NUV LED device, standard post-growth fabrication process including the formation of mesas, CSLs and pads is carried out on NUV LED epi-wafers. In addition, to obtain strong output light of the NUV LED, it is critical to employ a proper CSL with both good conductivity and high transparency in the NUV wavelength region. Therefore, transparent conductive oxide AZO is studied and optimizations are carried out on the

AZO based CSLs. It turns out in the end that a graphene interlayer can improve the performance of the AZO based CSL by decreasing the Schottky barrier height between the CSL and the semiconductor.

On the other hand, to fabricate a hybrid f-SiC based warm white LED by combining the NUV LED and the f-SiC epi-layer, an adhesive bonding approach is employed. Hydrogen silsesquioxane (HSQ) is used as the bonding material due to its high transparency in the NUV wavelength region. By using this method, a NUV LED grown on a 4H-SiC substrate is successfully bonded to a free-standing B-N co-doped f-SiC epi-layer. EL emission from the NUV LED on the top excites the bottom f-SiC epi-layer to generate light finally presenting a warm white emission.

Abstrakt

Denne afhandling fokuserer på fremstilling af en hybrid varm-hvid lysdiode (LED) baseret på fluorescerende silicium karbid (f-SiC). Denne type LED bruger en nær ultraviolet (NUV) LED som excitationskilde og et donor-acceptor par doteret f-SiC substrat som bølgelængekonverteringsmateriale. I sammenligning med almindeligt brugte bølgelængekonverteringsmaterialer som fosforescerende materialer (fosforer), indeholder f-SiC baserede hvide LED'er ikke sjældne jordarter og har længere materialelevetider.

Dette projekt starter med fremstillingen af en NUV LED enhed, der fungerer som excitationskilde i den f-SiC baserede hvide LED. Derefter præsenteres arbejde angående forbedring af elektroluminescence (EL) outputtet af NUV LED enheden. Det består i at indføre og optimere et aluminium doteret zinkoxid (AZO) lag, der virker som et strømspredelag (Current Spreading Layer (CSL)). Til sidste præsenteres en bondemetode, som er brugt til at bonde NUV LED'en og det nitrogen og bor doterede f-SiC epi lag sammen til en hybrid f-SiC baseret varm hvid LED.

Til fremstillingen af NUV LED enheden gennemføres en standard fabrikationsproces, som inkluderer dannelsen af mesa'er, CLS og pad's på NUV LED epi wafere. Udover at forhøje output lysintensiteten af NUV LED enheden er det kritisk at anvende et godt CSL med god ledningsevne og høj transparens. Derfor studeres den transparente elektrisk ledende oxid AZO, og

der optimeres på det AZO-baserede CSL for at reducere Schottky barrierehøjden mellem CSL'et og halvlederen.

Til fremstillingen af den hybride f-SiC baserede varmhvide LED kombineres en NUV LED og et f-SiC epi-lag ved hjælp af en bondemetode. Hydrogen silsesquioxan (HSQ) bruges som bondemateriale pga. dets høje transparens i NUV bølgelængdeområdet. Ved hjælp af denne metode kan en NUV LED, som er groet på et 4H-SiC substrat, bondes til et B-N doteret f-SiC epi-lag. Derved kan EL emission fra NUV LED'en på toppen excitere det nederste f-SiC epi-lag, som så kan generere og udsende varmt hvidt lys.

Table of Contents

Chapter 1 Introduction

Light-emitting diode (LED) light sources possess advantages such as energy saving, robustness, and long lifetime in comparison with the conventional incandescent lamps and fluorescent tubes therefore being expected to become the future market leader [1]. Particularly, white LEDs have attracted extensive attention over the past decades as promising devices and are increasingly popular in many applications of not only general lighting equipment but also backlight source of liquid crystal flat display panels and the headlights of automobiles [2].

Nowadays, the most common commercialized white LED is made by combining a gallium nitride (GaN) based blue LED chip with a coating of yellow phosphor such as cerium-doped yttrium aluminum garnets (YAG) [1-6]. However, the yellow phosphor degrades faster than the blue LED, which turns the white light to be bluish over time hence decreasing the light quality [1]. Also, for this type of white LED, the color rendering index (CRI) is limited by a lack of the red component in the spectrum [3-5]. To obtain an increased CRI, another type of white LED is developed by combining an ultraviolet (UV) LED and phosphors of three colors, which however decreases the emission efficiency by the low efficiency of red phosphors [2-4]. Furthermore, most of the white LEDs described above contain rare-earth elements [1, 4]. Hence, the utility of these white LEDs is limited by the phosphor performance and the decreased abundance of rare-earth elements.

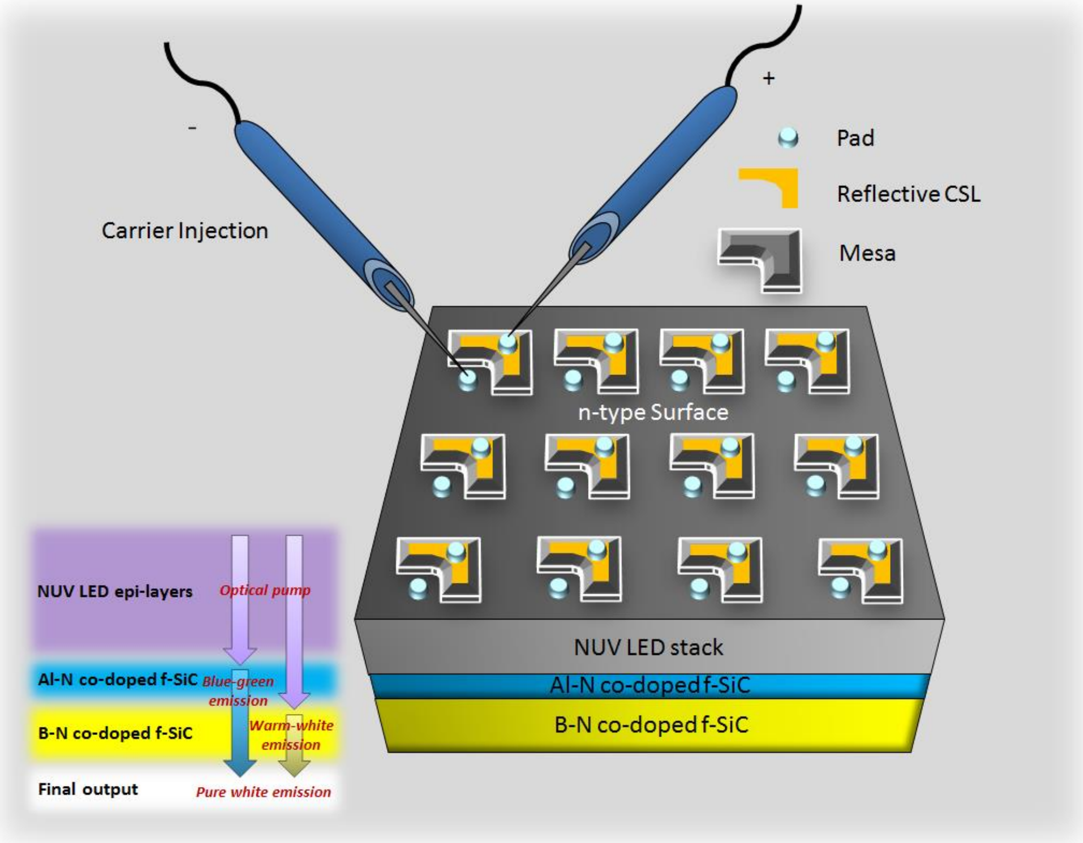

Figure 1.1 Schematic illustration of a novel monolithic f-SiC based white LED

As a promising alternative method, a novel monolithic fluorescent silicon carbide (f-SiC) based white LED is invented by Kamiyama [2-4]. The f-SiC possesses advantages such as high thermal conductivity and ability to cover the entire visible spectral range. In addition, the f-SiC based white LED is rare-earth element free and contains no decaying phosphors.

A schematic illustration of this type of LED is shown in Figure 1.1. As shown, a near-ultraviolet (NUV) LED stack is grown on f-SiC epi-layers. The NUV LED on the top functions as an excitation source while the f-SiC epi-layers work as wavelength convertors. By post-growth processing including mesa and contact fabrication on the NUV LED, a highly reflective current spreading layer (CSL) is produced on the top, which can reflect most of the NUV photons generated in the active multiple quantum wells (MQWs) and make the reflected photons propagate to the f-SiC epi-layers. Due to the large optical bandgap of SiC, its emission wavelength can be designed and altered within the entire visible spectrum by introducing different dopants. One of the f-SiC epi-layers is co-doped by Nitrogen (N) and Boron (B) while the other one is co-doped by N and Aluminum (Al). Through excitation of NUV photons from the LED on top, a warm white light with a peak wavelength at around 580 nm is generated from the N-B co-doped f-SiC epi-layer due to its donor-acceptor-pair (DAP) luminescence [1-4]. Simultaneously, a blue-green emission with a peak wavelength at around 485 nm is generated from the N-Al co-doped f-SiC epi-layer. Combination of the warm white and blue-green emissions can result in a pure white light. For this new type of white LED, a device lifespan around 300,000 hours can be expected, which is much longer than that of the typical phosphor-based white LED (50,000 hours) [5]. In addition, its value of color rendering index (CRI) could exceed 90 [5, 7]. The luminous efficacy could reach as high as 130 lm/W which is higher than that of incandescent lamps (approximately 10 lm/W) and fluorescent lamps (typically 80 lm/W) [5, 8].

Except for the monolithic method, there is another way, i. e. the hybrid method, to realize the f-SiC based white LED. The focus of this thesis is on the fabrication of a hybrid f-SiC based warm white LED. A schematic diagram of technical steps to realize the f-SiC based white LEDs is shown in Figure 1.2. There are primarily four steps.

In Step 1, epi-layers of warm white emission B and N co-doped f-SiC and blue emission Al and N co-doped f-SiC are grown [1, 2]. The idea is to first grow 200 µm B-N co-doped f-SiC epi-layer on a 6H-SiC substrate by a fast sublimation growth process followed by the growth of a 50 µm Al-N co-doped f-SiC epi-layer on top. After growth, the 6H-SiC substrate is polished away to produce the f-SiC substrate. Intense warm white emission from B and N co-doped 6H-SiC has been demonstrated by the joint effort of DTU Fotonik, Linköping University, and University of Erlangen-Nürnberg through the NORLED project [1, 9]. The f-SiC epi-layers with B and N dopants can be grown on 6H-SiC (0001) substrates with 1.4 degree off-orientation in the [1120] direction under a growth temperature of 1725℃ [9, 10]. Intense DAP band emission can be obtained by B and N concentrations larger than 10^{18} cm^{-3} with a peak wavelength at 587 nm and a full width at half maximum (FWHM) of 120 nm [9, 10]. Growth of N and Al co-doped 6H-SiC using liquid solution phase epitaxial technology and fast sublimation growth process is still under research.

In Step 2, GaN based high-efficiency NUV LED epi-layers are grown through metalorganic chemical vapor deposition (MOCVD) on commercial sapphire and SiC substrates by Institute of Semiconductors, Chinese Academy of Science. After growth, these epi-wafers are used for experiments described in Step 3 and Step 4.

The work of this thesis is involved in Step 3 and Step 4.

In Step 3, there are two main focuses. Firstly, post-growth fabrication process is carried out on NUV LED epi-wafers and it includes the formation of mesas, CSLs and pads. The purpose is to fabricate standard NUV LED devices as a starting point. After the fabrication of standard NUV LED devices, characterizations regarding the optical and electrical performance are carried out before the further optimization.

Secondly, in Step 3, performance optimization on the NUV LED device by employing a transparent conductive oxide material instead of the conventional CSL is carried out. To enhance the output light of the NUV LED device, it is critical to employ a proper CSL with both good conductivity and high transmittance. In this work, efforts are made to find an alternative candidate with high transmittance in the NUV wavelength region to replace the conventional absorbing CSL. Also, improvement on the I-V and electroluminescence (EL) performance of the NUV LED with the transparent conductive oxide CSL is carried out.

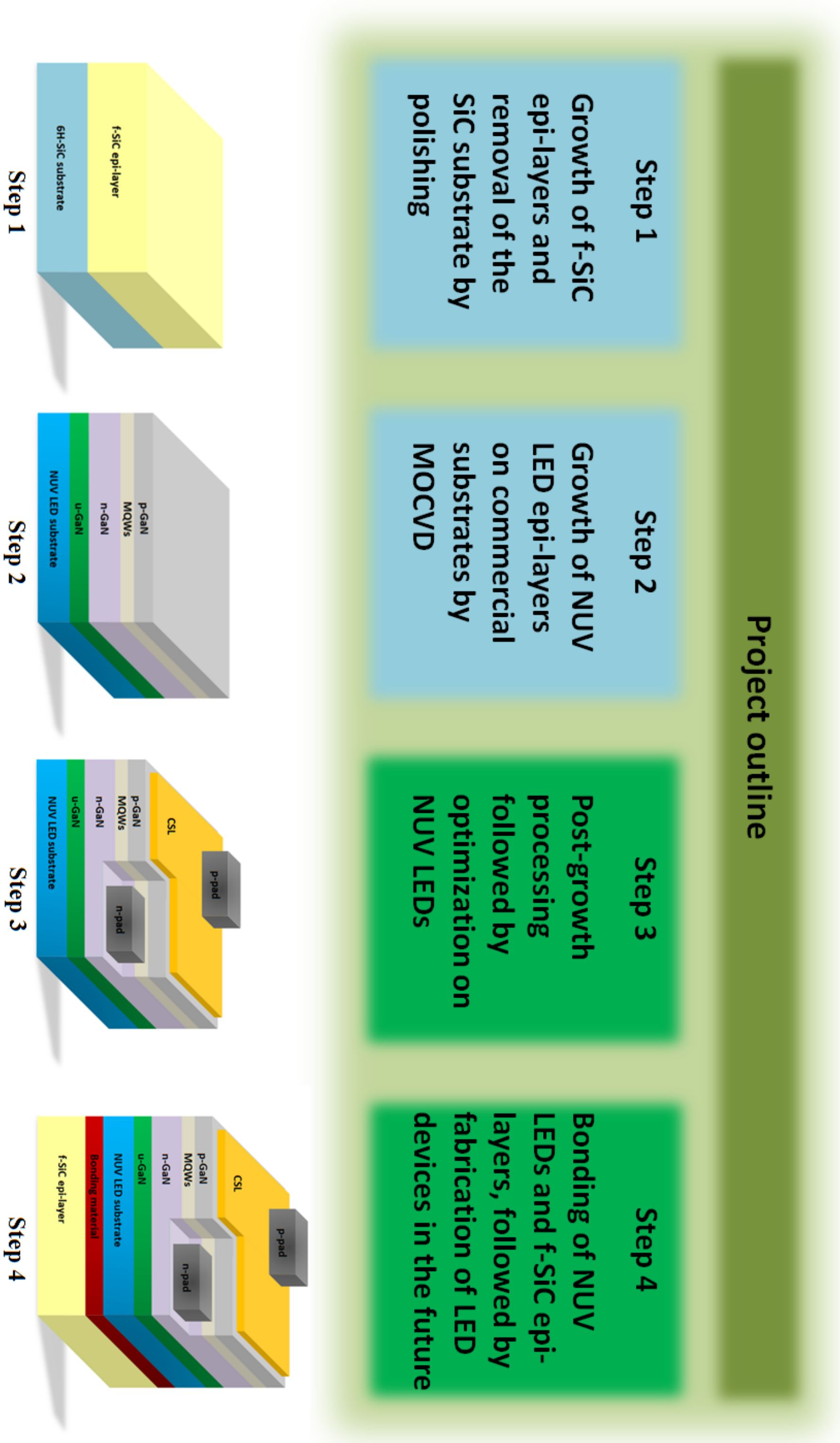

Figure 1.2 Schematic diagram of technical steps to realize hybrid f-SiC based white LEDs (The work of this thesis is involved in Step 3 and Step 4)

In Step 4, the objective is to fabricate a hybrid f-SiC based LED. In this work, an NUV LED epi-wafer and an f-SiC epi-layer are combined through a bonding process. Afterwards, characterizations are carried out regarding bonding quality and EL performance of the hybrid f-SiC based LED. In the future, after bonding, LED devices can be fabricated on the bonded sample by the standard fabrication processes of mesas, CSLs and pads.

In summary, to realize the fabrication of a hybrid f-SiC based warm white LED, the work includes post-growth processing of NUV LED devices followed by performance optimization of the transparent conductive aluminum-doped zinc oxide (AZO)-based CSLs and finally the bonding of the hybrid f-SiC based LED. The structure of the thesis is briefly explained below.

Chapter 2 demonstrates a standard fabrication process of NUV LED devices, which primarily consists of mesa fabrication, CSL fabrication and pad fabrication. Section 2.1 starts with the history and the development of GaN-based NUV LEDs followed by a brief introduction of its MOCVD growth as well as the state-of-the-art of NUV LEDs. In section 2.2, a standard fabrication process of NUV LED devices is presented in detail followed by optimizations on the adhesion of the metal n-pads. Section 2.3 demonstrates characterization results of the fabricated NUV LED device with the conventional Ni/Au CSL regarding I-V characteristics, EL, transfer line method (TLM) test as well as transmittance. Section 2.4 discusses some of the challenges that can affect the NUV LED performance followed by a summary of this chapter in section 2.5.

Chapter 3 studies a transparent conductive CSL material AZO as CSLs on NUV LED devices. In section 3.1, the NUV LED device with the commonly used transparent conductive indium tin oxide (ITO) CSL is fabricated followed by characterizations and comparisons with the AZO CSL. In section 3.2, NUV LED devices with different AZO-based CSLs are fabricated and compared regarding I-V characteristics, EL and CSL transmittance. Section 3.3 proposes an approach to further improve the performance of the AZO-based CSL by employment of a graphene interlayer. Relevant characterization results are demonstrated and discussed. Conclusions of this chapter are drawn in section 3.4.

Chapter 4 demonstrates an approach of bonding an NUV LED to a B-N co-doped f-SiC epi-layer. By doing so, a hybrid f-SiC based LED can be obtained. In section 4.1, fundamental information regarding adhesive bonding including basic mechanisms and advantages is introduced. Section 4.2 presents the method of hydrogen silsesquioxane (HSQ) adhesive bonding including tests on Si and SiC samples followed by the bonding of an NUV LED to a B-N co-doped f-SiC epi-layer. Afterwards, characterization results regarding HSQ transparency, bonding quality and EL of the hybrid LED are demonstrated and discussed in section 4.3. At the end, section 4.4 summarizes the results of this chapter.

Chapter 5 summarizes the work in this thesis, mainly regarding the standard post-growth processing on NUV LED epi-wafers, transparent conductive AZO-based CSLs and bonding of the NUV LED and the f-SiC epi-layer. At the end an outlook on future research work is presented.

Chapter 2 Fabrication of gallium nitride based near-ultraviolet light-emitting diodes

In this chapter, basics regarding GaN based NUV LEDs and its standard fabrication process are demonstrated. Afterwards, characterizations on the fabricated NUV LEDs are carried out followed by discussion on challenges that can affect the NUV LED performance.

2.1 Near-ultraviolet light-emitting diodes

UV LEDs are LEDs that can generate emissions with wavelengths shorter than 400 nm. They are promising alternatives for UV lamps and they are also attractive candidates in various applications including lighting and displays, microscopy, lithography technology, resin curing, medicine, biotechnology and environmental monitoring [11-17]. According to the spectral ranges of emission, they can be divided into NUV LEDs (300–400 nm) and deep ultraviolet (DUV) LEDs (200–300 nm) [17]. In this work, NUV LEDs, which can be used as the excitation source in the f-SiC based LED, are studied.

2.1.1 History and development

The development of semiconductor emitters began from the 20th century when there had been several reports on EL from some materials including SiC [18]. In the 1960s, the first blue LED made from SiC was fabricated and it became commercially available in the 1990s although it was not viable and had a low efficiency of around 0.03% [19, 20]. Meanwhile, in the late 1950s, researchers were making visible LEDs using III-V compounds and in 1964, the green GaP LED was produced with an efficiency of 0.6% [21]. The indirect bandgaps of SiC and GaP limit their efficiencies, since a phonon needs to get involved in the hole-electron recombination process due to momentum conservation [18].

Figure 2.1 displays bandgaps and lattice constants of semiconductors. The connecting lines stand for their ternary compounds, with different ratios of the relevant binary materials. As shown in the figure, nitride materials with wurtzite structures possess direct bandgaps ranging from 0.8 to 6.3 eV, which makes themselves capable of emissions covering a wide spectrum hence becoming attractive in optoelectronic applications as semiconductor emitters.

In the 1960s, the growth of single crystal films of GaN had become a promising technology and it succeeded in 1968 [22]. At that time, infrared, red, and green LEDs had been successfully made except for the LEDs emitting shorter wavelengths. The wide bandgap of GaN makes itself an attractive material in the application of short wavelength emission, including the blue emission which can make flat panel televisions possible and end the era of the venerable cathode ray tube [18].

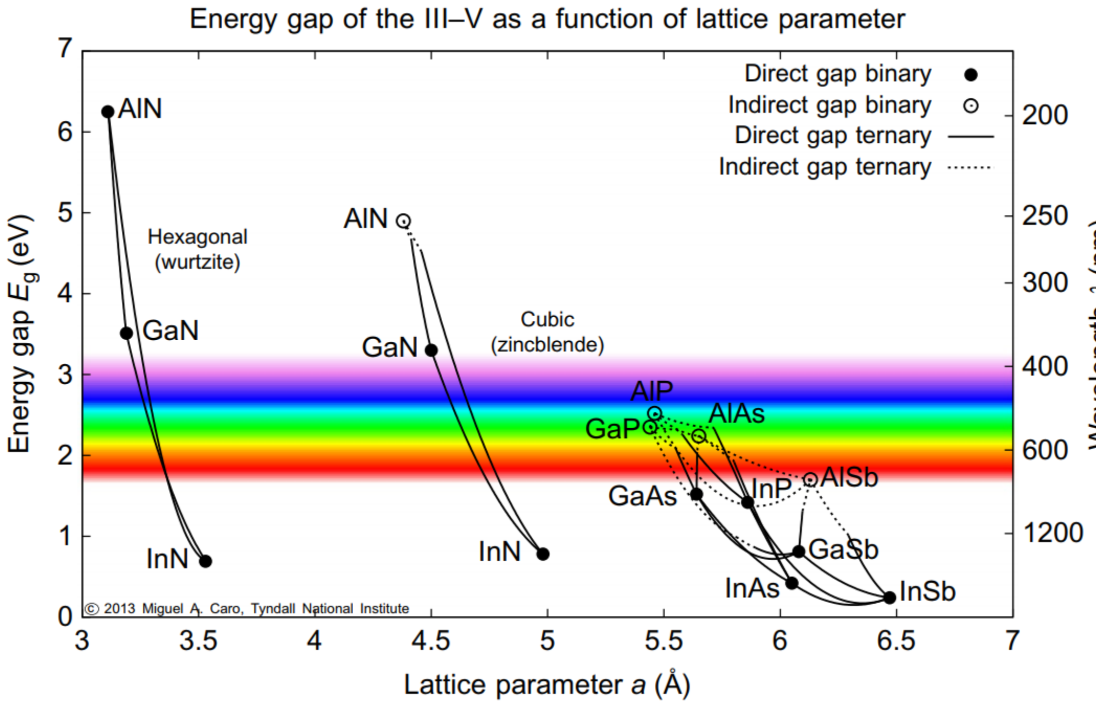

Figure 2.1 Energy gap of the III-V as a function of lattice parameter [23]

In the beginning, the grown GaN films had always been n-type until 1971 when the Zn-doped p-GaN emerged hence allowing the production of the first GaN LED [18, 24]. In the next two years, GaN LEDs with Mg-doped p-GaN emitting blue/violet light were successfully made [25, 26]. However, it was always difficult to obtain efficient emissions from a GaN active layer at room temperature [27]. Fortunately, group-III nitrides composed of GaN and its alloys InN or AlN have revolutionized the solid-state lighting market due to their ability to realize efficient emissions in a wide visible spectral range including NUV [27, 28]. Growth of high-quality InGaN films first succeeded in 1992 [29]. The addition of small amounts of indium to GaN enables strong band-to-band emission at room temperature. By altering the indium composition in InGaN, band-to-band emission ranging from green to UV can be obtained [27]. Soon, Nakamura et al. fabricated the first InGaN/GaN double-heterostructure LED in 1993 followed by the growth of InGaN MQW structure [30]. In 1995, Nakamura et al. developed the first blue/green InGaN single quantum well (SQW) structure LEDs [31]. Afterwards, the UV LED using the InGaN active layer was also produced [32, 33].

2.1.2 MOCVD epitaxial growth

In 1984, Kawabata et al. at Matsushita reported the first blue GaN LED grown by MOCVD [18]. Nowadays, MOCVD has become an extensively employed technique in the manufacture of optoelectronics including GaN-based LEDs [35-39].

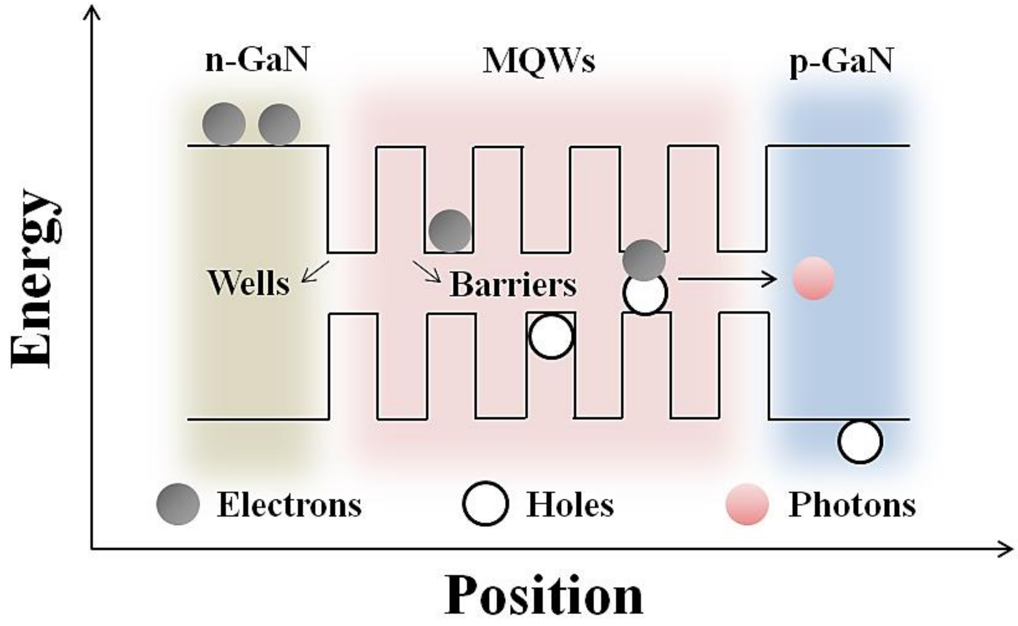

Figure 2.2 Fundamental elements of a light- emitting diode

As shown in Figure 2.2, fundamentally, the structure of a NUV LED contains an n-GaN layer, MQWs and a p-GaN layer as the main elements. By injection of holes and carriers through p-GaN and n-GaN, respectively, radiative carrier recombination and photon generation processes take place in the active MQWs. The active layer in MQWs can be either $Al_xGa_{1-x}N$ or $In_xGa_{1-x}N$. Usually, $Al_xGa_{1-x}N$ is employed for emission of wavelengths smaller than 380 nm while $In_xGa_{1-x}N$ can cover the entire visible range through tuning the content of indium. For GaN, InGaN, and AlGaN epitaxial growth, precursors of Ga, N, In and Al are normally trimethylgallium (TMG), Ammonia (NH_3), trimethylindium (TMIn) and trimethylaluminum (TMA), respectively [38, 39]. When growing the MQWs, the mismatch of lattice constants between the GaN barrier and the $In_xGa_{1-x}N$ or $Al_xGa_{1-x}N$ well can result in an internal strain. The strain in different material layers induces piezoelectric fields which can affect the internal quantum efficiency (IQE) of the LED.

Generally, in n- and p-GaN layers, atoms of Si are used as the n-type dopants while Mg as the p-type dopants, respectively. Normally, Monosilane (SiH_4) is used for n-type doping by Si and bis-cyclopentadienyl magnesium (Cp_2Mg) is used for p-type doping by Mg. The standardly used doping concentration of Mg has to be sufficiently high in order to produce a reasonable conductivity since Mg has a relatively high activation energy (around 150 meV) therefore limiting the doping efficiency [40, 41].

The substrates used for MOCVD growth can also affect the quality of the epi-layers grown on the top. Generally, sapphire and SiC have been widely employed for the epitaxial growth of III-V nitrides. GaN-based light-emitting diodes grown on sapphire substrates, assisted with a thin buffer layer of AlN or GaN, can present a good luminescence capacity. However, sapphire also possesses some disadvantages including a lattice mismatch of 14% between GaN and itself [42], which can result in a dense threading dislocation in the grown films. Also, its large thermal expansion coefficient and low thermal conductivity could degrade the quality of GaN films [43]. As for the SiC substrate, although its MOCVD growth technology of NUV LED epi-layers is not as mature as that of the sapphire substrate, it has also become increasingly attractive due to its advantages. In comparison with the sapphire substrate, the SiC substrate possesses a smaller lattice mismatch (4%) hence allowing fewer dislocations generated during GaN growth [42]. Furthermore, more than 10 times better thermal conductivity of SiC [43] than that of the sapphire makes SiC a promising material in high power related applications. Generally speaking, both sapphire and SiC substrates have their merits and the specific needs of an application determine which kind of substrate to employ.

2.1.3 State-of-the-art

The performance of LEDs can be evaluated by IQE (the ratio of photons internally emitted from the MQWs divided by the carriers injected into the LED), light extraction efficiency (LEE) (the ratio of photons externally emitted from the device divided by the photons internally emitted from the MQWs) and external quantum efficiency (EQE) which is defined as the product of the IQE and the LEE (the ratio of photons externally emitted from the device divided by the carriers injected into the LED). Therefore, to obtain a high EQE, both the IQE and LEE should be optimized [44].

To have a high IQE, the amount of hole-electron nonradiative recombination happening at defects and nonradiative Auger recombination should be minimized. It can be improved by modifying the crystal quality and reducing the defect density during growth. Currently the highest IQE is 80% for blue LEDs at a current density smaller than 30 A/cm^2) [44]. However, the IQE of NUV LEDs is much lower than those of green and blue LEDs. This can be explained by the low indium content in the composited wells and barriers of a NUV LED, which leads to a small band-offset. So it is easy for the injected carriers to escape from the active region hence resulting in a limited IQE [45, 46]. For example, the IQE of the NUV LED epi-wafers employed in this work is around 25%.

The refractive index difference exists at the LED/air interface makes a considerable fraction of generated photons in the device easily get trapped due to total internal reflection consequently limiting the LEE [44]. To improve the LEE, surface roughening technologies have been extensively studied [47]. The mechanism of surface roughening technologies is to increase the sidewall surface hence providing more pathways and more chances for photons to hit the interface in an almost perpendicular direction therefore minimizing the total internal reflections. In addition, by the employment of photonic crystals [48], patterning of substrates [49] et al. [50, 51], the LEE of the LED can also be increased.

Although there has been a great development in the NUV LED industry, further optimizations are still in need. In this chapter, basics regarding the NUV LED fabrication and the characterizations are introduced first followed by the performance improvement in the next chapter. In the following section 2.2 and 2.3, a standard fabrication process is demonstrated in detail including formations of mesas, CSLs and pads. Afterwards, characterizations on I-V characteristics, EL, ohmic property and transmittance are carried out and the results are demonstrated. In the end, challenges that can affect the performance of an NUV LED are discussed.

2.2 Fabrication process

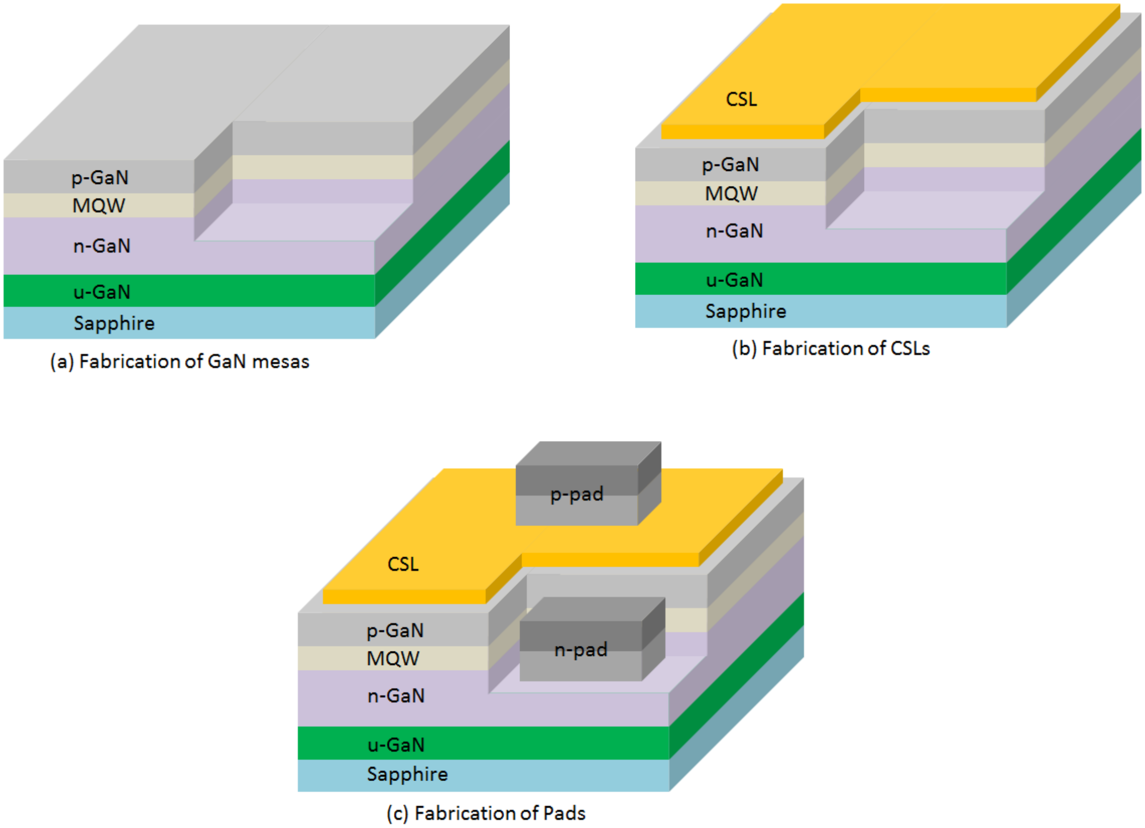

(a) Fabrication of GaN mesas

(b) Fabrication of CSLs

(c) Fabrication of Pads

Figure 2.3 Fundamental fabrication steps of NUV LED devices

As shown in Figure 2.3, there are mainly three steps in the standard fabrication process of a NUV LED device. The fundamental structure of an NUV LED epi-wafer includes an n-GaN layer normally with a thickness around 2-3 µm covered by several periods (normally 8-10 periods) of MQWs (InGaN/GaN MQWs) as the active layer which generates photons. A p-GaN layer is on top of the MQWs with a thickness generally around 100-150 nm. During the fabrication, firstly, GaN mesas are produced on the NUV epi-wafer in order to expose the n-GaN layer. Secondly, current spreading layers are produced on the p-GaN surface to avoid current crowding due to the resistive p-GaN so as to spread out the electric current uniformly. In the end, n- and p-pads are added to the n-GaN and p-GaN surfaces, respectively, for electric current injection. A more detailed fabrication process is introduced in the following section.

2.2.1 Fabrication of mesas

The purpose of making mesas is to expose the n-GaN for the subsequent formation of the n-pad so that the holes and electrons can be injected through the p-GaN and the n-GaN, respectively. The basic structure of the NUV epi-wafer employed in this work, which is grown by the MOCVD CRUIS I (AIXTRON, Herzogenrath, Germany), includes a 2.5 µm n-GaN layer (doping concentration of $1.5\times10^{19}cm^{-3}$) covered by 9 periods of InGaN/GaN MQWs and a 130 nm p-GaN layer (doping concentration of $2\times10^{19}cm^{-3}$) on the top. On the p-GaN, there is a highly Mg doped p^{+}-GaN layer with a thickness of 15 nm and a doping concentration of $2\times10^{20}cm^{-3}$. The standard fabrication steps of GaN mesas are shown in Figure 2.4.

Figure 2.4 (a)-(d) demonstrate the fabrication steps of resist mesas. During the fabrication, firstly, a layer of 300 nm SiO_2 is deposited on the NUV LED sample by plasma-enhanced chemical vapor deposition (PECVD). Then, 1.6 µm positive AZ5214E photoresist is spun on the top of the sample followed by baking on a hotplate at 90 ℃ for 90 seconds to drive out the solvent. Afterwards, the AZ5214E photoresist is exposed by UV light through a mask with mesa patterns at an intensity of 13 mW/cm^2 for 10 seconds. During the exposure, chain-scission happens in the exposed areas of AZ5214E and makes the exposed AZ5214E become soluble in the developer. After development in

AZ 726 MIF (2.38% TMAH in water) for 30 seconds, the exposed AZ5214E is resolved hence producing resist mesas on the SiO_2 layer.

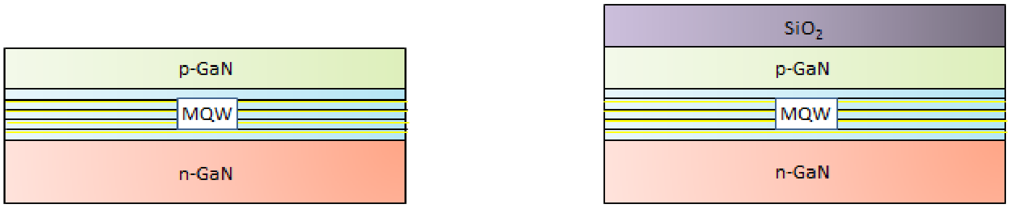

(a) NUV epi-wafer

(b) SiO_2 deposition by PECVD

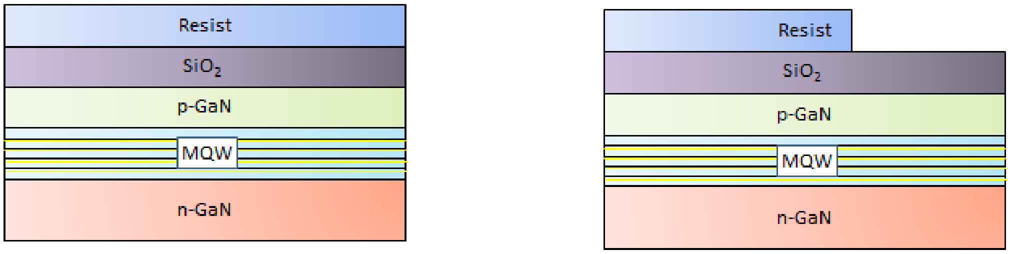

(c) Spin-coating of AZ5214E

(d) Lithography of mesas

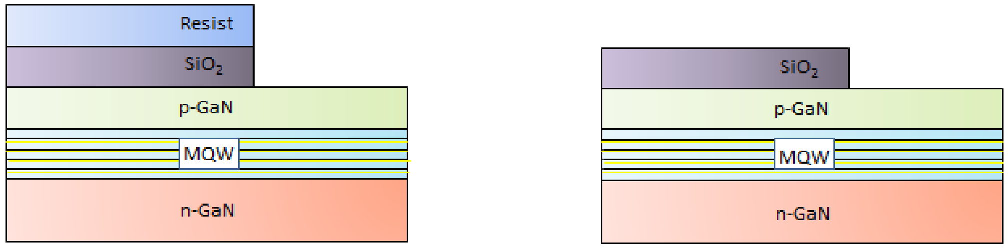

(e) BOE etch of SiO_2

(f) Removal of AZ5214E

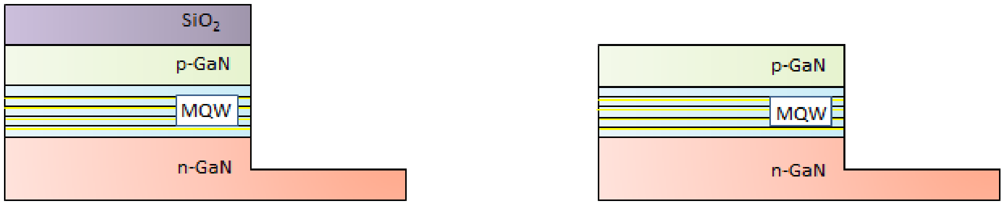

(g) ICP etch of GaN

(h) Removal of SiO_2

Figure 2.4 Standard fabrication steps of GaN mesas

Figure 2.4 (e) and (f) demonstrate the fabrication steps of SiO_2 mesas. After the formation of the resist mesas, the sample is immersed in buffered oxide etch (BOE), which consists of NH_4F : HF = 87.5% :12.5%, for 2 minutes to etch the exposed SiO_2 in order to transfer the mesa structures from the resist layer to the SiO_2 layer. After SiO_2 etch, the AZ5214E resist is removed using oxygen plasma at a power of 100 W for 20 minutes leaving only SiO_2 mesas on the p-GaN. The SiO_2 mesas function as masks in the following dry etch of the GaN mesas.

Figure 2.4 (g) and (h) demonstrate the fabrication steps of GaN mesas. The dry etch of GaN is carried out by inductively coupled plasma (ICP) etching using Cl_2 and BCl_3. An etch depth of 1.4 µm is achieved to expose the n-GaN layer. Then, the SiO_2 is removed by immersion in 5% hydrofluoric acid (HF) for 10 minutes leaving only GaN mesas on the NUV LED sample. In the end, the LED sample with mesas is annealed by a RTA process in N_2 at 500 ℃ for 10 minutes followed by passivation in 37% hydrogen chloride (HCl) for 1 hour [52].

2.2.2 Fabrication of current spreading layers and pads

The standard fabrication steps of CSLs and pads on the NUV LED sample with GaN mesas are demonstrated in Figure 2.5. CSLs can help the LED avoid the current crowding effect so as to obtain a more uniform carrier distribution when holes are injected into p-GaN layer. In this section, a standard Ni/Au CSL is employed. The Ni/Au is a conventional CSL and has been widely used in the LED application due to its excellent electrical properties [53].

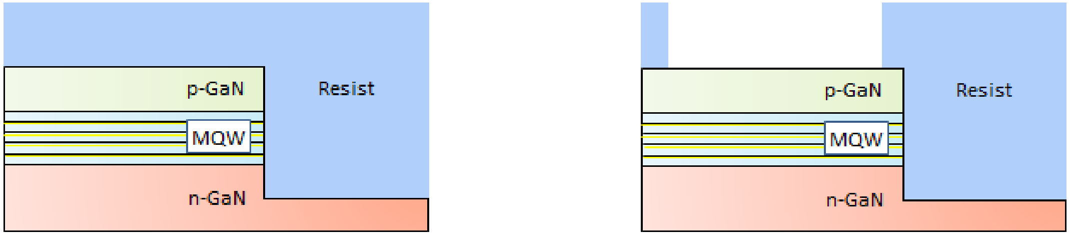

(a) Spin-coating of n-Lof 2020 (b) Lithography of CSLs

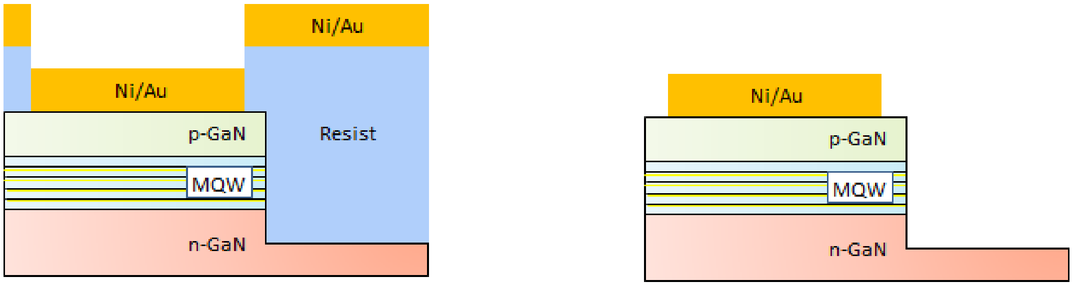

(c) Deposition of Ni/Au (d) Ni/Au Liftoff

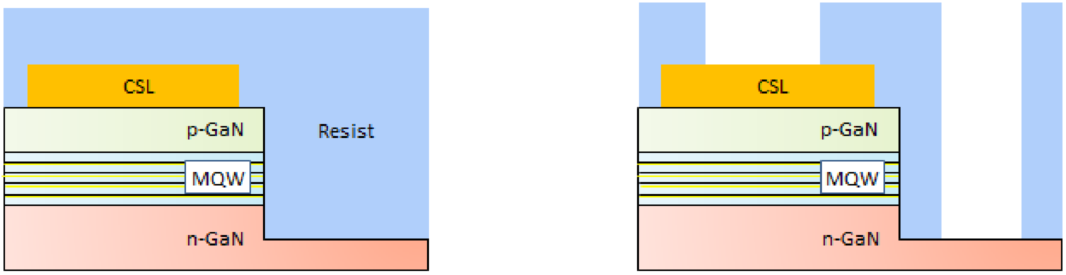

(e) Spin-coating of n-Lof 2020 (f) Lithography of pads

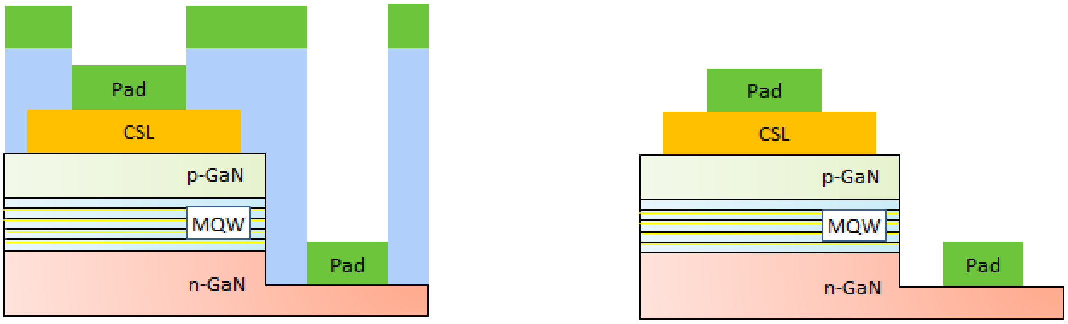

(g) Deposition of Ti/Au (h) Ti/Au Liftoff

Figure 2.5 Standard fabrication steps of CSLs and pads

Figure 2.5 (a)-(d) demonstrate the fabrication steps of standard Ni/Au CSLs. Firstly a layer of 2 μm negative N-LOF 2020 photoresist is spun on the LED sample followed by baking on a hotplate at 110 ℃ for 1 minute to drive out the solvent. Afterwards, the N-LOF 2020 is exposed by UV light through a mask with CSL patterns at an intensity of 13 mW/cm^2 for 10 seconds followed by baking at 110 ℃ for 1 minute. Cross-linking happens in the exposed areas of N-LOF 2020 hence becoming insoluble in the developer. Then the sample is developed in AZ 726 MIF for 30 seconds to resolve the unexposed N-LOF 2020 hence leaving openings for the following deposition of CSL materials. Afterwards, 10 nm Ni and 40 nm Au layers are e-beam evaporated. Then, lift-off in MICROPOSIT Remover 1165 is carried out for 15 minutes assisted with ultrasonic to remove the resist together with the CSL materials on the top. Finally, 10 nm Ni/ 40 nm Au CSLs are formed on the p-GaN surfaces of the GaN mesas.

Figure 2.5 (e)-(h) show the fabrication steps of the p- and n-pads. The materials of the p- and n-pads are identical and the process is similar to the one of CSLs but with two differences. One of the differences is that the mask employed for exposure is with patterns of pads. In addition, the evaporated materials are 30 nm (Titanium) Ti and 200 nm Au, which are also standard materials used as pads in the LED application [54]. After lift-off, the 30 nm Ti/ 200 nm Au p- and n-pads are formed on the p-GaN and the n-GaN surfaces, respectively.

Figure 2.6 shows a scanning electron microscope (SEM) image of an NUV LED device after the standard fabrication process and the dimensions of the device are also shown in micrometer scale. The SEM images in this work are inspected by a Supra 40 VP SEM (Zeiss, Oberkochen, Germany) at 5 kV. The previously described standard fabrication process of the LED device is widely used in both the LED scientific research as well as the LED industry [55]. More details of the fabrication process are demonstrated in Appendix A.

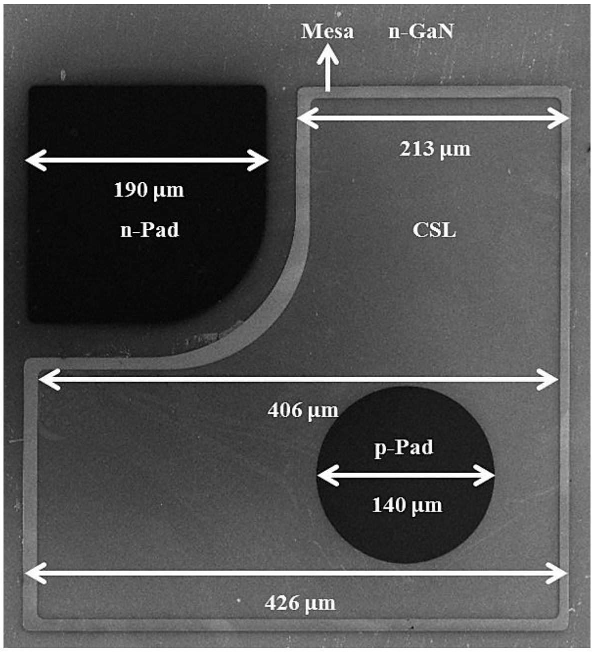

Figure 2.6 SEM image of a fabricated NUV LED device

2.2.3 Optimization of the fabrication process

Before the process described in Figure 2.4, the fabrication of the SiO_2 mesas is carried out using a RIE process instead of the BOE one. However, with the employment of the RIE process of SiO_2, severe peeling-off of n-pads can happen during the liftoff. The peeling-off of the n-pads significantly deteriorates the yield of the LED devices. In the following section, the explanation and the optimization regarding this issue are demonstrated.

Figure 2.7 and Figure 2.8 show SEM images taken from the fabricated NUV LED devices assisted with a RIE process of SiO_2 instead of a BOE one. As shown in Figure 2.7, some of the n-pads are damaged while some are completely missing leaving only the marks on the LED sample. This happens during the lift-off of the p- and n-pads. Figure 2.8 shows the surface of the n-GaN where an n-pad is deposited and then flakes off during the lift-off. It shows many undesired small structures with heights around 100-500 nm on the n-GaN. The heights of the small structures are comparable to the 230 nm thick pads and therefore could probably affect the adhesion of the n-pads to the n-GaN.

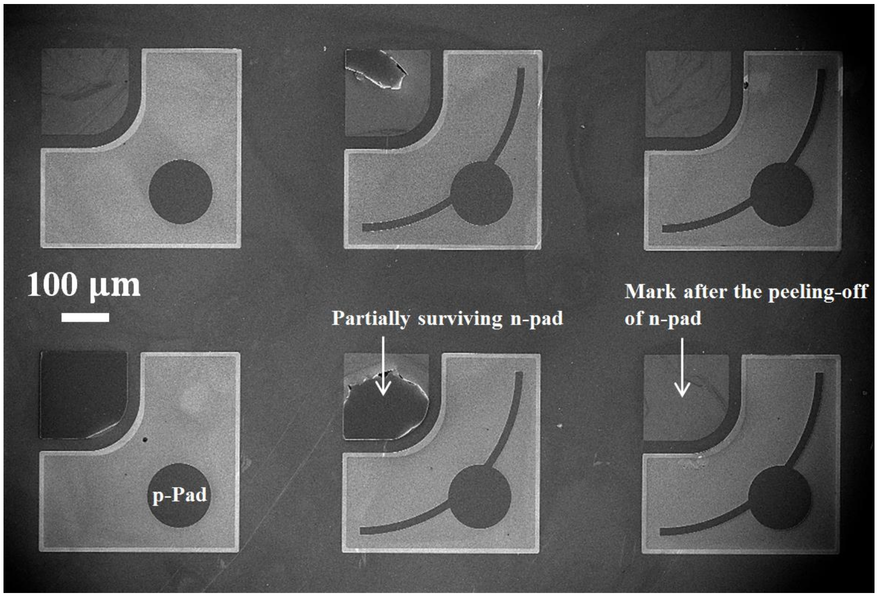

Figure 2.7 SEM image showing peeling off of n-pads after liftoff

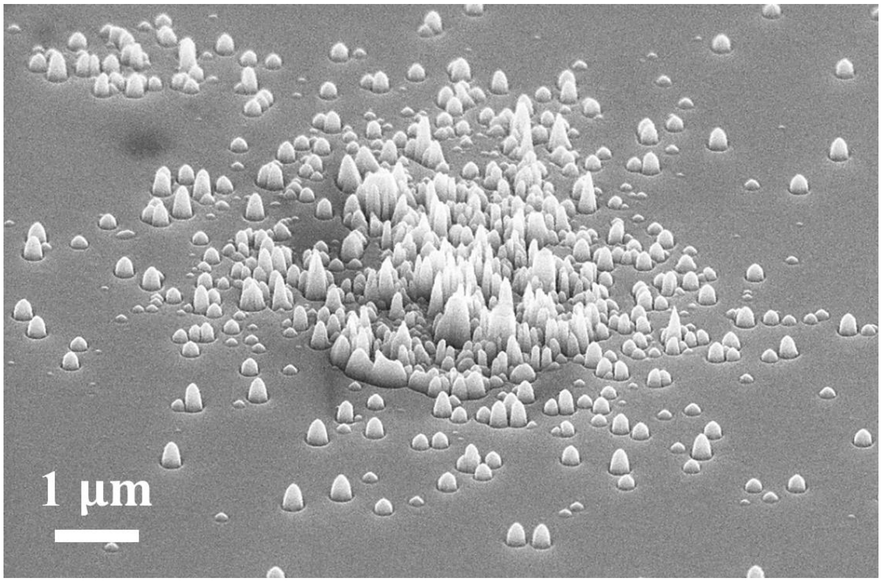

Figure 2.8 SEM image showing undesired structures on the n-GaN

The formation of the undesired small structures on the n-GaN surface is schematically illustrated in Figure 2.9 (a)-(c). During the RIE dry etch of the SiO_2, the areas of mesas are protected by AZ5214E. The AZ5214E can also be sputtered by the plasma hence leaving undesired resist on the exposed SiO_2 surface to be etched. This induces a micro-masking effect leaving undesired

SiO_2 structures on the GaN surface to be etched after removal of the AZ5214E. Afterwards, the ICP etch of GaN transfers the SiO_2 structures to the n-GaN layer hence producing the undesired small GaN structures.

An approach to avoid the micro-masking effect resulting from the sputtering of the AZ5214E during RIE is to employ a wet SiO_2 etching process instead of the RIE dry etch, as described in the fabrication process shown in Figure 2.4. With the optimization on the etch method of SiO_2, the yield of the n-pads is significantly increased. As shown in Figure 2.10, all of the n-pads survive after the lift-off.

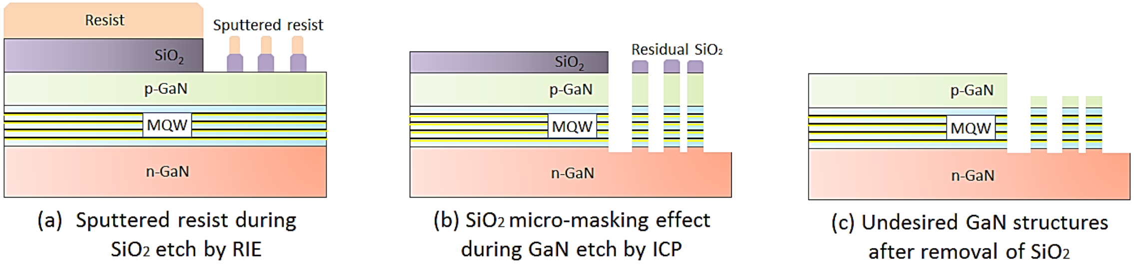

Figure 2.9 Schematic illustration of the formation of undesired structures on n-GaN

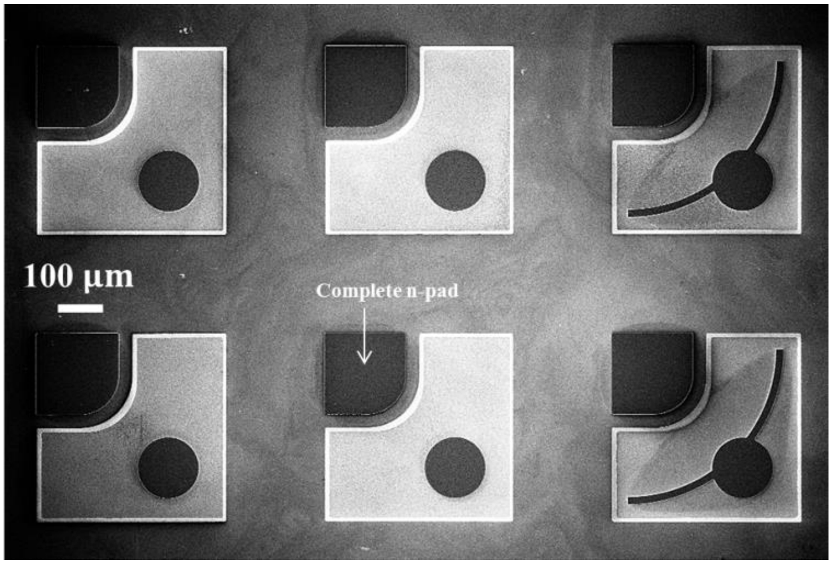

Figure 2.10 SEM image showing the fabricated NUV LED devices with a higher yield

2.3 Characterizations

After fabrication, optical and electrical properties of the fabricated NUV LED device are characterized. The results are demonstrated as below.

EL of the NUV LED device

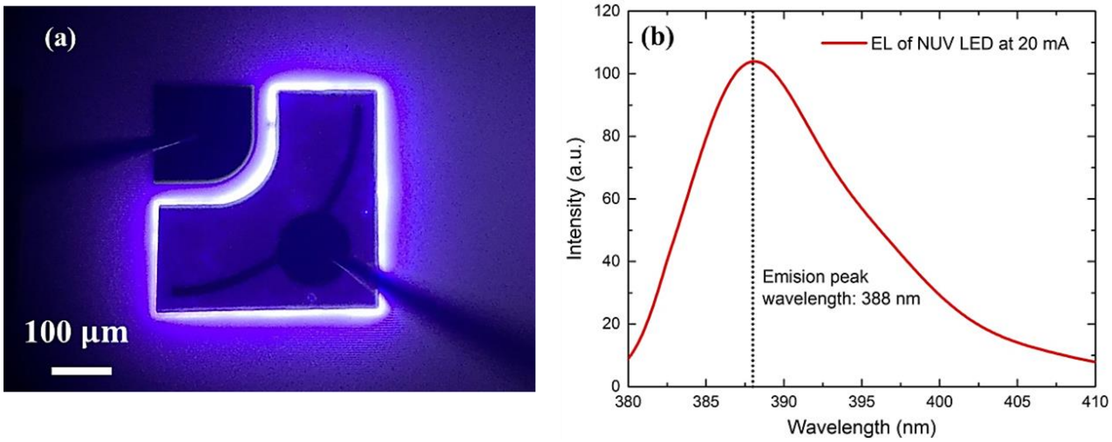

Figure 2.11 (a) Photograph of the NUV LED device fabricated emitting NUV light; (b) EL curve of the NUV LED device

Figure 2.11 (a) shows a photograph of the NUV LED device emitting strong NUV light. The emission is collected by a large-core optical fiber coupled to the CAS 140-B optical spectrometer. The electric current injection to the NUV LED is carried out by a Model 2450 Interactive SourceMeter instrument system (Keithley, Solon, Ohio, USA). EL of the NUV LED device is successfully obtained under an electric current at 20 mA. Figure 2.11 (b) shows the EL spectrum of the device. The EL peak wavelength of the device is 388 nm at the current of 20 mA.

I-V characteristics of the NUV LED device

I-V measurements are carried out using the Model 2450 Interactive SourceMeter instrument system. Figure 2.12 shows the I-V curves of the NUV LED device. It shows a turn-on voltage at around 3 V which is comparable to the reported values [56, 57]. The series resistance can be estimated by linear fitting to the curve after turn-on, which is around 27.8 Ohm, which is also comparable to the reported results [56, 57].

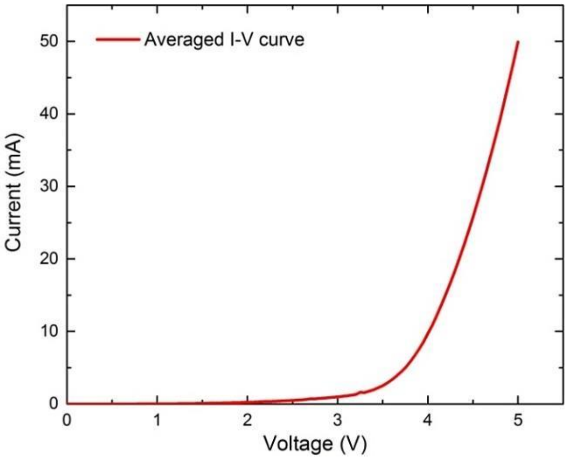

Figure 2.12 I-V curve of the NUV LED device

TLM measurement of the conventional Ni/Au CSL

To test the ohmic property of the Ni/Au CSL, TLM pattern is employed. The sample used for TLM measurement is schematically demonstrated in Figure 2.13. As shown in the figure, identical Ni/Au bars (yellow rectangles in the figure) spaced by different distances are deposited on a GaN mesa. The function of the GaN mesa is to constraint the electric current direction when carrying out the I-V measurements on neighboring Ni/Au bars.

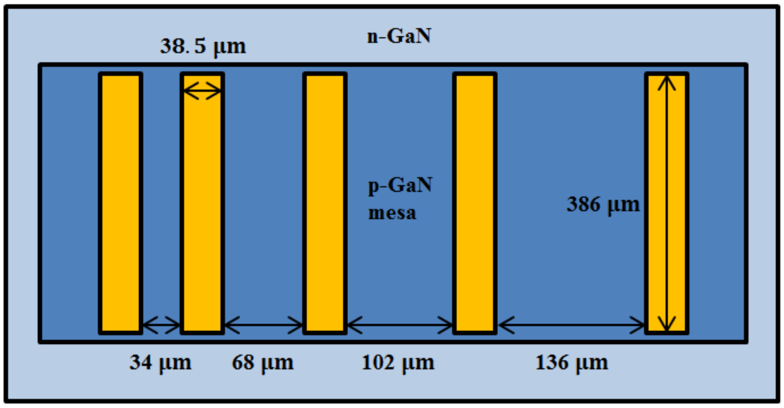

Figure 2.13 Schematic illustration of the pattern for TLM measurement

I-V curves are obtained from measurements on each neighboring bars and all the I-V curves are shown in Figure 2.14. These linear I-V curves indicate the Ni/Au CSL is an ohmic contact. The resistance of each I-V curve can be extracted from the slope through $\frac{1}{\text{slope}}$. Table 2.1 lists the slopes and the corresponding resistances of all the I-V curves.

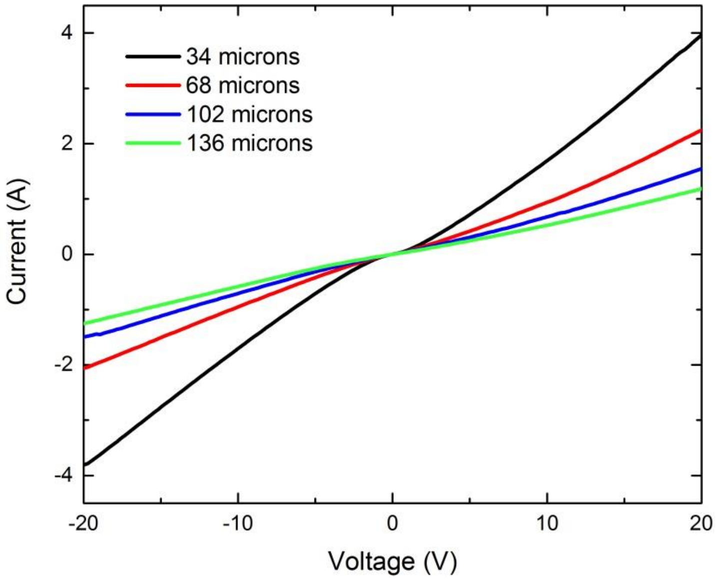

Figure 2.14 I-V curves of neighboring bars with different spacing (measured on Ni/Au)

Table 2.1 Series resistances extracted from I-V curves (measured on Ni/Au)

Bar spacing (μm)	Slope	Resistance (Ω)
34	0.21500	4.651
68	0.12000	8.333
102	0.08100	12.346
136	0.06197	16.137

According to the data listed in Table 2.1, a linear curve $y = 0.109\,x + 0.975$ can be drawn as shown in Figure 2.15. The curve is fitting to the points with the calculated resistance as the y-axis value and the corresponding bar spacing as the x-axis value. Afterwards, the contact resistivity of Ni/Au CSL can be calculated by combining the three formulas demonstrated below [58].

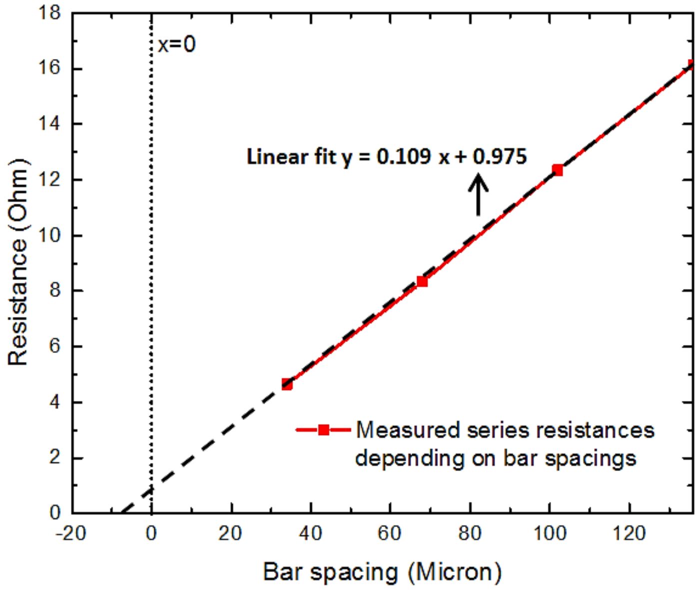

Figure 2.15 Curve of resistance dependence on bar distance (measured on Ni/Au)

$$\text{The Contact resistivity} = \text{Contact resistance} \times \text{Transfer length} \times \text{bar width}$$

$$\text{Contact resistance} = \frac{\text{intercept of y} - \text{axis}}{2}$$

$$\text{Transfer length} = -\frac{\text{intercept of x} - \text{axis}}{2}$$

The width of the Ni/Au bar is 386 μm and it can be extracted from Figure 2.15 that the intercept of y-axis is 0.975 while -8.945 is the intercept of x-axis. According to the formulas listed above, the contact resistivity of Ni/Au CSL is $8.4 \times 10^{-6}\,\Omega \cdot \text{cm}^2$ which is comparable to the most reported values [59-62]. According to the characterization results, Ni/Au is a CSL with excellent electrical properties as reported [59-62].

Transmittance of the conventional Ni/Au CSL

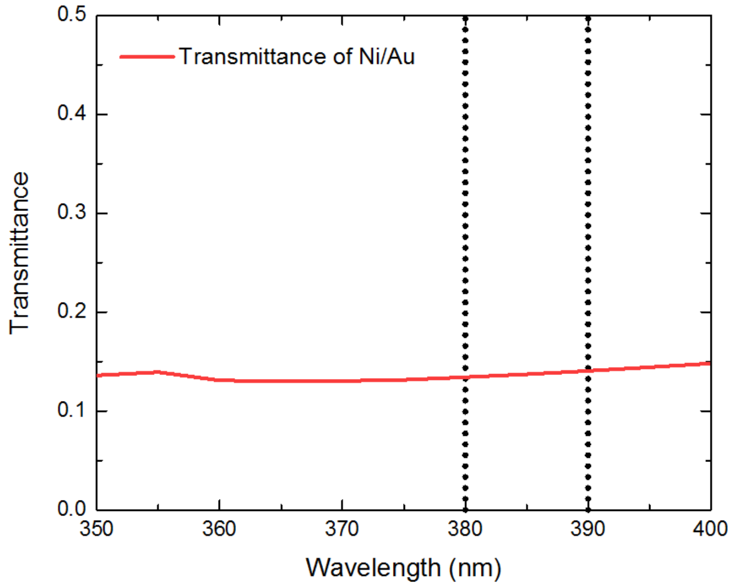

Figure 2.16 Optical transmittance spectrum of Ni/Au CSL

The transmittance of the Ni/Au CSL on the sapphire substrate is measured using an OL 700-71 6-inch diameter integrating sphere system (Gooch & Housego, Ilminster, UK) assisted with a Xenon lamp and a CAS 140 B optical spectrometer (Instrument Systems, Munich, Germany). The transmittance spectrum of the 10 nm Ni/40 nm Au CSL is shown in Figure 2.16. In the wavelength range of the most interest (380-390 nm), the transmittance is measured to be 15-16%, which is comparable to the reported value [60].

2.4 Challenges regarding the NUV LED performance

In this section, some of the challenges that can limit the performance of the NUV LED are demonstrated and discussed.

Light extraction efficiency

For the generated photons in MQWs, the refractive index difference at the GaN (n=2.54)/air (n=1) interface or the SiC (n=2.65)/air interface can make the light easily get trapped inside the LED due to total internal reflection thus resulting in a limited LEE. For example, for GaN, the refractive index difference between GaN and air leads to a small escape cone of 23º for the photons traveling from GaN to air [63, 64]. One approach to improve the LEE of the LED is to apply nanostructures at the LED/air interface. The nanostructures with large sidewall surface offer more pathways for the generated photons to escape hence increasing the LEE [65, 66]. Various nanopatterning methods, which include self-assembled Ni nanoparticles [65], nanosphere masking layer [66] and so on, can be employed to enhance the output light intensity of the LEDs.

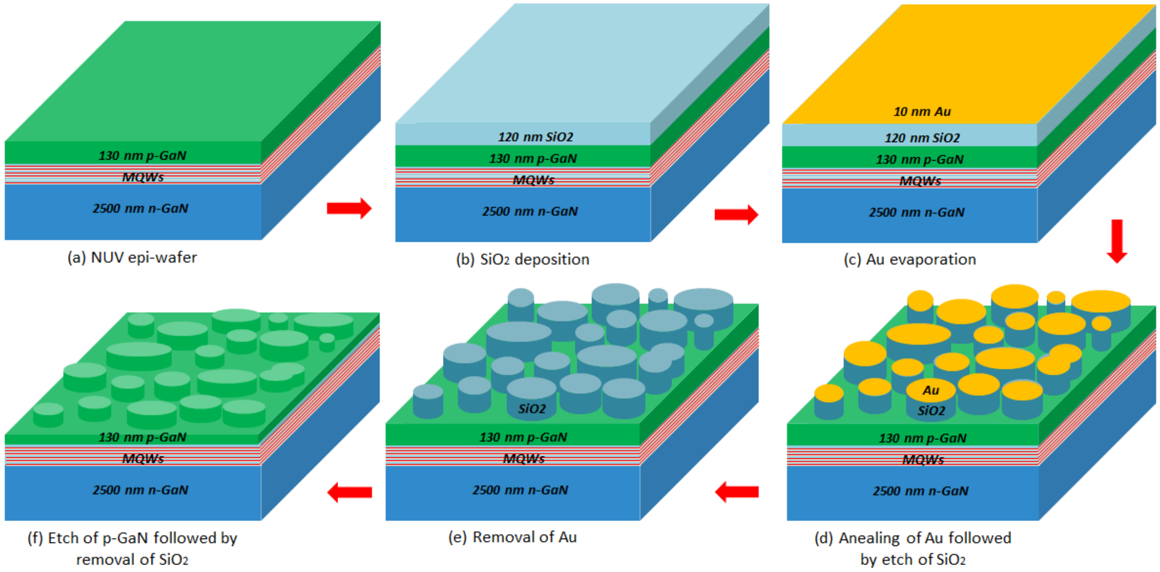

Figure 2.17 Fabrication process of nanostructures on p-GaN

In this work, a method using self-assembled Au nanoparticles is employed to fabricate nanostructures on the p-GaN and the fabrication process is shown in Figure 2.17 (a)-(f). The used NUV-LED epi-wafer is identical as the samples used previously with a 130 nm p-GaN layer on top. Firstly, a 120 nm SiO_2 layer is deposited on the p-GaN by PECVD. Afterwards, 10 nm Au film is formed on the top of SiO_2 by electron-beam evaporation. Then a RTA process is applied to produce self-assembled Au nanoparticles (3 minutes in N_2 at 650 ℃). By a RIE process, the Au pattern is transferred to the SiO_2 layer. Thereafter, an ICP GaN etching process transfers the SiO_2 nanopattern to the epi-wafer thereby forming nanostructures. Finally, the SiO_2 is removed using

5% HF. In the end, GaN nanostructures with heights of around 70 nm, 105 nm, and 155 nm are fabricated, respectively, by controlling the GaN etch time.

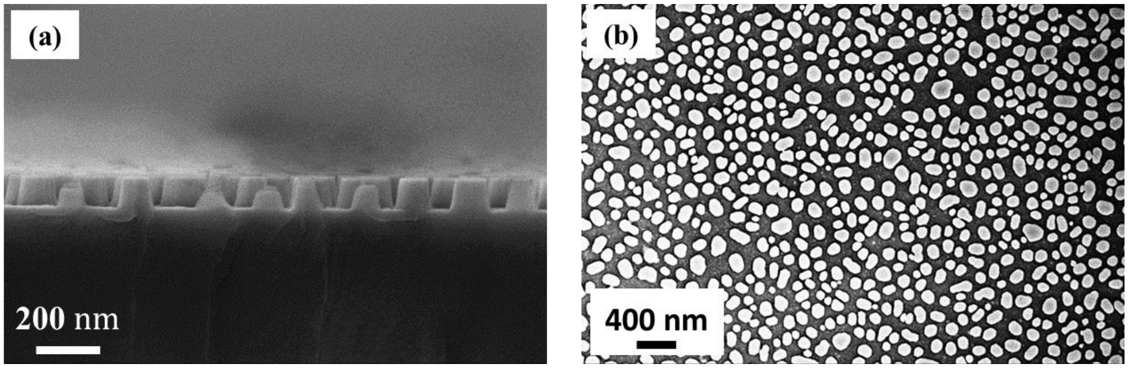

Figure 2.18 SEM images showing (a) the cross section of the 105 nm nanostructures and (b) the top view of the 105 nm nanostructures

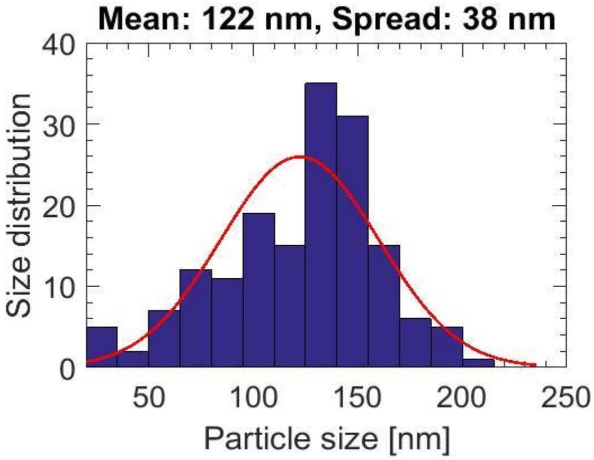

Figure 2.19 Diameter distribution of 105 nm nanostructures

As an example, Figure 2.18 (a) and (b) show the cross section and the top view of the fabricated nanostructures with heights of 105 nm. The corresponding average lateral dimension of the nanostructures is around 120-130 nm as shown in Figure 2.19.

After the fabrication of nanostructures, PL measurement is carried out on the LEDs through excitation by a 375 nm laser. During PL measurement, the NUV LED is excited from the backside (the substrate side) and detected from the front side (the p-GaN side). According to the measurement, the PL intensity is improved by 65%, 74% and 38% using nanostructures with heights of 70 nm, 105 nm, and 155 nm, respectively, in comparison with the corresponding LEDs before nanostructure fabrication. The highest PL enhancement of 74% by the 105 nm nanostructures shown in Figure 2.20 is 28 % higher than the reported 58% PL enhancement using silica nanospheres [66]. The improved PL could be attributed to the optimized structure height in this work. The result indicates that higher nanostructures have better ability to extract light out of LEDs when comparing nanostructures with heights of 70 nm and 105 nm. However, too deep GaN etch could harm the MQWs and introduce damage to the active region resulting in a decrease of radiative recombination rate, which is the case of 155 nm nanostructures.

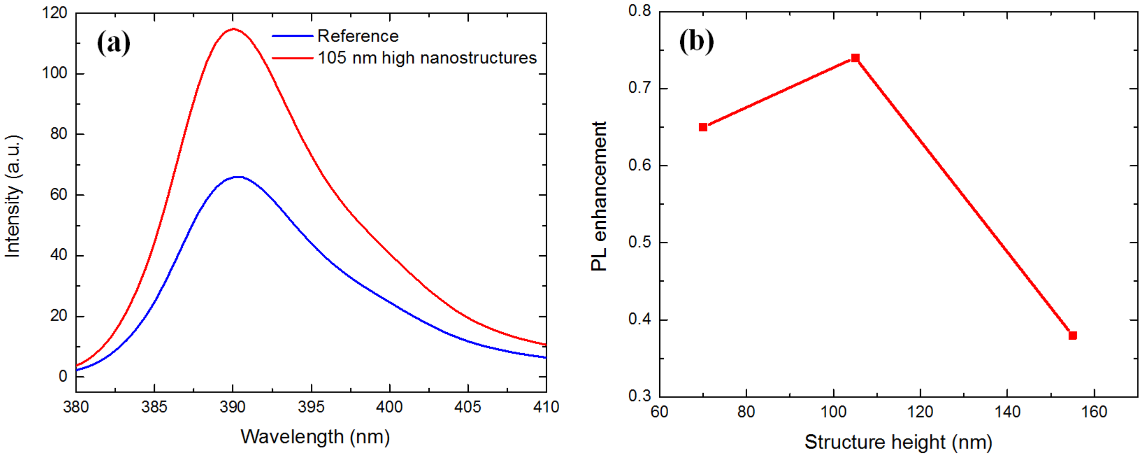

Figure 2.20 PL enhancement of NUV LEDs (a) by 105 nm nanostructures and (b) by nanostructures of different heights

The nanostructures fabricated by this method can also be applied to the SiC substrates of LEDs. For example, for the f-SiC based white LED shown in Figure 1.1, the nanostructures can be fabricated on the f-SiC substrate to enhance the LEE hence increasing the output light.

Internal quantum efficiency

The radiative carrier recombination and photon generation processes take place in the active MQWs. By altering the indium composition in InGaN/GaN MQWs, the bandgap can be tuned from near ultraviolet to the entire visible spectrum. A NUV LED usually contains low indium composited wells leading to a small band-offset, which makes it relatively easy for the injected carriers to escape from the active region hence resulting in a limited IQE [46]. LEDs emitting longer wavelengths , e.g. green LEDs, usually have a high indium content in the InGaN/GaN MQWs. Exposing the MQWs of green LEDs by fabricating nanopillar structures on top, the internal strain, which results from the large lattice mismatch existing at the heterointerface, can be released [67, 68]. By this way, nanopillar structures improve the radiative recombination rate and thus enhance the IQE of the LEDs. However, for the NUV LEDs, this method cannot effectively improve the IQE due to the low indium content in the MQWs leading to an already small lattice mismatch in InGaN/GaN MQWs. The lattice mismatch in InGaN/GaN MQWs can be estimated for NUV and green LEDs, respectively, as shown below.

For Green LEDs ($\lambda = 555$ nm) with InGaN/GaN QWs, it can be read from Figure 2.1 that the bandgap energy is $E_{InGaN} = 2.234$ eV. In addition E_{GaN} = 3.42 eV and E_{InN} = 0.7 eV. The standard equation of the bandgap energy depending on indium composition at room temperature is shown below.

$$E_{InGaN}(x) = (1 - x)E_{GaN} + xE_{InN} - bx(1 - x) \text{ [69]}$$

$E_{InGaN}(x)$ represents the bandgap energy of $In_xGa_{1-x}N$ and b=1.4 eV is the bowing parameter. Then, it can be obtained that x=0.323.

The Vegard's law regarding the lattice constant is shown below.

$$a_{A_{(1-x)}B_x} = (1 - x)a_A + xa_B$$

The below equation can be obtained for $In_xGa_{1-x}N$.

$$a_{In_xGa_{(1-x)}N} = (1 - x)a_{GaN} + xa_{InN}$$

The above equation can also be written as below.

$$a_{In_{0.323}Ga_{0.677}N} = (1 - 0.323)a_{GaN} + 0.323a_{InN}$$

It can be read from Figure 2.1 that, for GaN barrier with E_{GaN} = 3.42 eV, the lattice constant a_{GaN}=3.19 Å. For InN with E_{InN} = 0.7 eV, a=3.545 Å. In the end, the lattice Constant of green $In_{0.323}Ga_{0.677}N$ can be calculated to be $a_{In_{0.323}Ga_{0.677}N} = 3.31$.

In the end, the lattice mismatch between InGaN and GaN for green LEDs can be calculated as

$$\frac{a_{In_{0.323}Ga_{0.677}N} - a_{GaN}}{a_{GaN}} = \frac{3.31 - 3.19}{3.19} = 3.8\%$$

Similarly, for NUV LED ($\lambda = 390$ nm) with InGaN/GaN QWs, it can be read from Figure 2.1 that the bandgap energy is $E_{InGaN} = 3.263$ eV. Besides, E_{GaN} = 3.42 eV and E_{InN} = 0.7 eV.

According to the equation below, it can be obtained that x=0.038.

$$E_{InGaN}(x) = (1 - x)E_{GaN} + xE_{InN} - bx(1 - x)$$

According to Vegard’s law, the following equation can be obtained.

$$a_{In_{0.038}Ga_{0.962}N} = (1 - 0.038)a_{GaN} + 0.038a_{InN}$$

In the end, the lattice Constant of NUV $In_{0.038}Ga_{0.962}N$ can be calculated to be $a_{In_{0.038}Ga_{0.962}N} = 3.2$.

The lattice mismatch between InGaN and GaN for NUV LEDs can be calculated as below.

$$\frac{a_{In_{0.038}Ga_{0.962}N} - a_{GaN}}{a_{GaN}} = \frac{3.2 - 3.19}{3.19} = 0.3\%$$

According to the calculation, the lattice mismatch of Green LEDs in InGaN/GaN MQWs is around 12 times larger than that of NUV LEDs. Therefore, the approach of nanopillars is not suitable for IQE optimization of the NUV LEDs.

Current Spreading Layers

CSLs on LEDs allow a more uniform carrier distribution avoiding the current crowding effect [70, 71].

The conduction mechanism for the CSL on the GaN includes thermionic emission and field emission. In thermionic emission, carriers need to transport over the potential barrier at the GaN/CSL interface. In field emission, carriers can tunnel through the potential barrier at the GaN/CSL interface, which takes place when the doping concentration is sufficiently high hence narrowing the barrier width. Therefore, to have a CSL with good conductivity, a low barrier height at the GaN/CSL interface (to enhance the thermionic emission) and a high doping concentration of the GaN (to enhance the field emission) are necessary.

Regarding the doping concentration of the GaN at the p-GaN/CSL interface, the epi-wafer used in this work contains a highly Mg doped p^+-GaN layer on top, which has a thickness of 15 nm and a doping concentration of $2\times10^{20}\,cm^{-3}$.

In terms of the barrier height at the GaN/CSL interface, however, it is difficult to find a CSL material having a sufficiently high work function for p-GaN, thus leading to a large Schottky barrier height (SBH) at the p-GaN/CSL interface [71-73]. The SBH depends on the work function of the CSL material in contact and is determined by the difference between the sum of the electron affinity (4.1 eV) and the bandgap E_g (3.4 eV) of the p-GaN (7.5 eV in total), and the work function Φ_c of the CSL material, as shown in Figure 2.21 [74-77]. In order to maximize the drive current and minimize the leakage current under a certain voltage, the work function of the CSL material is desired to be greater than the sum of 7.5 eV for p-GaN. Table 2.2 lists metals with relatively high work functions but still, all of them are smaller than 7.5 eV.

Due to the difficulties of finding a conductive material with a work function larger than 7.5 eV, another option is to reduce the SBH by decreasing the difference through the employment of a material with a sufficiently high work function [74-77]. The reduction of the SBH can result in a lower contact resistance and it has been reported that the contact resistance at the p-GaN/CSL interface decreases exponentially with increased work functions of CSL materials [72].

Table 2.2 Work functions of several metals

Metals	Work functions (eV)
Pt	5.12 – 5.93
Au	5.10 – 5.47
Ag	4.26 – 4.74
Ti	4.33
Al	4.06 – 4.26

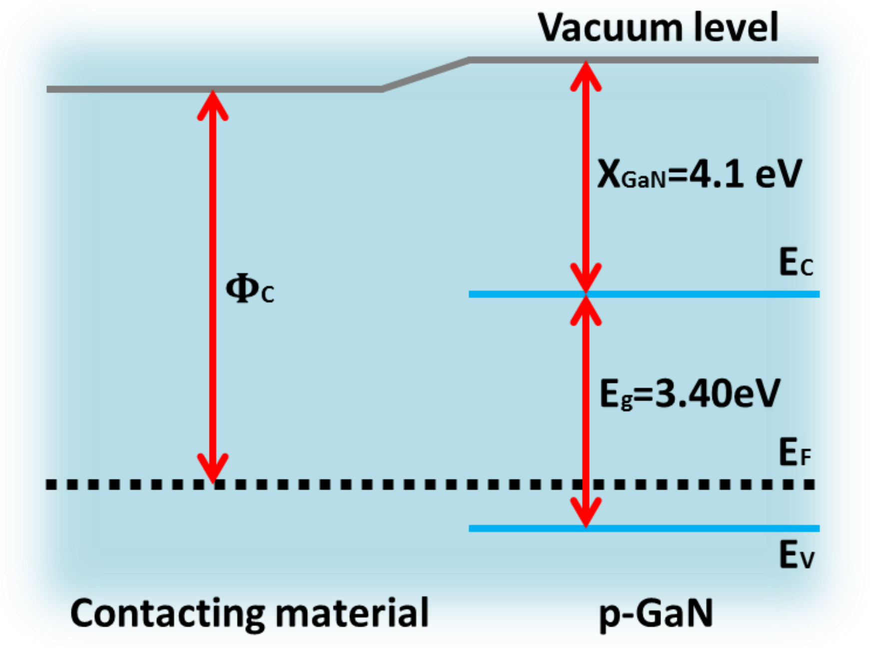

Figure 2.21 Band diagram of p-GaN and contacting material

In addition, in the application of NUV LEDs, it is also important for the CSLs to have a high transmittance in the NUV wavelength region. As shown in the previous sections, the conventional Ni/Au CSL presents excellent electrical performance, but its low transmittance in the NUV wavelength region hinders its use in NUV LEDs [56]. Hence, it is necessary to find a conductive CSL with also a high NUV transmittance.

2.5 Summary

The NUV LED device with the conventional Ni/Au CSL is successfully fabricated by a standard fabrication process. During the fabrication, the problem of n-pad peeling-off is studied and solved by minimizing the undesired structures produced on the n-GaN during the GaN etch process. This improvement is achieved by employing a BOE wet etch process in the SiO_2 mesa fabrication instead of the RIE dry etch process of SiO_2.

After device fabrication, the NUV LED is characterized on the electrical and optical properties. NUV EL of the device is obtained and a peak wavelength of around 388 nm is achieved under a current of 20 mA. According to the I-V measurement, the device presents a turn-on voltage around 3 V and a series resistance around 27.8 Ohm. In addition, TLM measurement is carried out to test the ohmic property of the conventional Ni/Au CSL. Linear I-V curves are obtained from the Ni/Au CSL in the TLM measurement indicating the ohmic behavior and a contact resistivity around $8.4 \times 10^{-6}\,\Omega \cdot \mathrm{cm}^2$ is obtained from the calculation. Although the Ni/Au CLS possesses good electrical performance, its transmittance smaller than 20% in the NUV wavelength range can limit the performance of the NUV LED. This indicates the requirement of a CSL with not only good electrical properties but also high transmittance in the NUV LED application.

Challenges that can limit the NUV LED performance are discussed in the end of this chapter. Firstly, to minimize the number of photons trapped inside the LED by total internal reflection, a method of surface roughening assisted with self-assembled Au nanoparticles is studied. In the end, the nanostructures with heights around 105 nm give the highest PL enhancement due to the increased LEE. Secondly, because of the low indium composited wells in the NUV LED, the injected carriers can escape more easily therefore leading to a limited IQE when compared to the LEDs emitting longer wavelengths. The lattice mismatch in InGaN/GaN MQWs of Green LEDs is calculated to be around 12 times larger than that of NUV LEDs. Hence the commonly used approach of nanopillars is not an efficient way to improve the IQE of the NUV LED. Last but not the least, since it is difficult to find a CSL material with a work function larger than 7.5 eV for the GaN-based NUV LED, a large SBH at the p-GaN/CSL interface can be formed. So it is important to employ a CSL material with a sufficiently high work function to reduce the SBH. In addition, a high transmittance in the NUV wavelength region is also important for the CSL in the NUV LED application.

Chapter 3 Transparent conductive current spreading layer materials

In this chapter, transparent conductive material AZO is studied as a promising CSL material on a NUV LED. Characterizations and Comparisons are made between different AZO based CSLs.

3.1 Aluminum-doped zinc oxide and comparison with indium tin oxide

A CSL is a critical component in a GaN based LED. It is well known that without a CSL, non-uniformity distribution of carriers induced by the highly resistive p-GaN (inherently low hole concentration of the p-GaN) can lead to current crowding [78-80]. A CSL on p-GaN can effectively constraint the current crowding effect by uniformly spreading out the electric carriers over the lateral direction. As shown in the previous chapter, conventional Ni/Au CSL on p-GaN has a good electrical performance, but its low transparency in the NUV wavelength region hinders its use in NUV LEDs [60, 81, 82]. Therefore, a conductive CSL with high transmittance in the NUV region is extremely desired to further improve the performance of NUV LEDs.

Transparent conductive oxide (TCO) materials possess superior optical and electrical properties hence attracting extensive attentions in electronic and optoelectronic applications [83-87]. Currently, ITO with superior conductivity and transparency has been widely used as a CSL material in NUV LEDs [88-89]. However, the cost of ITO can grow high in the future due to the scarceness of indium while its thermal stability is not satisfactory [80, 90]. Hence, it becomes necessary to look for alternative transparent conductive materials in the application of NUV LEDs.

ZnO is a popular TCO semiconductor, which is famous for its wide direct band gap (3.37 eV), high transparence in visible region, good conductivity and high thermal stability [91, 92]. Thanks to these advantages, it has been a promising material in various applications including UV light emitters, transparent high-power electronics, surface acoustic wave devices, and chemical gas sensing [91]. Recently, lots of research efforts have been devoted to the technology of ZnO doping since its structural, electrical and optical properties can be improved by doping with various impurities like ions and alkali metals [93, 94]. It has been reported that, Sb-, Ga-, In-, and Al-doped ZnO thin films are promising TCO materials in the LED industry [93-96]. Especially, Al is one of the most promising dopants for mass production and the AZO thin film has been treated as a potential candidate for the alternative to ITO [97]. It is because the AZO material possesses similar electrical and optical properties in comparison with ITO. Meanwhile, as an indium-free material, it is low-cost, nontoxic and more stable at high temperatures, which offers substantial attractions in the LED industry [97].

There have been various techniques for producing AZO films, such as chemical vapor deposition (CVD), molecular beam epitaxy (MBE), pulse laser deposition, atomic layer deposition (ALD), e-beam evaporation and sputtering [98-104]. Among these, the method of sputtering deposition is one of the most popular ways since it is low-cost, high-efficiency and can produce AZO films with satisfactory quality like good uniformity, smooth surface as well as good adhesion to substrates.

In this section, NUV LED devices with two types of CSLs, which are the AZO CSL and the ITO CSL, are fabricated and investigated on the optical and electrical properties, respectively, followed by comparisons.

3.1.1 Fabrication process

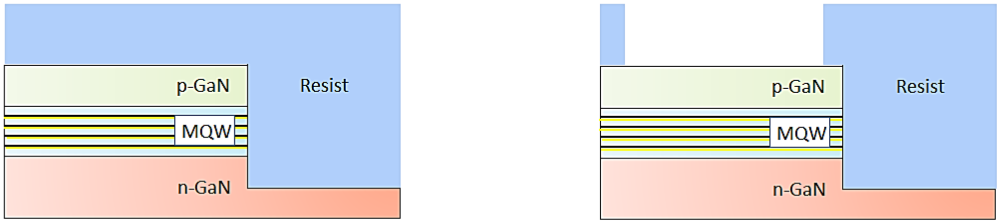

(a) Spin-coating of N-LOF 2020

(b) Lithography of CSLs

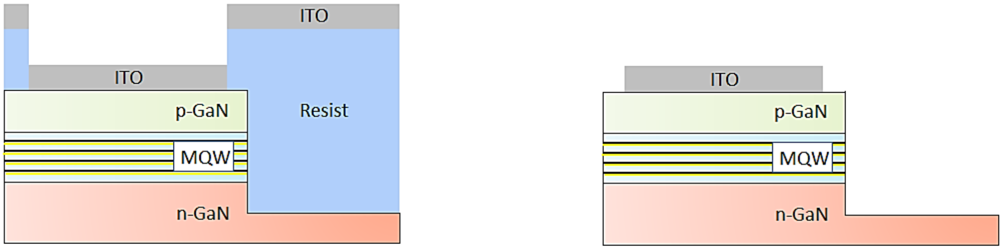

(c) Deposition of ITO

(d) ITO liftoff followed by annealing

Figure 3.1 Fabrication steps of the ITO CSL on the GaN mesa

Figure 3.1 (a)-(d) shows the fabrication process of the ITO CSL on the GaN mesa. After mesa fabrication shown in Figure 2.4, the CSL lithography is carried out on the GaN mesa by spin coating of 2 µm negative photoresist N-LOF 2020 followed by exposure and liftoff just like the process demonstrated in Figure 2.5. Afterwards, 250 nm ITO is e-beam evaporated on the mesa using an III-V Dielectric Evaporator. The employed ITO target consists of 90% In_2O_3 and 10% SnO_2. The deposition is carried out using a power of 5 W under O_2 ambient with a pressure of 10^{-5} mBar. After ITO liftoff in MICROPOSIT Remover 1165 assisted with ultrasonic followed by annealing in N_2 at 550°C for 30 minutes, the ITO CSL is produced on the GaN mesa. In the end the Ti/Au pad is added to the p- and n-GaN, respectively. The step of pad fabrication is the same as the process introduced in Figure 2.5.

The LED device with 250 nm AZO CSL is fabricated using the same process except that the AZO deposition is carried out using a sputtering cathode TORUS with a ZnO target containing 2% Al_2O_3. During the sputtering, a power of 75 W under Ar ambient with a pressure of 5 mTorr is used.

In the end, two types of NUV LED devices with a 250 nm ITO CSL and a 250 nm AZO CSL are made for the following characterizations.

3.1.2 Characterizations

After fabrication of NUV LED devices with ITO and AZO CSLs, optical and electrical properties of the LED devices are characterized. The results are demonstrated and analyzed as below.

Transmittance of ITO and AZO CSLs

Transmittance spectra of the ITO and AZO CSLs on sapphire substrates are measured in the wavelength region of 380-430 nm using an integrating sphere system. As shown in Figure 3.2, the transmittances of the ITO and AZO CSLs are both around 70%. At the 391 nm peak wavelength of the devices, which is shown in Figure 3.3, the transmittance of the ITO CSL is around 72%, while 68% for the AZO CSL, indicating a difference of 4%.

EL of NUV LED devices with ITO and AZO CSLs

EL spectra are obtained by measuring on NUV LED devices with different CSLs. Figure 3.3 shows that both NUV EL spectra are successfully obtained for devices with ITO and AZO CSLs by injecting an electric current of 50 mA. The peak wavelengths of the devices are both at around 391 nm. In addition, the NUV LED device with the ITO CSL shows a 5.5 times EL enhancement at the peak wavelength.

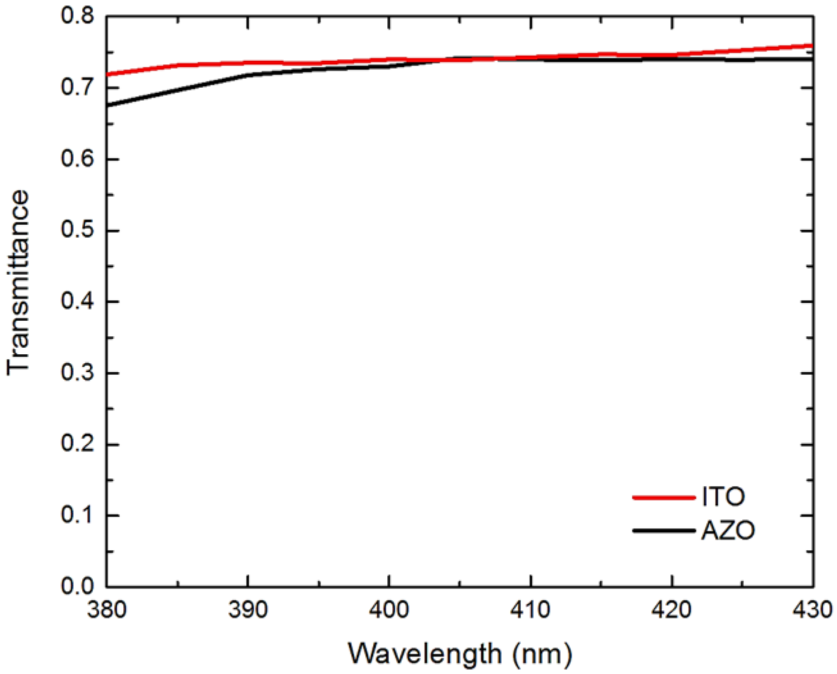

Figure 3.2 Optical transmittance spectra of ITO and AZO CSLs

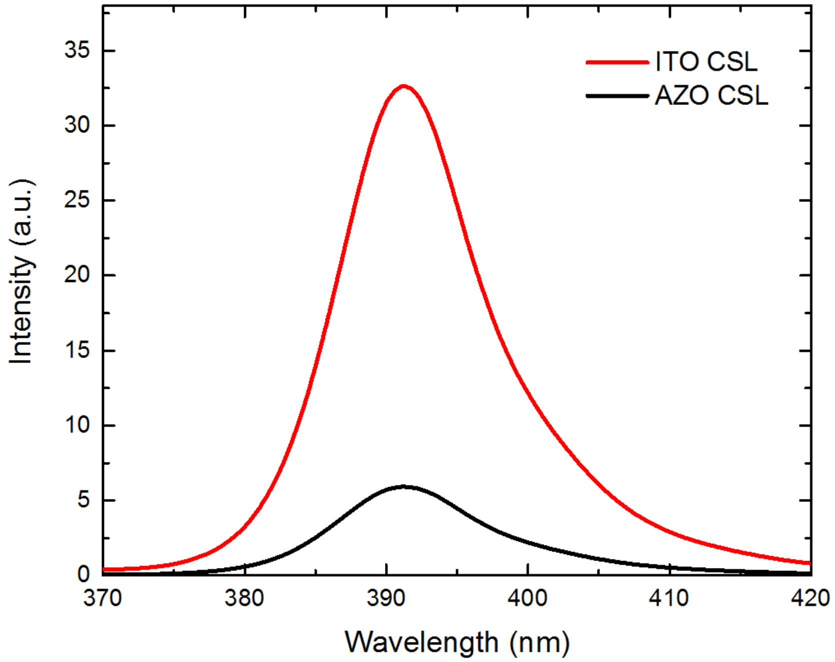

Figure 3.3 EL spectra of NUV LED devices with ITO and AZO CSLs

I-V characteristics of NUV LED devices with ITO and AZO CSLs

Figure 3.10 shows the I-V curves of the fabricated NUV LED devices with ITO and AZO CSLs. The turn-on voltage of around 3.5 V is obtained for the LED device with the ITO CSL while the device with the AZO CSL has a larger turn-on voltage. At a forward voltage of 6 V, the electric currents are 53 mA and 2 mA for the devices with the ITO CSL and the AZO CSL, respectively. This shows a much smaller series resistance of the device with the ITO CSL. The series resistances, which can be estimated by linear fitting to the part after turn-on of the curve, are 31.18 Ohm and 895.10 Ohm for the devices with the ITO CSL and the AZO CSL, respectively.

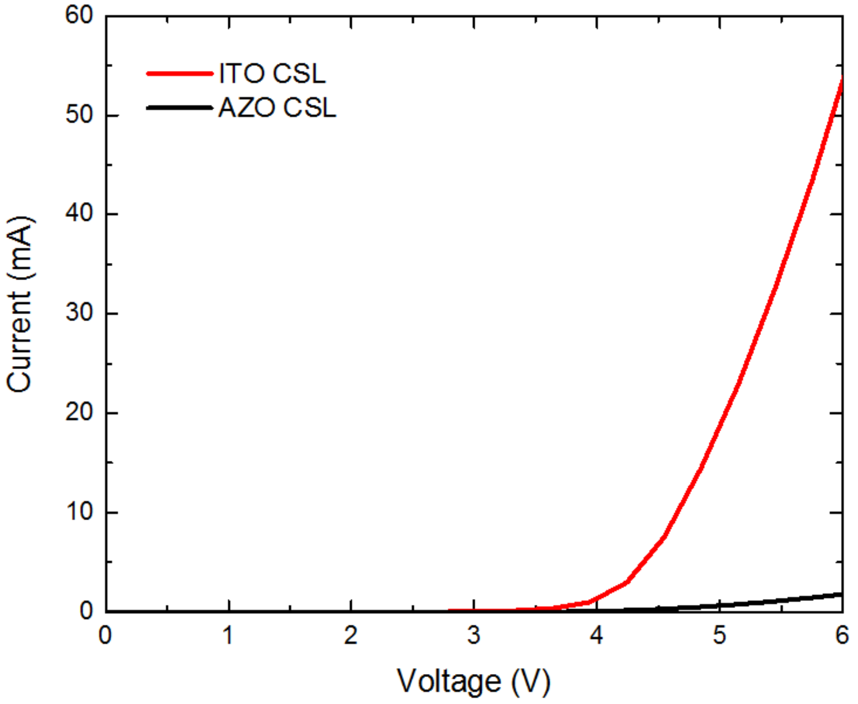

Figure 3.4 I-V curves of NUV LED devices with ITO and AZO CSLs

Ohmic test of ITO and AZO CSLs

To test the ohmic property of ITO and AZO CSLs, the TLM pattern is employed. The structure and the sizes of the sample used for TLM test is identical as the one shown in Figure 2.13. As shown in Figure 2.13, identical ITO or AZO bars spaced by different lengths are deposited on a GaN mesa.

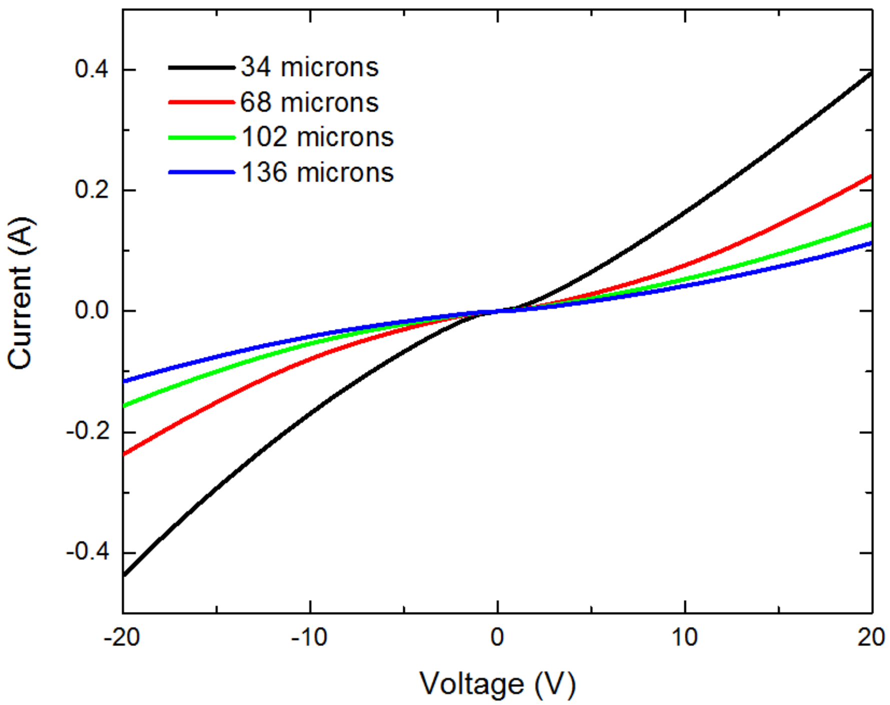

Figure 3.5 I-V curves of neighboring bars with different spacing (measured on ITO)

I-V curves are obtained from measurements on each neighboring bars. Unlike the I-V curves of the ITO bars, the I-V curves measured on the AZO bars are completely nonlinear. As shown in Figure 3.5, the I-V curves of the ITO bars are almost linear. The resistance of each I-V curve can be extracted from the curve slope through $\frac{1}{\text{slope}}$. Table 3.1 lists the slopes and the corresponding resistances of all the I-V curves.

Table 3.1 Series resistances extracted from I-V curves (measured on ITO)

Bar spacing (μm)	Slope	Resistance (Ω)
34	0.01864	53.648
68	0.00959	104.275
102	0.00638	156.740
136	0.00490	204.082

Figure 3.6 shows a linear curve $y = 1.482x + 3.745$ drawn by fitting to the measured resistance as the y-axis and the corresponding bar spacing as the x-axis. The contact resistivity of ITO CSL can be calculated as below.

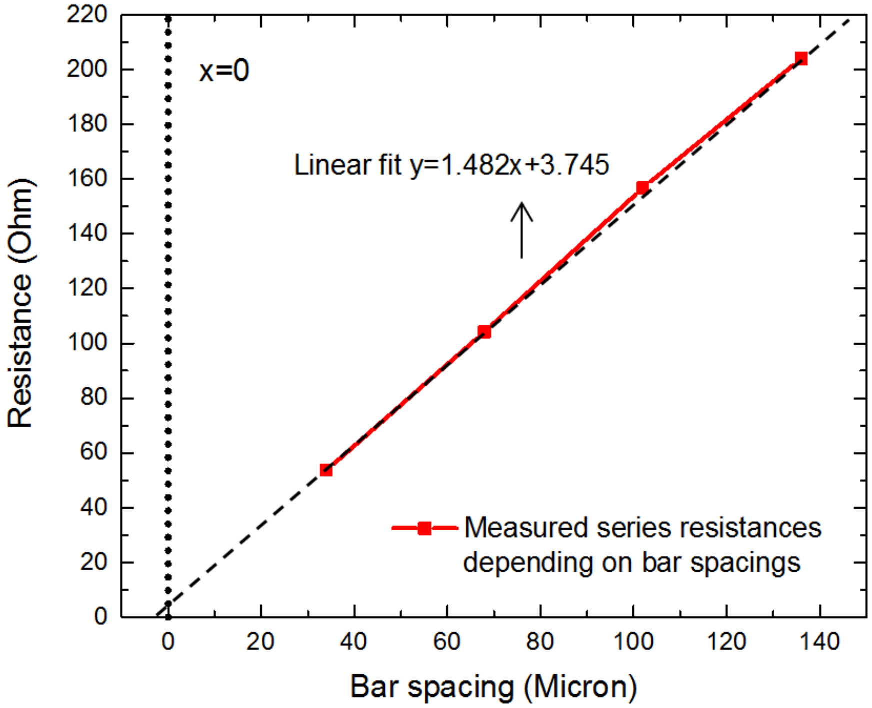

Figure 3.6 Curve of resistance dependence on bar distance (measured on ITO)

The Contact resistivity can be calculated by the formula below.

$$\text{Contact resistivity} = \text{Contact resistance} \times \text{Transfer length} \times \text{bar width}$$

The contact resistance and the transfer length can be calculated by the formulas below.

$$\text{Contact resistance} = \frac{\text{intercept of y} - \text{axis}}{2}$$

$$\text{Transfer length} = -\frac{\text{intercept of x} - \text{axis}}{2}$$

It is known that bar width = 386 μm and it can be extracted from Figure 3.6 that the intercept of y-axis is 3.745 while -5.054 is the intercept of x-axis. According to the formulas listed before, the contact resistivity of the ITO CSL is $1.8 \times 10^{-5}\,\Omega \cdot \text{cm}^2$.

3.1.3 Conclusion

Two types of NUV LED devices with different CSLs which are the ITO CSL and the AZO CSL are successfully fabricated. The transmittances of the ITO and AZO CSLs are both around 70%. The LED device with the ITO CSL shows a 5.5 times stronger EL than that of the AZO CSL at the peak wavelength. The series resistances are estimated to be 31.18 Ohm and 895.10 Ohm for the devices with the ITO CSL and the AZO CSL, respectively. According to the TLM test, the contact resistivity of the ITO CSL is $1.8 \times 10^{-5}\ \Omega \cdot \text{cm}^2$. The results show that, although AZO is a low-cost indium-free material, its performance still needs to be further improved in order to replace the ITO as a CSL on the NUV LED.

3.2 Nickel interlayer for Aluminum-doped zinc oxide

There have been several reports on significant improvement on electrical properties of AZO CSLs by insertion of a Ni based interlayer between the AZO film and the p-GaN [105-107]. This is due to the formation of Ga vacancies near the surface of p-GaN leading to a decreased contact resistivity [108-109]. In this section, NUV LED devices with two types of AZO based CSLs, which are Ni/AZO CSLs and AZO CSLs, are fabricated and investigated on the optical and electrical properties, respectively, followed by comparisons.

3.2.1 Fabrication process

Figure 3.7 (a)-(h) shows the steps for Ni/AZO CSL fabrication. After mesa fabrication shown in Figure 2.4, the first CSL lithography is carried out on the GaN mesas by spin coating of 2 µm negative photoresist N-LOF 2020 followed by exposure and liftoff just like the fabrication process demonstrated in Figure 2.5. Afterwards, a layer of 2 nm Ni is e-beam evaporated on the patterned N-LOF 2020 resist layer. After Ni liftoff in MICROPOSIT Remover 1165 assisted with ultrasonic, Ni CSLs are formed on the mesas. Then, the Ni CSLs go through rapid thermal annealing in air at 525 °C for 5 minutes.

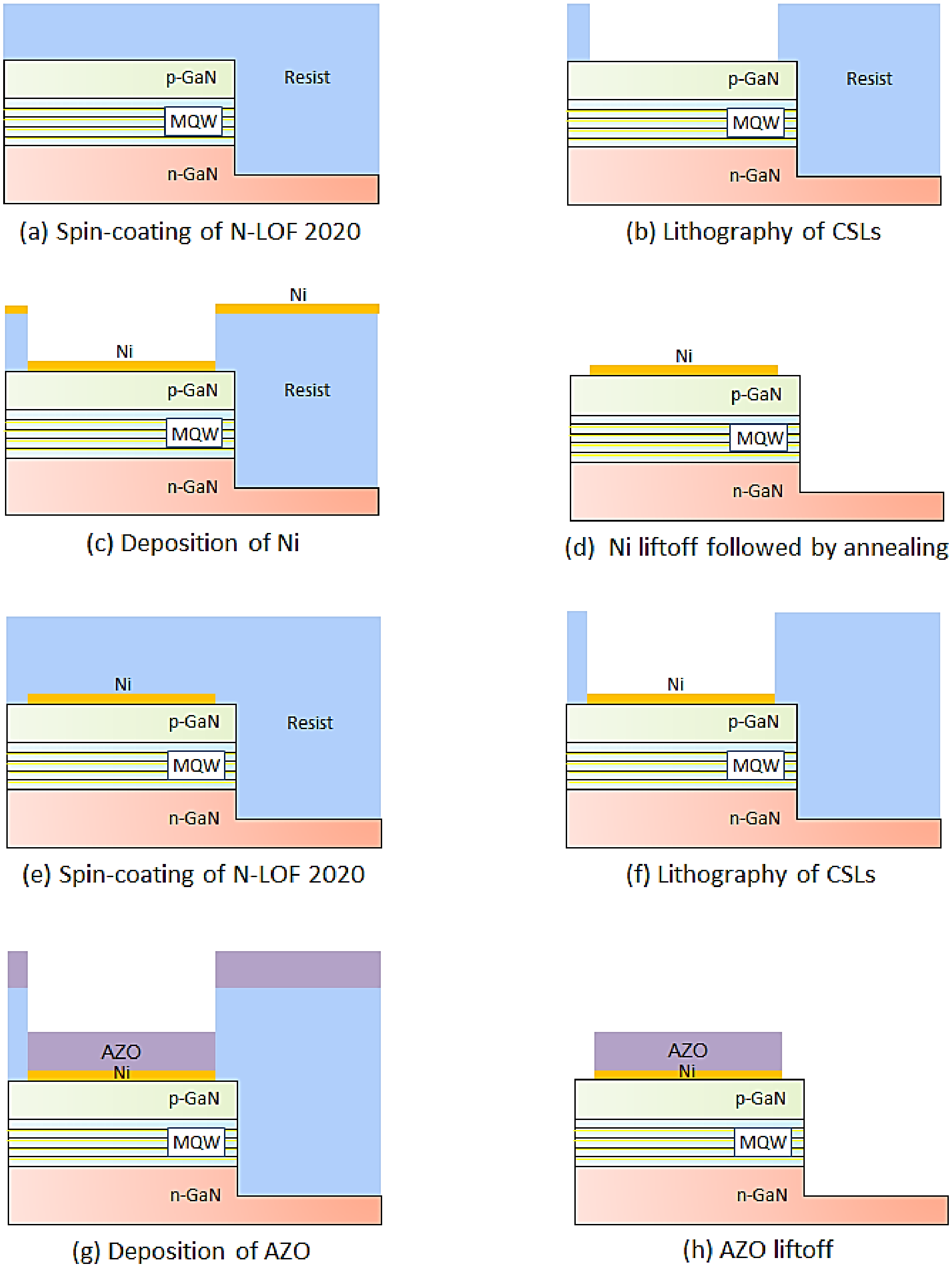

(a) Spin-coating of N-LOF 2020
(b) Lithography of CSLs
(c) Deposition of Ni
(d) Ni liftoff followed by annealing
(e) Spin-coating of N-LOF 2020
(f) Lithography of CSLs
(g) Deposition of AZO
(h) AZO liftoff

Figure 3.7 Fabrication steps of AZO based CSLs on GaN mesas

Subsequently, the second CSL lithography, which employs identical photoresist, parameters and mask design as the first lithography, is carried out followed by sputtering deposition of 250 nm AZO. After AZO liftoff in MICROPOSIT Remover 1165 assisted with ultrasonic, the Ni/AZO CSLs are produced on GaN mesas. In the end the Ti/Au pads are added to the p- and n-GaN respectively to make a device. The step of the metal pad fabrication is the same as the process introduced in Figure 2.5.

In addition to the NUV LED devices with Ni/AZO CSLs, the devices with 250 nm AZO CSLs are also fabricated for comparison.

3.2.2 Characterizations

After fabrication of NUV LED devices with different AZO based CSLs, optical and electrical properties of the devices with the Ni/AZO CSL and the AZO CSL are characterized. The characterization results are demonstrated and analyzed as below.

Transmittance of AZO based CSLs

Transmittance spectra of the AZO based CSLs on sapphire substrates are measured in the wavelength region of 380-430 nm using an integrating sphere system. As shown in Figure 3.8, the transmittance of the AZO CSL is higher than that of the Ni/AZO CSL due to the absorption of NUV photons by the Ni interlayer. At the 386 nm peak wavelength of the devices, the transmittance of the AZO CSL is around 70%, while 67% for the Ni/AZO CSL, indicating a decrease of 3% by adding the Ni interlayer. However, the transmittances of the AZO based CSLs are much higher than that of the conventional Ni/Au CSLs (13-14% in the wavelength region of 380-390 nm). In comparison with the conventional Ni/Au CSL, a 5 times and a 4.8 times higher transmittances are achieved by the AZO CSL and the Ni/AZO CSL, respectively.

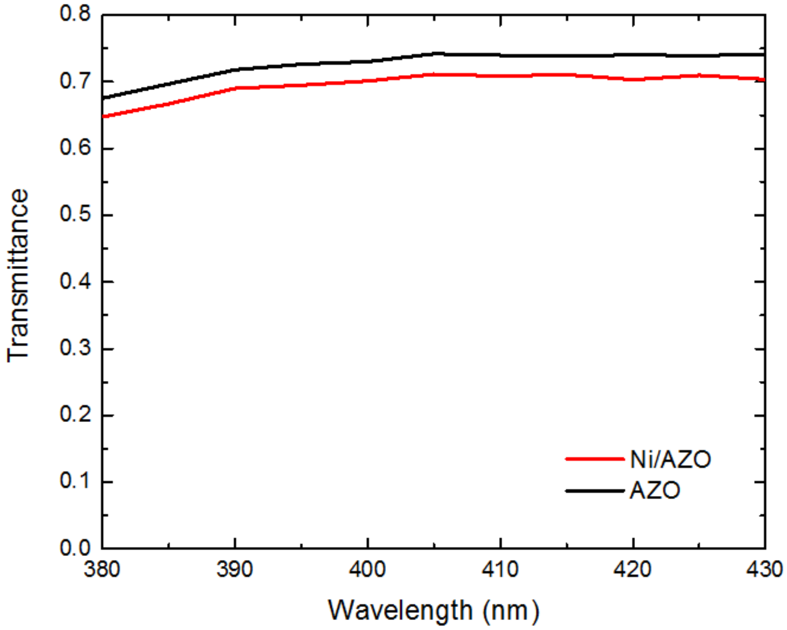

Figure 3.8 Optical transmittance spectra of AZO based CSLs

EL of NUV LED devices with AZO based CSLs

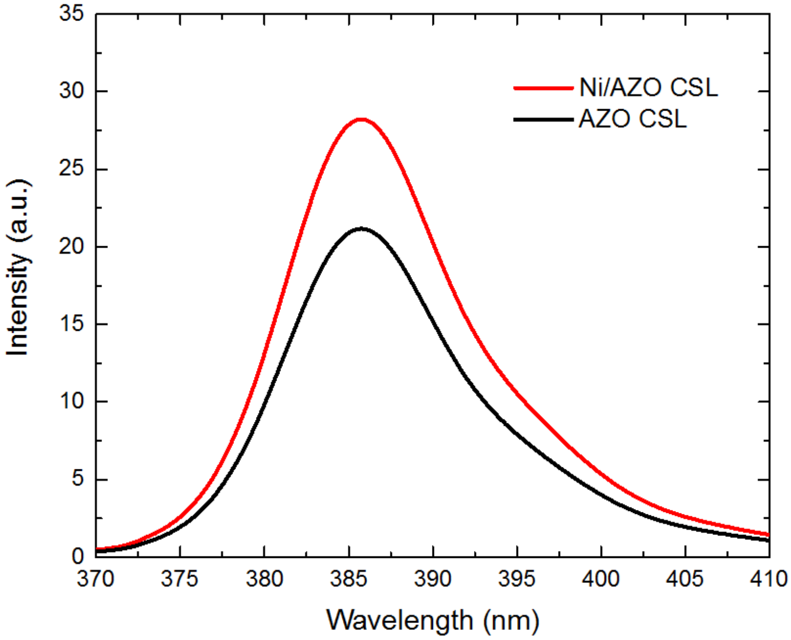

Figure 3.9 EL spectra of NUV LED devices with AZO based CSLs

EL spectra are obtained by measuring on NUV LED devices with different AZO based CSLs. Figure 3.9 shows that both NUV EL spectra are successfully obtained for devices with AZO based CSLs by injecting an electric current of 50 mA. The peak wavelengths of the devices are both at around 386 nm which are within the expectation. In addition, the NUV LED device with the Ni/AZO CSL shows a 1.33 times stronger EL at the peak wavelength of 386 nm by adding the Ni interlayer under the AZO layer. This confirms the better electrical performance of the Ni/AZO CSL in comparison with that of the AZO CSL.

I-V characteristics of NUV LED devices with AZO based CSLs

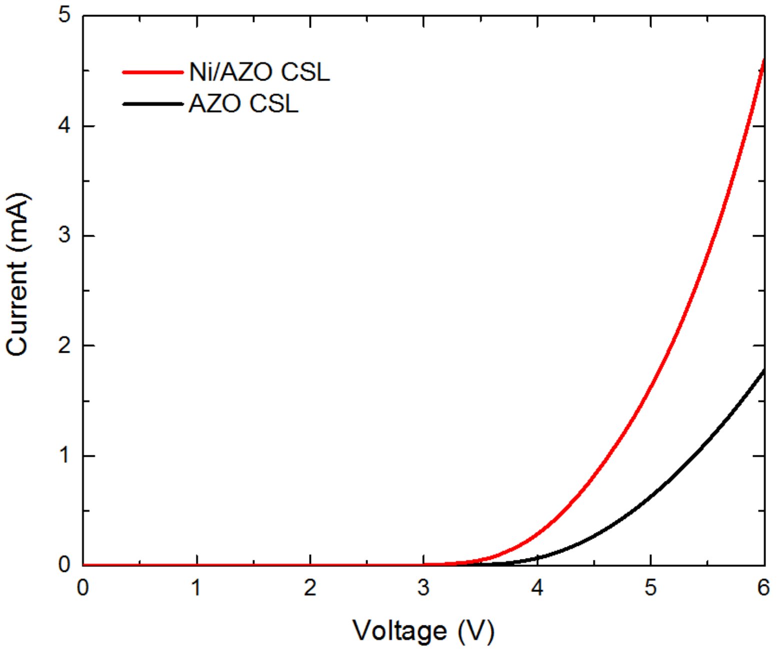

Figure 3.10 I-V curves of NUV LED devices with AZO based CSLs

Figure 3.10 shows the I-V curves of the fabricated NUV LED devices with AZO based CSLs. Turn-on voltages of around 3.5 V and 3.7 V are obtained for the devices with the Ni/AZO CSL and the AZO CSL, respectively. At a current of 1 mA, the operation voltages are 4.7 V and 5.5 V for the devices with the Ni/AZO CSL and the AZO CSL, respectively. This shows a reduced series resistance of the device by using a Ni interlayer in the Ni/AZO CSL.

The series resistances, which can be estimated by linear fitting to the part after turn-on of the curve, are 350.88 Ohm and 890.47 Ohm for the devices with the Ni/AZO CSL and the AZO CSL, respectively. The device with the AZO CSL shows a 2.54 times larger series resistance than that of the device with the Ni/AZO CSL. The smaller series resistance by using the Ni/AZO CSL can be attributed to the formation of Ga vacancies near the p-GaN surface.

I-V measurements on Ni/AZO CSLs with TLM patterns

The Ni/AZO bars, which are identical as the TLM patterns employed in Figure 2.13, are measured for the test of ohmic property. All the I-V curves of the Ni/AZO bars are nonlinear indicating that they do not possess ohmic behavior.

3.2.3 Conclusion

NUV LED devices with two types of transparent conductive CSLs, which are a Ni/AZO CSL and an AZO CSL, respectively, are successfully fabricated. After the fabrication, the devices with different AZO based CSLs are characterized and compared. NUV EL emissions of the devices of both types are obtained by injecting electric currents and peak wavelengths at around 386 nm are achieved under an injection current of 50 mA. In addition, the device with the Ni/AZO CSL shows a 1.33 times stronger EL at the peak wavelength of 386 nm by adding a Ni interlayer in comparison with the device with the AZO CSL. Furthermore, in I-V measurements of the devices, the one with the AZO CSL shows a 2.54 times larger series resistance than that of the one with the Ni/AZO CSL. In the transmittance measurements, both CSLs show high transmittance in the NUV wavelength region. At the peak wavelength of 386 nm, the transmittance of the AZO CSL is around 70%, while 67% for the Ni/AZO CSL, indicating a 5 times and a 4.8 times higher transmittance, respectively, in comparison with the conventional Ni/Au CSL. These experiments indicate that the AZO based CSLs present a high transmittance in the NUV wavelength region and the Ni interlayer can improve the electrical performance of the AZO CSL. However, the electrical properties of the AZO based CSLs are not as good as that of the ITO CSL and still need further optimization.

3.3 Graphene interlayer for aluminum-doped zinc oxide

As shown previously, Ni/Au CSLs have better electrical performance than that of transparent AZO based CSLs. To further improve the performance of AZO based CSLs, one way is to lower the SBH at the contacting interface between the CSL and the semiconductor. As mentioned before, for GaN based NUV LEDs, it is difficult to find an appropriate CSL material having a sufficiently high work function (larger than 7.5 eV) for p-GaN, which leads to a large SBH at the p-GaN/CSL interface. Through employment of a material with a sufficiently high work function, the SBH at the interface can be reduced by decreasing the difference [74-77]. Here, the idea is to use a single layer graphene (SLG) interlayer to improve the performance of AZO based CSLs in NUV LED related applications.

SLG is a two-dimensional carbon material consisting of a hexagonal array of carbon atoms, which is known for possessing outstanding properties including high carrier mobility, good thermal conductivity and mechanical stability [110-112]. Moreover, the high transparency in a wide spectral range including NUV makes itself a promising transparent CSL material in NUV LED related applications [113, 114]. Furthermore, in terms of the work function, graphene is more superior when compared to the reported work function of AZO [115-119]. This indicates a potential of being an effective interlayer to improve the performance of AZO based CSLs by modifying the SBH.

There has been work focused on combining graphene and AZO nanorods for improvement of LED device performance [120-122]. However, few research results have been reported on the combination of SLG and AZO as plain CSLs in the application of NUV LEDs. In this work, the effect of adding a SLG film to an AZO based CSL for a NUV LED is investigated. AZO based CSLs with and without a SLG interlayer are fabricated on both sapphire samples and NUV epi-wafers. After the fabrication, optical properties of the CSLs on sapphire samples and electrical properties on NUV epi-wafers are measured and compared.

3.3.1 Fabrication process

Transferring graphene sheets to substrates

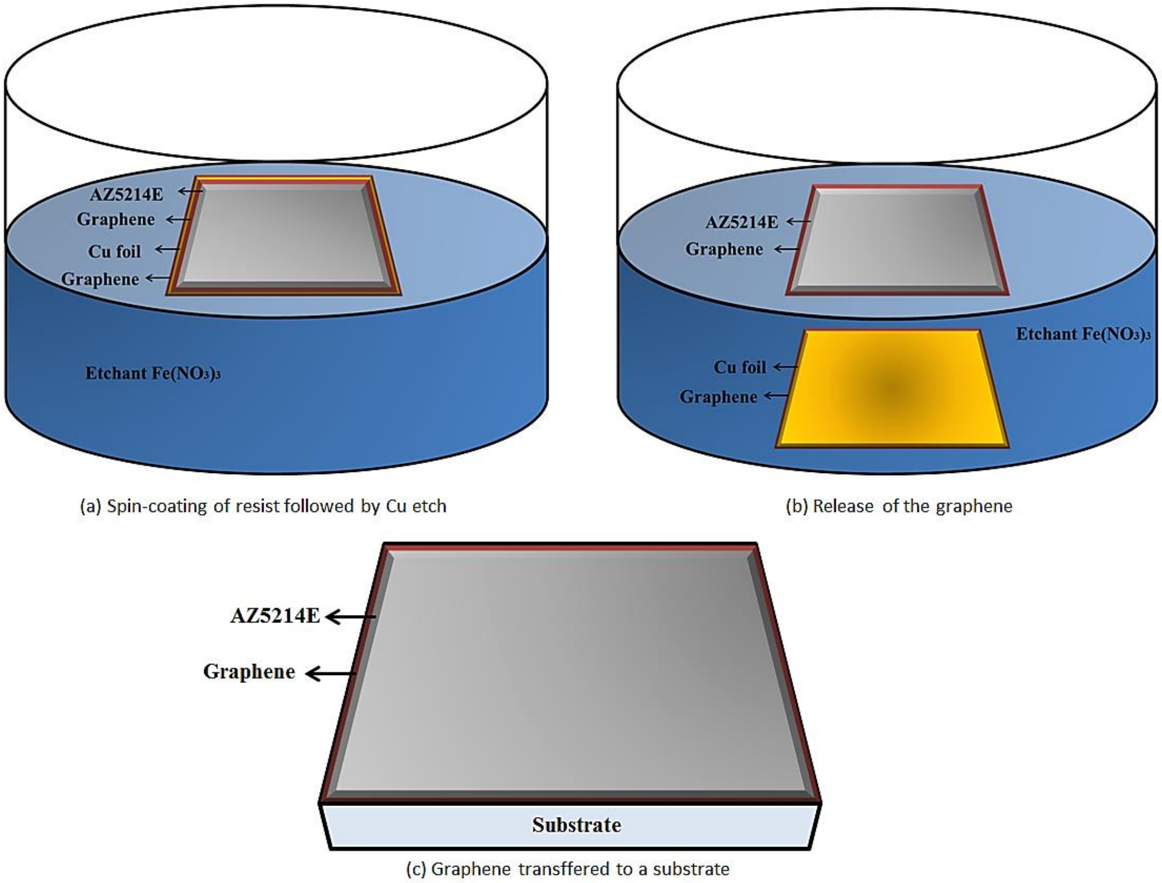

(a) Spin-coating of resist followed by Cu etch

(b) Release of the graphene

(c) Graphene transffered to a substrate

Figure 3.11 Schematic illustration of the standard process of graphene transfer

Pieces of 2"×4" SLG grown by CVD on Cu foil (GRAPHENE SUPERMARKET, Reading, Massachusetts, USA) are employed in the experiment. The SLG sheet is transferred to an NUV epi-wafer or a sapphire sample by a standard transfer process as shown in Figure 3.11: at the beginning, a layer of 2 μm photoresist AZ5214E is spin-coated onto the SLG and the AZ5214E/SLG stack is then released by etching the Cu foil in a $Fe(NO_3)_3$ solution (17 wt%) at room temperature. The AZ5214E/SLG stack floating in the solution is then washed by deionized (DI) water and transferred to the target substrate followed by drying at room temperature for 24 hours. Finally, the AZ5214E on the SLG is dissolved in acetone at room temperature.

Fabrication of the current spreading layers

Two types of CSLs, which are SLG/2 nm Ni/250 nm AZO (CSL A) and 2 nm Ni/250 nm AZO (CSL B), are fabricated on both NUV epi-wafers and sapphire samples for measurements of electrical properties and transmittance, respectively. The InGaN/GaN NUV LED epi-wafers are grown on a c-plane (0 0 0 1) sapphire by MOCVD CRUIS I. The grown LED epi-layer consists of a sequence of a 3.5 µm thick GaN buffer layer, a 2µm thick Si-doped n-GaN layer, nine periods of InGaN/GaN multiple quantum wells (MQWs), and finally a 130 nm thick Mg-doped p-GaN layer. In the fabrication process, first, a layer of 2 nm Ni is deposited by electron beam evaporation on the top of a NUV epi-wafer with a transferred 6x6 mm^2 SLG sheet. Afterwards, the Ni layer is treated by rapid thermal annealing in air at 525 ℃ for 5 minutes to increase its transparency. Subsequently, a layer of 250 nm AZO with a sheet resistance of 70 Ω/sq is deposited by a sputtering cathode TORUS using a ZnO target containing 2% Al_2O_3 [123]. Identical fabrication steps are also applied on the NUV epi-wafer without the SLG and also on sapphire samples with and without a SLG. Consequently, two types of CSLs are fabricated on both the NUV epi-wafers and the sapphire samples. In the end, for the NUV epi-wafer with the CSL A (sample A) and for the NUV epi-wafer with the CSL B (sample B), a diamond pen is used to expose the n-GaN layer and indium spheres are added to their p-GaN and n-GaN surfaces for current injection, respectively, as shown in Figure 3.12. In addition, Si samples with the surface partially covered by gold (Au) and partially covered by SLG, AZO or Ni are fabricated assisted with standard photolithography and lift-off processes for work function measurements.

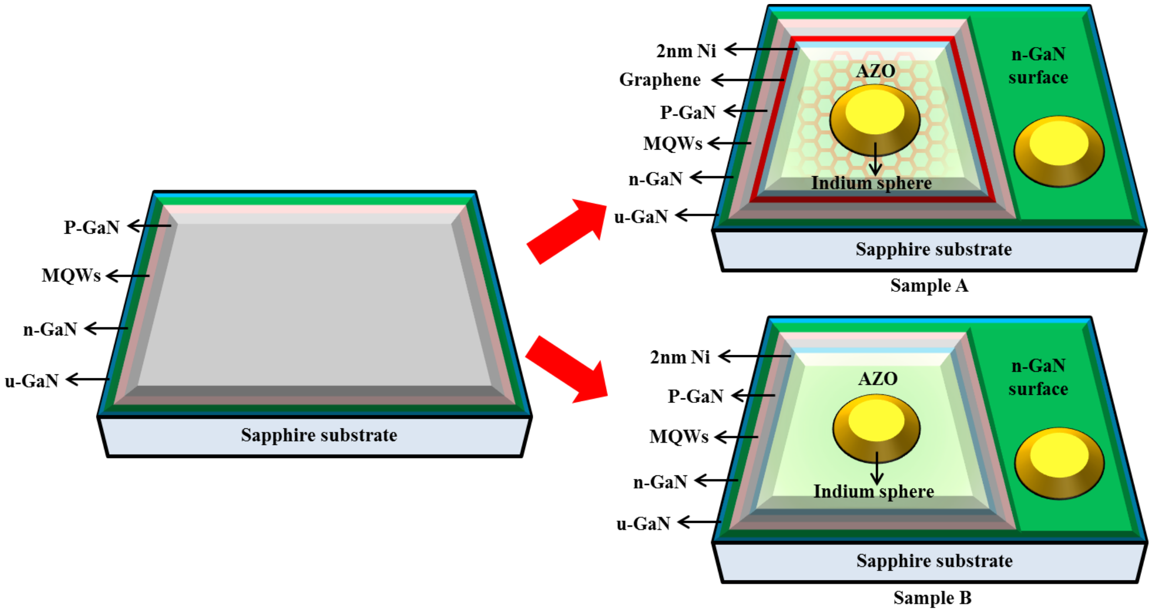

Figure 3.12 Schematic illustration of the structure of the NUV epi-wafer (left) and the fabricated sample A with the CSL A of SLG/Ni/AZO and the sample B with the CSL B of Ni/AZO (right) both using indium spheres for carrier injection

Characterization

The transmittance of the CSLs on the sapphire substrates is measured using an OL 700-71 6-inch diameter integrating sphere system assisted with a Xenon lamp and a CAS 140-B optical spectrometer. The thickness of the transferred SLG sheet is characterized by Raman spectroscopy, using a DXRxi Raman imaging microscope (Thermo Scientific, Waltham, Massachusetts, USA). The Raman spectrum of the graphene is recorded with an integration time of 25 seconds, using a 633 nm laser with a power of 8 mW. The EL spectra are obtained using a fiber-coupled optical spectrometer. The I-V curves from the LEDs are obtained using a Model 2450 Interactive SourceMeter instrument system. The work function measurements are carried out using PeakForce Kelvin probe force microscopy of a Dimension Icon atomic force microscope (AFM) (Bruker, Billerica, Massachusetts, USA).

3.3.2 Characterizations

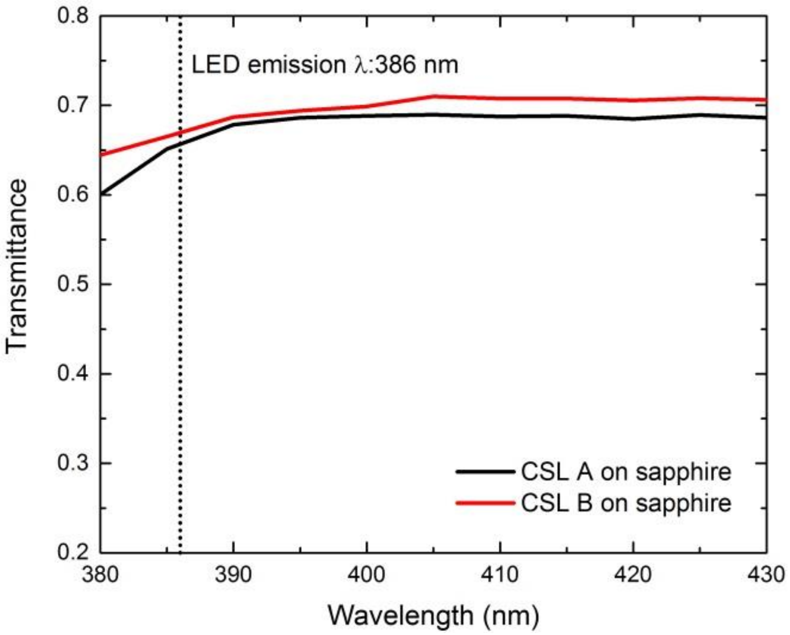

Figure 3.13 Optical transmittance spectra of a SLG/Ni/AZO CSL (CSL A) and a Ni/AZO CSL (CLS B) on sapphire samples in a wavelength range of 380-430 nm

The transmittance for the two types of CSLs deposited on sapphire samples is measured in the wavelength range of 380-430 nm, as shown in Figure 3.13. For the CSL B on sapphire, the transmittance is 66% at 386 nm while the CSL A on sapphire only suffers a small transmittance loss at 386 nm by adding the SLG interlayer and confirming the high transparency of SLG in the NUV wavelength region.

Figure 3.14 shows the Raman spectrum obtained by measuring the SLG transferred onto sample A. There are two dominant peaks which are the G peak at ~1580 cm^{-1} and the 2D peak at ~2700 cm^{-1} in the Raman spectrum of the SLG confirming the existence of the transferred SLG. The G to 2D peak intensity ratio identifies the thickness of the graphene layer. In our case, the value of IG/I2D is smaller than one (IG/I2D =0.67) with a full width at half maximum of ~60 cm^{-1} indicating the graphene layer is a SLG [124, 125].

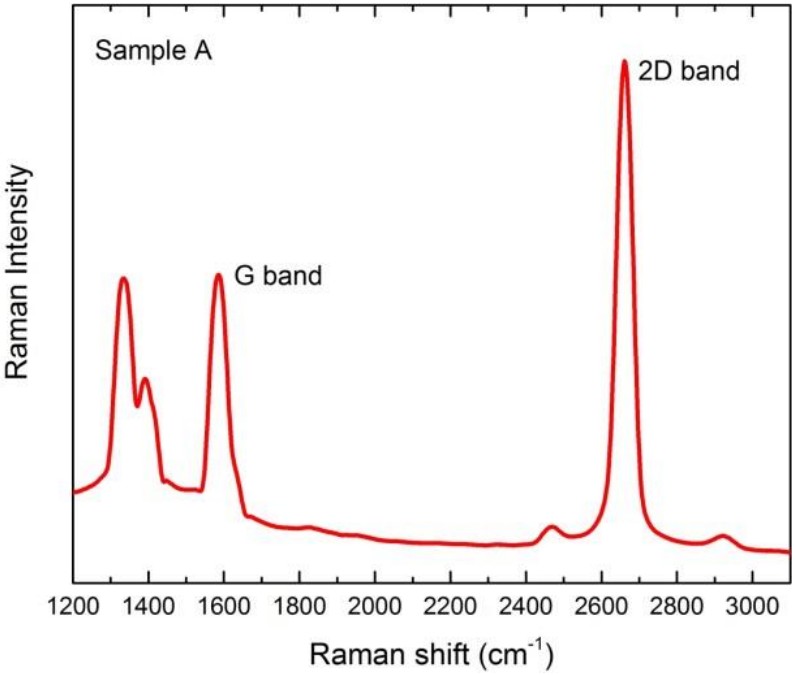

Figure 3.14 Raman spectrum of the transferred SLG on sample A collected using a 633 nm laser with a power of 8 mW

The EL emissions are obtained for both sample A and sample B. During the measurement, probes are pressed against the indium spheres on the p-GaN and the n-GaN layers for carrier injection. Figure 3.15 (a) shows a photograph of sample A during light emission under an injection current of 50 mA. Figure 3.15 (b) shows the EL spectra of sample A and sample B. The EL spectra are collected from the backside of the samples at a drive current of 50 mA and the peak emission is measured to be at around 386 nm. The emission intensity of sample A is 95% stronger than that of sample B at the peak wavelength.

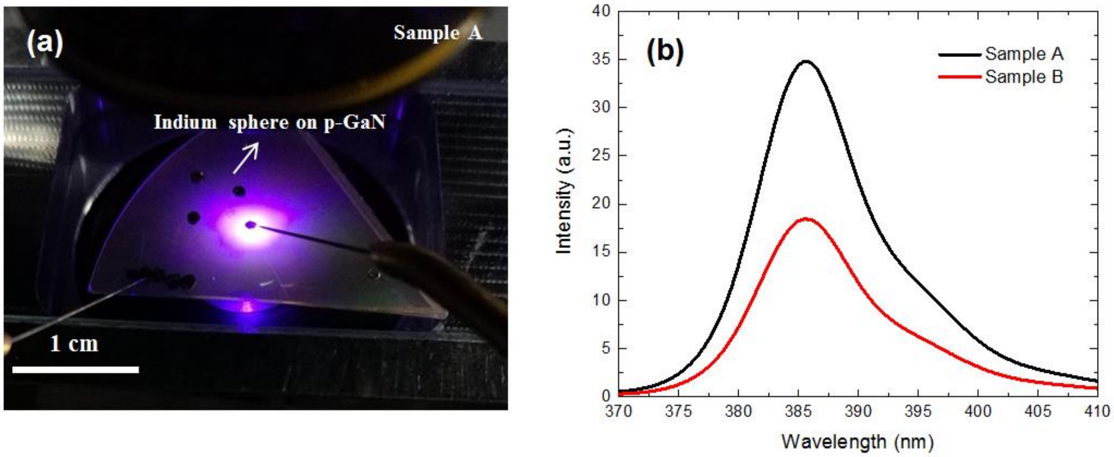

Figure 3.15 (a) Photograph of sample A during light emission at an injection current of 50 mA; (b) EL spectra of sample A (with SLG) and B (without SLG) at an injection current of 50 mA

In addition, Figure 3.16 shows a 0.5% reflectance difference at 386 nm between CSL A (15.5%) and CSL B (15%) on sapphire samples and this indicates that the 95% EL enhancement is not dominantly induced by the reflectance difference.

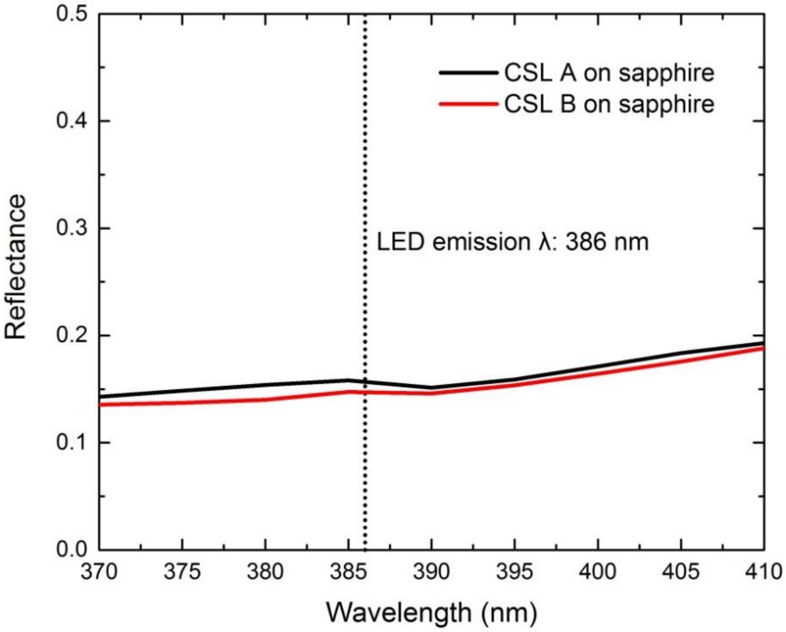

Figure 3.16 Optical reflectance spectra of a SLG/Ni/AZO CSL (CSL A) and a Ni/AZO CSL (CLS B) on sapphire samples in a wavelength range of 370-410 nm

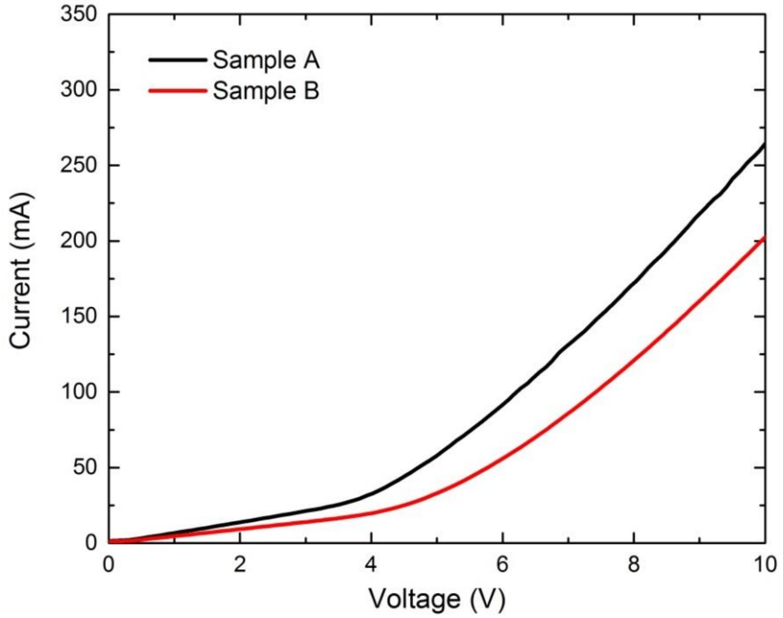

Figure 3.17 I-V curves of sample A (with SLG) and B (without SLG) for an input voltage range of 0-10 V

Furthermore, the I-V characteristics of sample A and sample B are measured and the results are shown in Figure 3.17. The current is measured by applying a voltage range of 0-10 V and the NUV emission starts at around 4 V for both samples. The forward voltage at an injection current of 50 mA is 4.6 V for sample A and 5.8 V for sample B. By fitting to the I-V curves after the turn-on, around 40% larger series resistance of sample B (37 Ω) than that of sample A (26 Ω) is shown due to the absence of a SLG interlayer in sample B.

To study the physics behind the EL enhancement by applying the SLG interlayer, work function measurements are carried out and the results are shown in Figure 3.18. As indicated in the graph, SLG (4.85 eV) has a higher work function than Ni (4.48 eV) and AZO (4.74 eV). The Ni layer deposited for work function measurement is also treated by rapid thermal annealing in air at 525 ℃ for 5 minutes. The higher work function of SLG than that of Ni or AZO causes a reduction of the SBH at the interface of the contacting layer and the p-GaN consequently allowing an easier carrier injection process through the p-GaN layer [71-73]. A simplified performance comparison as a contact layer on p-GaN between SLG and AZO can be made. According to the reported curve in [72] demonstrating the relationship between work functions and contact resistances, the work function difference of 0.11 eV between AZO and SLG leads to a 1.5 times larger contact resistance of AZO on p-GaN. This can be estimated that, in contrast with AZO, the current through the SLG interlayer can be increased by 50% under an identical voltage when the other relevant resistances are kept identical. This estimated result is comparable to the 40% increase for the current measured on sample A at 8 V shown in Figure 3.17. The comparison is made to AZO instead of Ni because in this work the employed 2 nm thin thickness and the 525 ℃ annealing temperature for Ni can lead to self-organization of Ni into nanoscale islands hence letting AZO in contact with p-GaN [126].

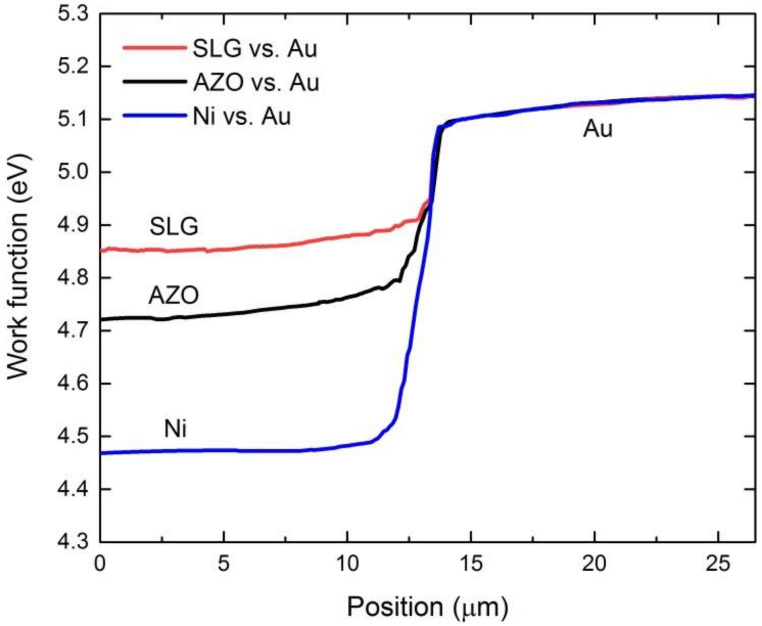

Figure 3.18 Work functions of SLG, AZO and Ni (left region) in comparison with that of Au (right region)

3.3.3 Conclusion

In conclusion, two types of CSLs which are SLG/Ni/AZO and Ni/AZO are successfully fabricated. This is done by using a standard graphene transfer process followed by deposition of Ni and AZO on both the p-GaN layer of the InGaN/GaN-based NUV-LED epi-wafers and the sapphire substrates. The graphene sheet is identified by micro-Raman spectroscopy confirming its type of SLG. A 95% EL enhancement is achieved for the epi-wafer with the SLG interlayer. Then, the I-V curves show that the LED without the SLG interlayer can possess a 40% larger series resistance. Furthermore, the transmittance of the SLG is measured and it shows a low transmittance reduction at a wavelength of 386 nm indicating its high transparency in the NUV range. The results show that SLG interlayers can be employed to improve the performance of the AZO based CSLs on the GaN based NUV LEDs.

3.4 Summary

In this chapter, in order to find a CSL with a higher transmittance in the NUV wavelength region than that of the Ni/Au CSL, a promising transparent conductive material AZO is investigated as a CSL on the NUV LED device. In the beginning, the AZO CSL is compared with the ITO CSL, which is one of the most popular transparent conductive materials in the LED application, regarding both the optical and electrical properties. The transmittances of the ITO and AZO CSLs are both around 70%. However, the ITO CSL shows better electrical properties including the EL, the series resistance and the contact resistivity than those of the AZO CSL. Therefore, although AZO is a low-cost indium-free material, its electrical performance as a CSL on the NUV LED still requires optimizations in order to replace the ITO CSL.

To improve the performance of the AZO, three types of AZO based CSLs, which are the AZO CSL, the Ni/AZO CSL and the SLG/Ni/AZO CSL, are fabricated for optical and electrical characterizations, respectively. According to the measurements, all the AZO based CSLs present high transparency in the NUV wavelength region and NUV EL emissions are obtained for all the three types of LEDs.

The comparison between LEDs with the AZO CSL and the Ni/AZO CSL shows that the Ni interlayer can improve the electrical performance of AZO. The LED with the Ni/AZO CSL presents both an enhanced EL and also a reduced series resistance relative to the LED with the AZO CSL.

Performance comparisons are also made between LEDs with the Ni/AZO CSL and the SLG/Ni/AZO CSL. The characterization results indicate that, by the employment of the transparent conductive SLG interlayer, the series resistance and the EL of the LED are further improved in comparison with that of the LED with the Ni/AZO CSL. The further improved electrical performance can be explained by the higher work function of SLG than that of AZO. Based on the optical and electrical characterizations, it can be concluded that the SLG interlayer can improve the performance of the NUV LED with the AZO based CSL.

Chapter 4 Adhesive bonding for hybrid warm white light-emitting diodes

In this chapter, a bonding method to combine an NUV LED and an f-SiC epi-layer is demonstrated in order to fabricate a hybrid f-SiC based warm white LED. After bonding and adding contacts, characterizations followed by discussions on the hybrid LED are carried out regarding both the bonding quality and the EL emission.

4.1 Adhesive bonding

The novel concept of f-SiC based white LED is introduced in chapter 1. It consists of an NUV LED and a donor and acceptor co-doped f-SiC substrate, which serve as the excitation source and the wavelength-conversion material, respectively. One fabrication approach to realize this f-SiC based white LED is to combine the NUV LED and the f-SiC substrate through adhesive bonding.

The adhesive bonding is one of the most widely used bonding techniques for combining two surfaces together. It employs intermediate adhesive layers between opposing surfaces. In a standard process of adhesive bonding, at least one of the surfaces to be bonded will be covered by an adhesive layer.

Subsequently, the two surfaces will be brought into close contact under a certain pressure. Then, the adhesive layer turns from a liquid or viscoelastic state into a solid state through treatment with heat or exposure by UV light [127]. By this way, the surfaces are bonded together.

The advantages of the adhesive bonding include low bonding temperatures, insensitivity to surface topography, resilience to stress and mechanical vibrations and uniform load distribution over a wide area, which makes itself extremely attractive in applications such as three-dimensional integrated circuits, advanced packaging, microfluidics and fiber–optic assemblies [127-132]. In comparison, for fusion bonding techniques, two opposing surfaces are required to be in sufficiently close contact in order to form covalent- or van der Waals bonds, which are the most important bonding mechanisms. Generally, the distance between atoms from two surfaces to be bonded should be less than 0.5 nm, which makes it difficult to fusion bond surfaces with a large roughness, as shown in Figure 4.1 (a) [127]. In this case, as shown in Figure 4.1 (b), flowable adhesives can be applied in between the surfaces to pave the roughness hence bringing the atoms of adjacent surfaces into sufficient vicinity to generate the van der Waals bond, which is the basic mechanism in adhesive bonding [127-129].

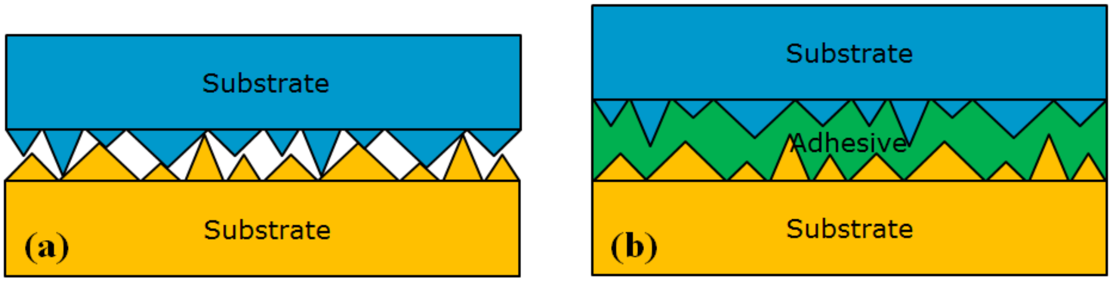

Figure 4.1 Schematic illustration of (a) fusion bonding and (b) adhesive bonding of rough samples

4.2 Adhesive bonding using hydrogen silsesquioxane

Although the adhesive bonding is straightforward to operate and less critical on surface roughness, high transparency of the adhesive material in the NUV wavelength region is indispensable for the application of hybrid f-SiC based white LED. An adhesive material with high transparency can maximize the NUV light propagating to the f-SiC epi-layers for excitation.

The high transmittance (above 90%) of HSQ in the NUV range makes itself an attractive bonding material in NUV LED related applications. Compared to the reported transmittance of the widely used BCB or SU-8 in adhesive bonding, HSQ appears more advantageous in the NUV wavelength region with higher and more uniform transmittance [133-136]. Therefore, adhesive bonding by HSQ is a promising candidate for the fabrication approach of f-SiC based white LEDs.

HSQ, which belongs to the inorganic compounds, is commercially available in a carrier solvent of methyl isobutyl ketone (MIBK) as Fox (flowable oxide). It is widely used in micro- and nano-engineering applications, e.g., as a high-resolution negative electron beam resist [137], as molding material in nanoimprint lithography [138] or as mask in dry etching processes [139]. Furthermore, it is also employed as an intermediate material in bonding processes. Successful cases have been carried out for materials including Si, GaN and AlGaN [140-145]. In these bonding cases, HSQ is employed to bring atoms of opposing surfaces into vicinity to form van der Waals bonds. Under a certain heating temperature, the HSQ layer will be converted into solid SiO_x and become competent in bearing the force to combine the opposing surfaces [140]. In the following sections, the work regarding adhesive bonding using HSQ will be demonstrated in detail.

4.2.1 Bonding tests

The plan of bonding tests is briefly described below. Tests of adhesive bonding using HSQ are carried out on Si samples first. After the bonding tests using Si samples, bonding tests on Si and SiC samples followed by SiC and SiC samples are done. Then, bonding between SiC and f-SiC is tested and, finally, the bonding of the NUV LED and the f-SiC samples is completed.

One of the reasons why Si is employed as the test material is due to its lower price relative to that of SiC. Also, for HSQ bonding of Si, reported successful cases can be found. Therefore, it is applicable to use Si to test the bonding parameters including temperature, pressure and time. Furthermore, the thermal expansion coefficient (TEC) difference between Si and SiC is acceptable. The TEC of a material can affect the bonding process, e.g., large TEC difference of two surfaces can lead to bad bonding quality or even a failure [146]. Table 4.1 shows the TEC of several materials at 20 °C [147]. There has been a successful case of HSQ bonding of Si and GaN, proving that HSQ can work with both Si and GaN surfaces with a TEC difference [140]. The TEC difference between Si (2.56 $10^{-6}K^{-1}$) and GaN (3.1 $10^{-6}K^{-1}$) is 20.1% while the TEC difference between Si (2.56 $10^{-6}K^{-1}$) and SiC (2.77 $10^{-6}K^{-1}$) is only 8.2% indicating that using Si samples for HSQ tests can be feasible.

Table 4.1 Linear thermal expansion coefficient of materials at 20℃ [147]

Material	Si	SiC	GaN
Thermal expansion coefficient ($10^{-6}K^{-1}$)	2.56	2.77	3.1
Difference relative to Si	0%	8.2%	20.1%

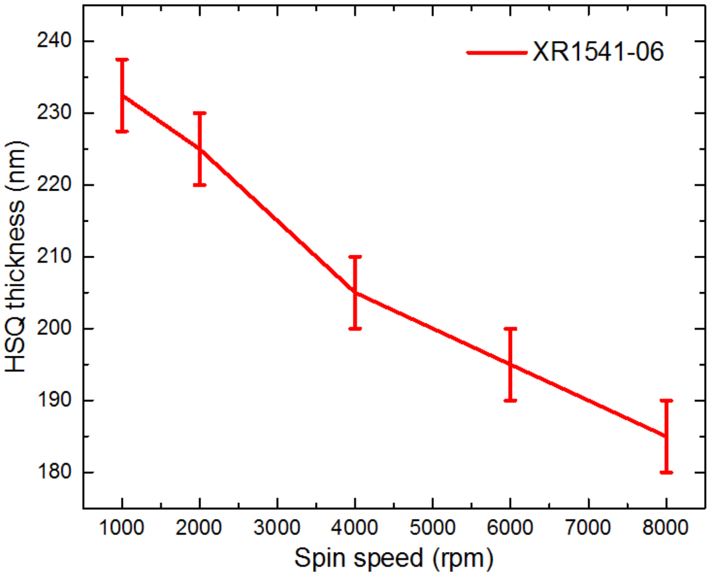

Figure 4.2 HSQ thickness dependence on spin speeds

The thickness dependence of HSQ (XR-1541-06 from Dow Corning Corporation) on spin speeds is tested and shown in Figure 4.2. The thickness changes from 185 nm to 230 nm when the spin speed alters from 8000 revolutions per minute (rpm) to 1000 rpm. A HSQ layer with the largest thickness around 230 nm, formed by a spin speed of 1000 rpm, is employed to pave the surface roughness. By spin-coating, HSQ is applied on the font side of a Si sample and the Si sample is then placed beneath another Si sample with front sides in contact, as shown in Figure 4.3 (a), followed by the bonding process.

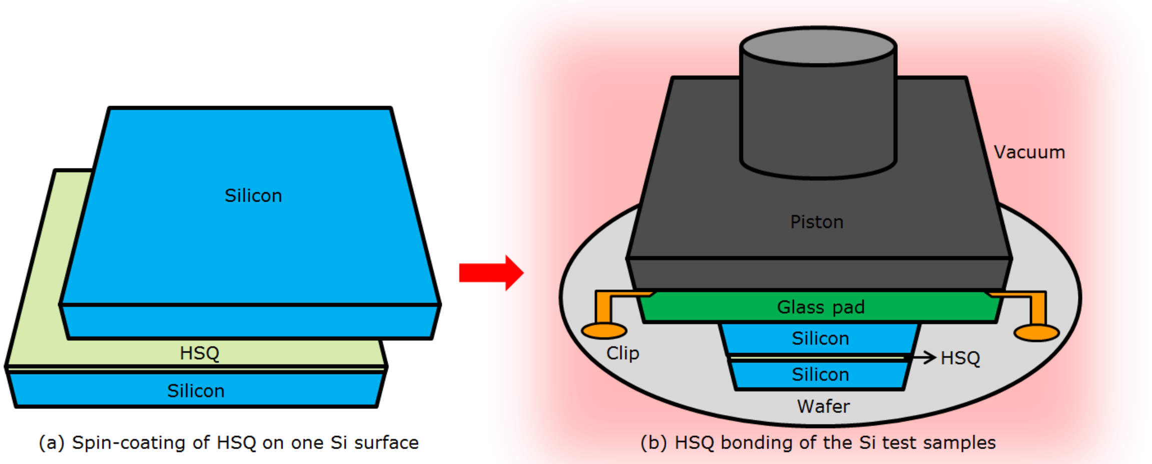

(a) Spin-coating of HSQ on one Si surface

(b) HSQ bonding of the Si test samples

Figure 4.3 Schematic illustration of the bonding process of Si samples assisted with a HSQ layer spun on one of the Si surfaces

During bonding, the stack is placed on a carrier wafer to prevent resist from flowing and staying in the bonder chamber, as shown in Figure 4.3 (b). A glass pad is employed to fix the samples to be bonded assisted with clips. The bonding is carried out under vacuum. A pressing force is applied to make a close contact between atoms. The chamber temperature is heated up to make the resist convert into solid SiO_x. The force and the temperature last for a certain time before the bonding ends. A more detailed process will be introduced in the following introduction of bonding between NUV LED and f-SiC samples.

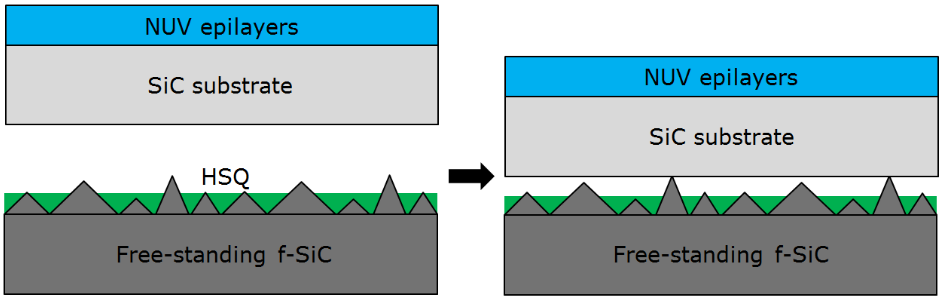

Figure 4.4 Unsuccessful bonding using one layer of HSQ

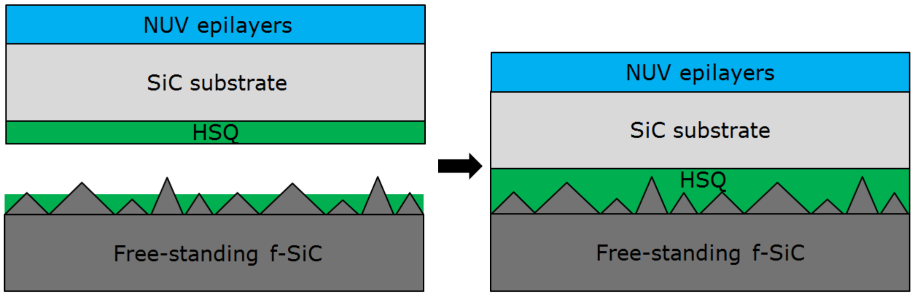

Figure 4.5 Successful bonding using two layers of HSQ

After the successful Si-Si bonding, Si-SiC bonding and SiC-SiC bonding also work well. The test SiC samples are from commercial 4H-SiC wafers. However, the bonding between SiC and f-SiC is not working at the beginning. This is because of the larger roughness of f-SiC than that of commercial SiC and Si samples. The roughness (arithmetic mean height) of the Si sample front side is measured by vertical scanning interferometry (VSI) on a PLU NEOX 3D Optical Profiler (Sensofar, Terrassa, Spain). It turns out to be around 3 nm for Si samples and around 10 nm for the 4H-SiC samples, respectively. But the roughness is around 100 nm for the backside (the polished side to be bonded) of the free-standing f-SiC epi-layer. As shown in Figure 4.4, the employed HSQ layer is not thick enough to completely cover the roughness of the f-SiC surface. Consequently, atoms from the two opposite surfaces cannot be brought into sufficient vicinity resulting in a failure. To overcome this issue, the HSQ resist thickness is adjusted. As shown in Figure 4.5, to have the f-SiC surface roughness completely covered, both the SiC surface and the f-SiC surface are spun on a layer of 230 nm HSQ. This enables the atoms at the opposing surfaces to be in sufficiently close contact allowing the van der Waals bonding to happen.

4.2.2 Bonding of the NUV LED and the f-SiC samples

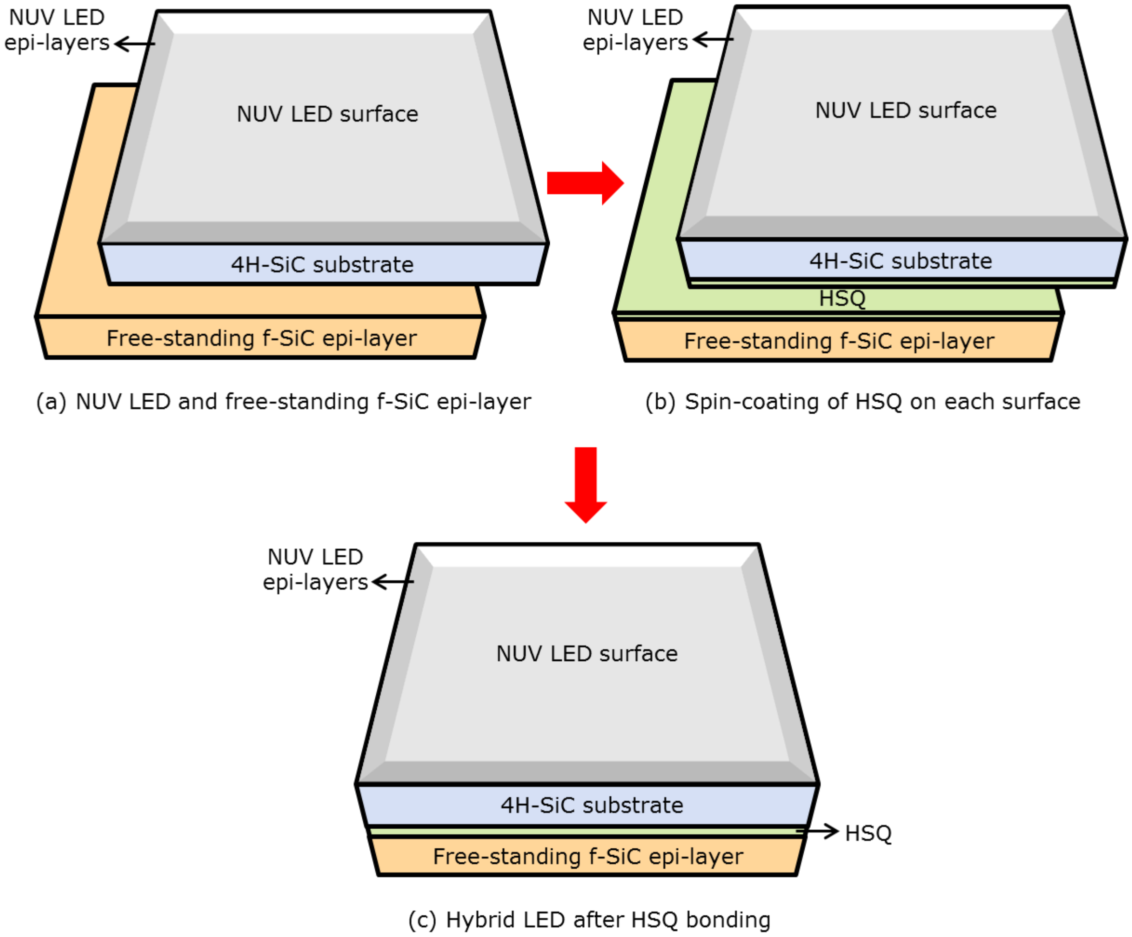

Figure 4.6 Schematic illustration of the bonding process of a NUV LED to a free-standing B-N co-doped f-SiC epi-layer assisted with HSQ layers spun on both SiC surfaces

After the tests, the bonding of an NUV LED and an f-SiC epi-layer is carried out. The NUV LED epi-layers are grown on a 2-inch (0001) 4H-SiC substrate by MOCVD (Cruis I, Aixtron, Germany). The grown LED epi-layer consists of a 3.6 μm thick AlGaN (5% Al) buffer layer, a 2 μm thick Si-doped n-AlGaN (7% Al) layer, nine periods of InGaN (3% In)/AlGaN (5% Al) MQWs, and finally a 85 nm thick Mg-doped p-AlGaN (2%) layer and a 32 nm thick Mg-doped p-GaN layer. The free-standing 200 μm B-N co-doped 6H-SiC (f-

SiC) epi-layer is grown on a 6H-SiC (0001) substrate with 1.4 degree off-axis by a fast sublimation growth process [1, 10]. After growth, the 6H-SiC substrate is polished away. As mentioned previously, the roughness is around 100 nm for the polished side of the free-standing f-SiC epi-layer and it is around 10 nm for the 4H-SiC substrate of the NUV LED.

The bonding process of the NUV LED and the f-SiC epi-layer is shown in Figure 4.6 (a)-(c). Both samples are cleaned by immersion in acetone for 10 min. Next, HSQ layers with a thickness of around 230 nm are spun on both the 4H-SiC substrate of the NUV LED and the polished backside of the free-standing f-SiC epi-layer. Then, the samples are placed on hotplates for baking at 150℃ for 1 minute followed by another baking at 200℃ for 1 minute to drive out the solvent. Afterwards, the NUV LED and the f-SiC epi-layer are placed on a holder with the surfaces covered by the HSQ layers in contact.

During the bonding in a Süss SB6 wafer bonder, firstly, vacuum pumping is carried out after the sample surfaces are in contact. Thereafter, the temperature is heated up to 400℃ under vacuum (10^{-4} mbar) with a ramping rate of 15℃ /minute. Then, at 400℃, a force is applied to the samples by a piston for 1 hour. The effective bonding pressure acting on the bond interface is around 250 N/cm^2. In the end, the sample is cooled down with a ramping rate of 10℃ /minute After successful bonding, a diamond pen is used to expose the n-AlGaN layer of the NUV epi-wafers and indium spheres are added to the p-type and n-type surfaces, respectively, for electric current injection.

4.3 Characterizations

After fabrication, bonding quality and EL performance of the hybrid LED are characterized. The characterization results are demonstrated below.

Transmittance of the HSQ intermediate layers

Characterizations on the hybrid f-SiC based LED sample after bonding are carried out. The transmittance of the HSQ layer is measured by a 6-inch integrating sphere system assisted with a Xenon lamp and a CAS 140-B optical spectrometer. The measurement is carried out on a test sample where HSQ is spun on top of a pure sapphire substrate.

Figure 4.7 shows the transmittance spectrum of a 230 nm HSQ layer after normalization of the 86% transmittance of the sapphire substrate. Unlike the sharp transmittance drop of SU-8 in NUV wavelength region [135], the transmittance of HSQ appears quite uniform in the measured wavelength range from 370 nm to 420 nm. At 390 nm, which is the peak wavelength of the employed NUV LED, the transmittance is 98% for the 230 nm HSQ layer. Then the transmittance of a 460 nm HSQ layer can be estimated to be around 96% resulting from 98%×98%. The 96% transmittance at 390 nm is comparable to the HSQ transmittance shown in [134]. It confirms the possibility of using HSQ as the adhesive bonding material in the NUV LED-related application due to its high transparency.

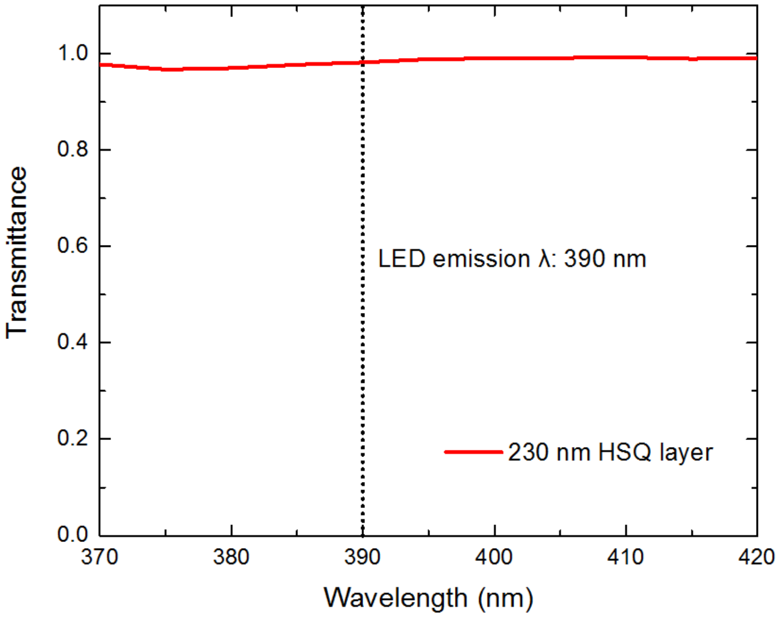

Figure 4.7 Optical transmittance spectrum of a 230 nm HSQ layer after normalization of the sapphire substrate in a wavelength range of 370-420 nm

Bonding quality of the hybrid LED

The cross section of the bonded SiC samples with the HSQ interlayer is inspected by a Supra 40 VP SEM at 5 kV. Figure 4.8 shows the cross-section of the cleaved interface between the NUV LED and the f-SiC epi-layer inspected by SEM. As shown in the figure, two layers of 230 nm HSQ, which results in a total thickness of 460 nm, are in contact with the upper f-SiC epi-layer and the lower 4H-SiC substrate of the NUV LED. The HSQ and the SiC surfaces are intimately combined without delamination, which suggests a good adhesion of the 460 nm HSQ interlayer to both the 4H-SiC surface and the surface of the free-standing f-SiC epi-layer. No voids and defects at the HSQ/SiC or HSQ/HSQ interfaces are observed indicating good bonding quality by the HSQ bonding approach.

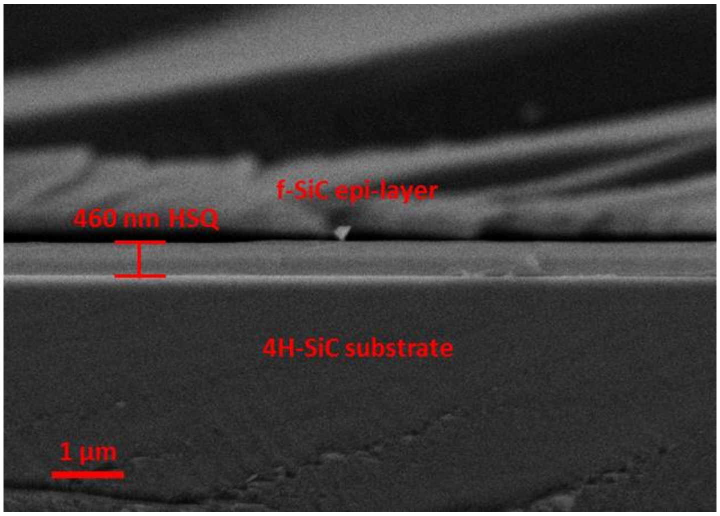

Figure 4.8 SEM inspection of the cross section of the bonded stack using 460 nm HSQ in between showing no voids

Figure 4.9 shows a photograph of the hybrid LED fabricated by HSQ bonding, i. e., with the HSQ intermediate layer embedded in it. In the figure, the indium spheres are added to the NUV LED upper surface as metal contacts for electric current injection and the free-standing f-SiC epi-layer is beneath the NUV LED chip. No voids and defects are observed by shining white light through the hybrid LED demonstrating again the good bonding quality by HSQ. Letters in the background indicate the white light transparency of the hybrid LED which confirms the feasibility of using white light to visualize the defects.

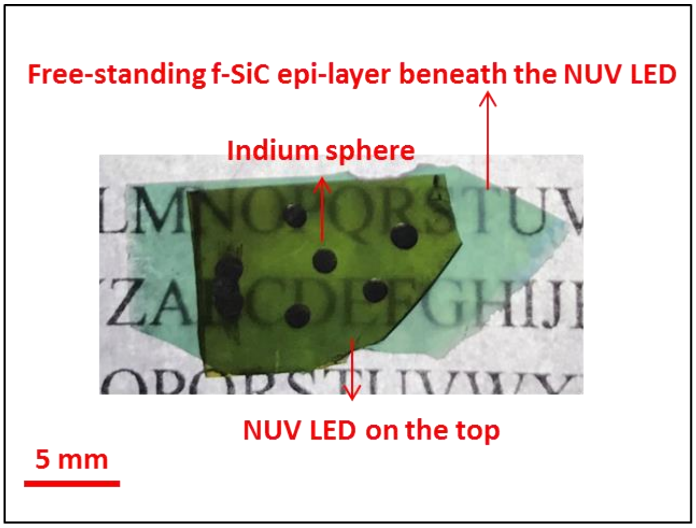

Figure 4.9 Photograph of the hybrid LED with the HSQ intermediate layer embedded in it

EL of the hybrid LED

Figure 4.10 shows a schematic illustration of the hybrid LED fabricated by bonding after exposing the n-AlGaN of the NUV LED on the top by a diamond pen. Then, electric current can be injected by pressing probes against the indium spheres added on the surfaces.

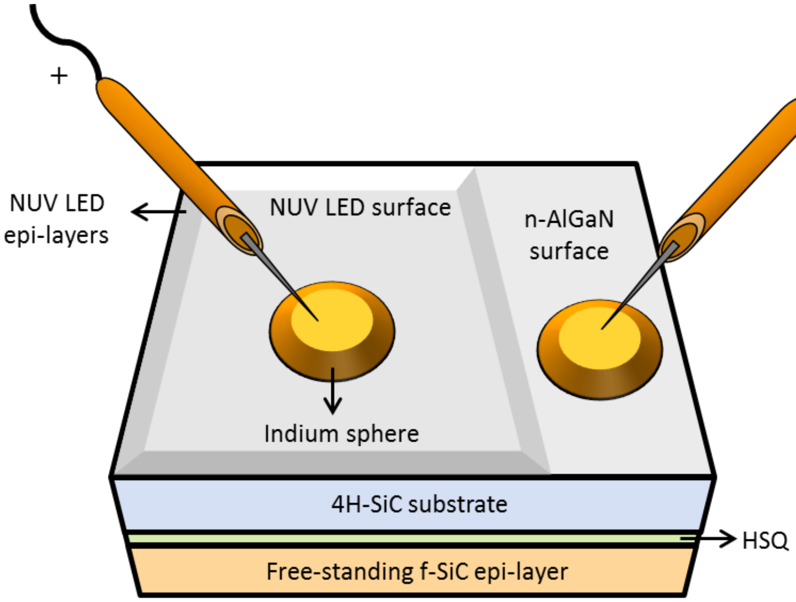

Figure 4.10 Schematic illustration of the hybrid LED with indium spheres on the NUV LED for electric current injection through probes

The EL emission is successfully obtained for the hybrid LED as shown in Figure 4.11. Figure 4.11 shows a photograph with electric current injection under natural ambient illumination, which is taken from the backside of the hybrid LED (the f-SiC epi-layer side). The hybrid LED is placed on a transparent glass slide in contact with the f-SiC epi-layer while the NUV LED on the top is connected to the probes. Indium spheres added on the top of the hybrid LED can be observed through the bonded NUV LED and f-SiC epi-layer. One probe is connected to the indium sphere on the n-type surface while the other one is connected to the indium sphere on the p-type surface. An electric current injected into the hybrid LED at 30 mA produces NUV emission which excites B-N co-doped f-SiC epi-layer. Finally, a warm white emission, which can be seen in the photograph of Figure 4.11, is obtained.

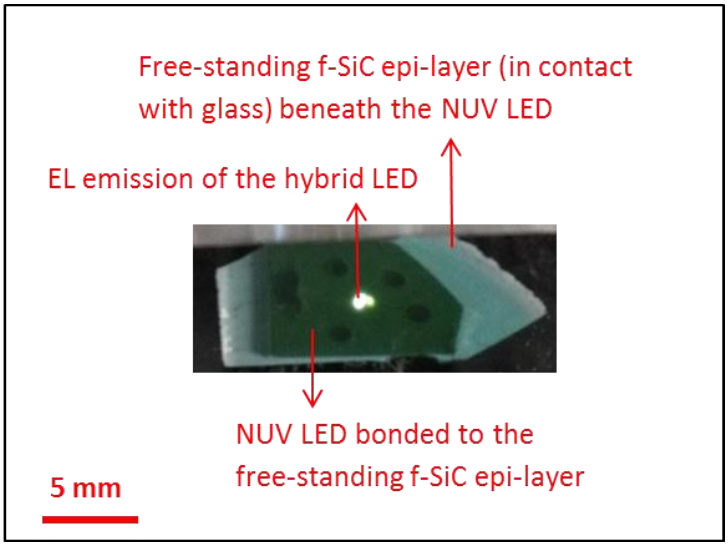

Figure 4.11 Photograph of the lighting hybrid LED from backside with an electric current injection at 30 mA

Figure 4.12 shows the EL spectra of the NUV LED solely before bonding (the upper curve) and the hybrid LED after bonding (the bottom curve) measured from the backside at 30 mA (the f-SiC epi-layer side for the hybrid LED). The emission is collected by a large-core optical fiber coupled to the CAS 140-B optical spectrometer. The electric current injection to the NUV LED is carried out by a Model 2450 Interactive SourceMeter instrument system.

The NUV LED before bonding presents a peak wavelength around 390 nm. After bonding, the emission of the f-SiC epi-layer by the excitation of the NUV photons can be clearly observed for the hybrid LED showing a peak emission wavelength around 550 nm, which is consistent with the expectation [2, 10].

Besides, Figure 4.12 also shows that, in comparison with the 390 nm peak wavelength of the NUV LED before bonding, the NUV peak wavelength shifts to around 405 nm after passing through hybrid LED. This can be explained by the inter-band absorption of the 6H-SiC, which absorbs photons possessing wavelengths shorter than around 408 nm [148, 149]. Hence, the long-wavelength photons (blue photons) can pass through the B-N co-doped 6H-SiC epi-layer leading to red-shift of the peak wavelength in the EL of the hybrid LED. In the end, the blue photons combined with the 550 nm-centered emission from the f-SiC epi-layer result in a warm white light as observed in Figure 4.11.

In the future, the performance of the hybrid LED can be further optimized. The 400 µm thick 4H-SiC substrate has a strong absorption in a wavelength range up to 387 nm according to its 3.2 eV optical bandgap. The NUV light generated by LED epi-layers on top has an emission wavelength of 390 nm, which will be partially absorbed by the 4H-SiC substrate. By employment of a thinner or more transparent SiC substrate and a NUV LED with longer emission wavelength, a hybrid LED with stronger EL intensity can be expected.

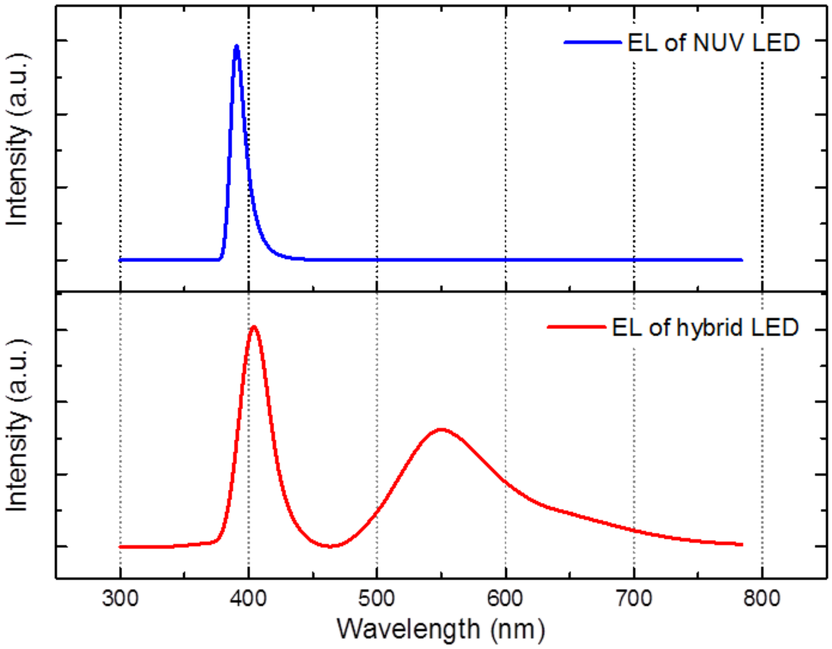

Figure 4.12 The EL spectra of the NUV LED before bonding and the hybrid LED measured from the backside at 30 mA

Efficiency of the hybrid LED

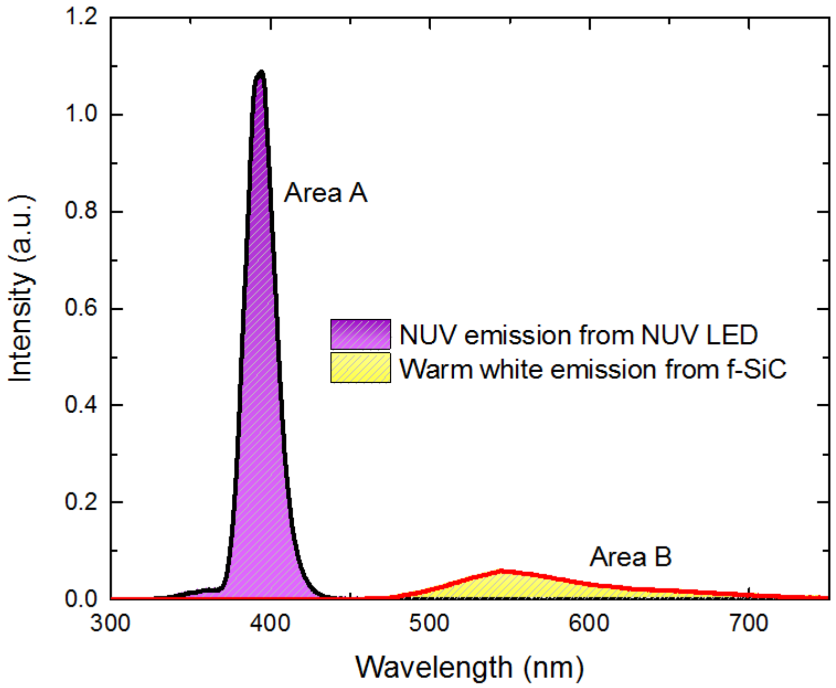

Figure 4.13 Relative intensity measured on the NUV LED and the hybrid LED

The efficiency of the hybrid LED can be expressed as below.

$$E = \frac{P_{out}\,(W)}{P_{in}\,(W)}$$

In the above formula, E, P_{out} and P_{in} stand for efficiency, output power and input power, respectively.

P_{in} can be calculated as below.

$$P_{in}\,(W) = I\,(A) \times V\,(V)$$

In the above formula, I and V stand for input current and input voltage, respectively. In this work, at 30 mA, the corresponding voltage is 22 V resulting in 0.66 mW as P_{in}.

P_{out} can be calculated as below.

$$P_{out}\,(W) = F\,(Wm^{-2}) \times A\,(m^{-2})$$

In the above formula, F and A stand for radiant flux density and emitting area, respectively. In this work the emitting area is around 1 mm^2.

Figure 4.13 shows the curve of monochromatic intensity measured on the hybrid LED and the NUV LED. The monochromatic intensity I_λ at a single wavelength is defined as the radiant flux density F per unit arc of solid angle and per unit wavelength ($\mathrm{Wm^{-2}sr^{-1}\mu m^{-1}}$).

The intensity (or radiance) I ($\mathrm{Wm^{-2}Sr^{-1}}$) of the hybrid LED can be calculated by integration of the I_λ of the hybrid LED over the emission range resulting in the yellow area in Figure 4.13.

$$I = \int_{450}^{700} I_\lambda d_\lambda = \text{Area B } (\mathrm{Wm^{-2}Sr^{-1}})$$

Then, F can be obtained from the intensity I by integration over a hemisphere. Then the P_{out} can be obtained using the 1 mm^2 emitting area to calculate the efficiency.

To estimate the conversion efficiency between the NUV emission and the f-SiC emission, the ratio between the intensity measured on the NUV LED (Area A) and the hybrid LED (Area B) can be calculated and an efficiency of around 21% is obtained in the end as shown below.

$$\frac{P_{out_{f-SiC}}}{P_{in_{NUV}}} \approx \frac{I_{out_{f-SiC}}}{I_{in_{NUV}}} = \frac{\text{Area B}}{\text{Area A}} \approx 21\%$$

In the above formula, $P_{out_{f-SiC}}$ and $P_{in_{NUV}}$ stand for the output power from the f-SiC and the input power from the NUV LED to the f-SiC, respectively.

4.4 Summary

In summary, the idea of this work is to fabricate a hybrid warm white f-SiC based LED through HSQ bonding. To start with, HSQ bonding tests are carried out on Si and SiC samples. After successful bonding tests, the adhesive bonding approach using HSQ is employed to successfully bond a NUV LED grown on a 4H-SiC substrate to a free-standing B-N co-doped f-SiC epi-layer. No voids are observed at the HSQ/SiC or HSQ/HSQ interfaces indicating a good bonding quality by this method. Strong EL emission of the hybrid LED is obtained by electric current injection at 30 mA. The NUV emission centered at 390 nm from the NUV LED on the top excites the bottom f-SiC epi-layer to generate a DAP emission centered at the wavelength of 550 nm finally presenting a warm white emission. In the future, the white light quality can be improved by employing an extra Al-N co-doped blue-emitting f-SiC epi-layer. From the results, it can be concluded that, HSQ bonding could be an effective approach in the SiC-based LED applications including the future fabrication of white LEDs based on B-N and Al-N co-doped f-SiC epi-layers.

Chapter 5 Conclusion and future perspective

A new type fluorescent silicon carbide (f-SiC) based white light-emitting diode (LED), which does not contain any rare-earth element or decaying phosphor, is introduced in the beginning of this thesis. This white LED can be realized by the combination of a near-ultraviolet (NUV) LED and an f-SiC substrate. In its structure, two adjacent f-SiC epi-layers, one doped by nitrogen (N) and boron (B) and the other one doped by N and Aluminum (Al), are employed as the wavelength-conversion materials while the NUV LED is used as the excitation source.

The main goal of this thesis is to realize the f-SiC based warm white LED. To achieve this purpose, the main focuses of the work include both the performance of the NUV LED and also the approach to combine the NUV LED and the f-SiC epi-layer. To be more specific, the relevant works include (1) LED post-growth processing on the NUV epi-wafer to fabricate NUV LED devices which can generate NUV light to excite the f-SiC epi-layer; (2) Performance optimization of transparent conductive material aluminum-doped zinc oxide (AZO) as the current spreading layer (CSL) of the NUV LED to enhance the NUV light to excite the f-SiC epi-layer; (3) Combination of the

NUV LED and the N-B co-doped f-SiC epi-layer through bonding in order to fabricate a hybrid LED emitting warm white light.

The NUV LED device with the conventional Ni/Au CSL is fabricated by a standard process followed by characterizations. In the fabrication, undesired small structures can be produced on n-GaN during the inductively coupled plasma (ICP) etch process and these structures can lead to severe pealing-off of n-pads resulting in an extremely low yield. In order to eliminate the undesired small structures, SiO_2 wet etch is employed for SiO_2 mesa fabrication instead of the reactive-ion etching (RIE) dry etch. By using the SiO_2 wet etch, the adhesion of the n-pads is increased. In the characterization, EL emission of the NUV LED device with a peak wavelength around 388 nm is obtained under an injection current of 20 mA. The LED device gives a turn-on voltage at around 3 V and a series resistance of around 27.8 Ohm. All these results confirm the good electrical properties of the Ni/Au CSL. However, a transmittance below 20% in the NUV wavelength region is obtained from the transmittance measurement on the Ni/Au CSL, which indicates the need for CSL with not only good electrical properties but also high transmittance in the NUV wavelength region.

As a promising indium-free transparent conductive material, AZO is investigated as a CSL on the NUV LED. First, comparisons are made between the AZO CSL and the ITO CSL. The results show that although the transmittances of the ITO and AZO CSLs are both much higher than that of the Ni/Au CSL, the ITO CSL shows much better electrical performance than the AZO CSL. This indicates the necessity of optimizations on the AZO CSL. To demonstrate that a Ni interlayer can improve the performance of the AZO CSL, NUV LED devices with two types of AZO based CSLs, which are the AZO CSL and the Ni/AZO CSL, are fabricated for comparisons. Transmittance measurements show that both of the AZO based CSLs present high transmittance in the NUV wavelength region. At the 386 nm peak wavelength, the transmittance of the AZO CSL is measured to be around 70%, while 67% for the Ni/AZO CSL. According to the I-V measurements, the device with the AZO CSL shows a 2.54 times larger series resistance than that of the device with the Ni/AZO CSL. Furthermore, NUV EL emissions are obtained under an injection current of 50 mA with peak wavelengths at around 386 nm for devices of both types. The device with the Ni/AZO CSL shows a 1.33 times stronger EL intensity at 386 nm when compared to the one with the AZO CSL. The characterization results indicate that the AZO based CSLs present high transmittance in the NUV wavelength region. However, although the Ni interlayer can improve the electrical performance of the AZO, it is still not as good as the ITO CSL. Therefore, methods for further improvement are required to obtain better performance of the AZO based CSLs.

To further improve the performance of the AZO-based CSLs, one approach is to lower the Schottky barrier height (SBH) at the contacting interface. This can be achieved through the employment of a material with a sufficiently high work function. Although it is difficult to find an appropriate CSL material having a sufficiently high work function (larger than 7.5 eV) for p-GaN, the SBH at the interface can be reduced by decreasing the difference. In this work, a single layer graphene (SLG) interlayer between the CSL and the p-GaN is used to further improve the performance of the AZO-based CSL in the application of NUV LEDs. Two types of CSLs which are Ni/AZO and SLG/Ni/AZO are fabricated for comparisons. The transmittance of the SLG is measured and it shows a low transmittance reduction at the LED peak wavelength of 386 nm indicating its high transmittance in the NUV wavelength region. In I-V characterization, it is shown that the LED without the SLG interlayer can possess a 40% larger series resistance. Furthermore, a 95% EL enhancement is achieved for the sample with the SLG interlayer at an electric current of 50 mA. The improvement of EL and I-V performance can be explained by the high work function of SLG. According to the optical and electrical characterizations, it can be concluded that SLG interlayers can improve the performance of NUV LEDs with AZO based CSLs.

To combine the NUV LED and the f-SiC epi-layer in order to produce the f-SiC based warm white LED, an approach of adhesive bonding is employed. Hydrogen silsesquioxane (HSQ) is used as the intermediate adhesive layer due to its high transmittance in the NUV wavelength region. Through the bonding assisted with HSQ, a NUV LED grown on a 4H-SiC substrate is successfully bonded to a free-standing B-N co-doped f-SiC epi-layer. By scanning electron microscopy (SEM), no voids are observed at the HSQ/SiC or HSQ/HSQ interfaces indicating a good bonding quality by this method. Strong EL emission of the hybrid LED is obtained by an injection electric current at 30 mA. The NUV emission centered at 390 nm from the NUV LED on the top excites the bottom f-SiC epi-layer to generate emission centered at the wavelength of 550 nm finally presenting a warm white emission. From the presented results, it shows that HSQ bonding could be an effective approach in the SiC-based LED applications including the future fabrication of white LEDs based on B-N and Al-N co-doped f-SiC epi-layers.

The above results show a bright prospect of the hybrid f-SiC based white LED as a potential alternative to the commercially popular white LED containing phosphors.

In the future research, to obtain better performance of the NUV LED as the excitation source, work on the transparent conductive CSL is needed to make a CSL with high NUV transmittance and good conductivity. Also, a reflector (such as Al or Ag) on the CSL is required to work together as a reflective CSL. The reflective CSL can reflect the NUV light, which is emitted by the NUV LED on top, all the way to the bottom f-SiC epi-layer hence providing a strong excitation.

In addition, more research efforts need to be devoted to maximize the NUV light from the NUV LED propagating to the f-SiC epi-layer through minimizing the NUV absorption by the SiC substrate. This can be achieved by growing the NUV epi-layers on a more transparent SiC substrate or producing a thinner SiC substrate by, for example, polishing.

Furthermore, to further improve the light quality of the hybrid f-SiC based white LED, combination of B-N and Al-N co-doped f-SiC epi-layers either by bonding or growth is necessary.

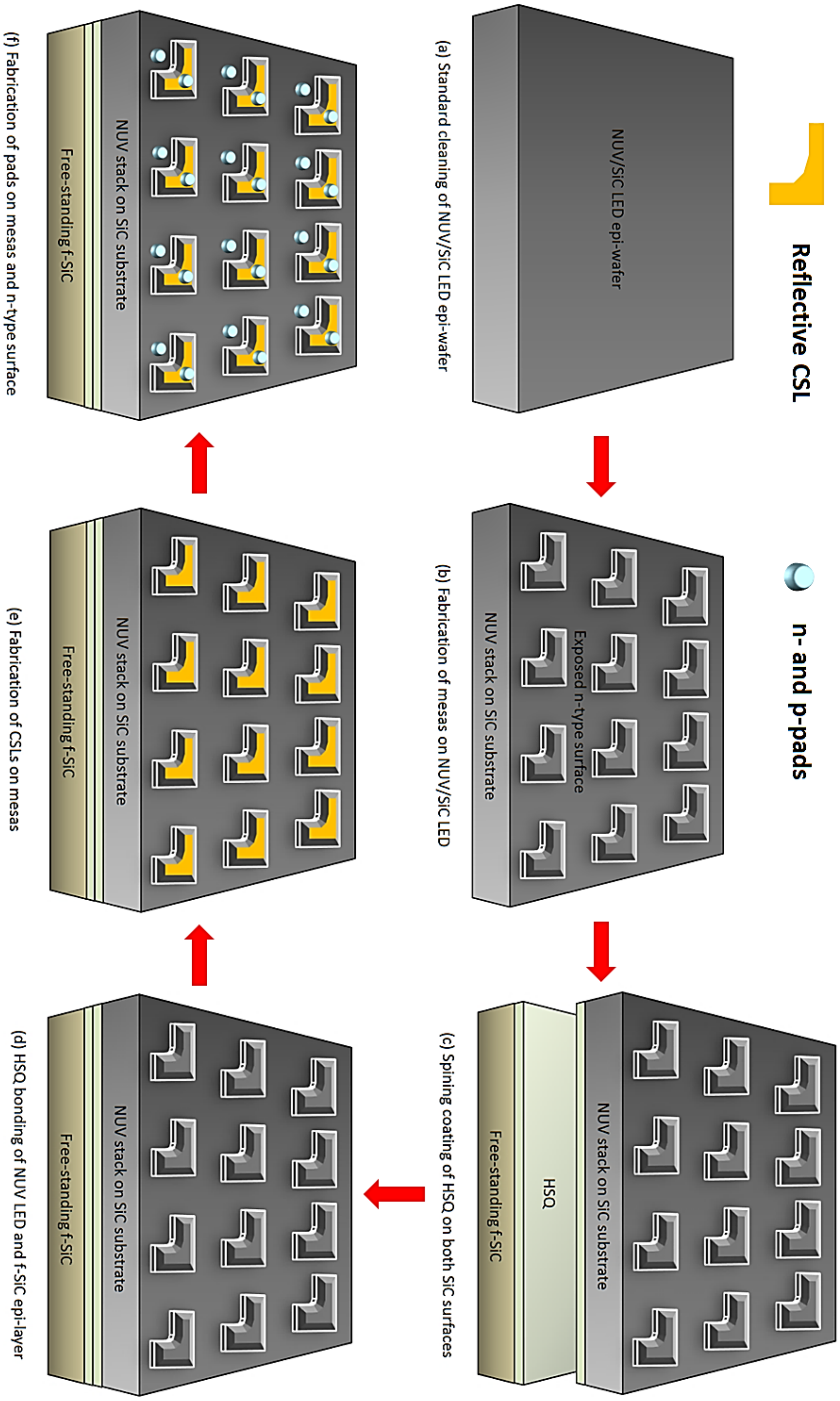

Figure 5.1 Schematic illustration of the fabrication of hybrid f-SiC based white LED devices

Last but not the least, in the future, f-SiC based white LED devices can be fabricated as shown in Figure 5.1 (a)-(f). The fabrication of the f-SiC based white LED devices can be realized by combining the standard fabrication process of the LED devices and the bonding of an NUV LED and an f-SiC substrate. Firstly, mesas are fabricated on the top of an NUV LED with a SiC substrate by a standard process. Afterwards, the NUV LED with mesas is bonded to a free-standing f-SiC substrate through HSQ adhesive bonding. Then, assisted with standard photolithography processes, reflective CSLs are deposited on the mesas of the LED followed by the formation of pads on the p- and n-type surfaces.

With the optimizations described above, a hybrid f-SiC based white LED with better performance can be expected in the soon future.

Bibliography

1 H. Ou, Y. Ou, A. Argyraki, S. Schimmel, M. Kaiser, P. Wellmann, M. K. Linnarsson, V. Jokubavicius, J. Sun, R. Liljedahl, and M. Syväjärvi, “Advances in wide bandgap SiC for optoelectronics” European Physical Journal B **87** (3), 58 (2014).

2 S. Kamiyama, T. Maeda, Y. Nakamura, M. Iwaya, H. Amano, I. Akasaki, H. Kinoshita, T. Furusho, M. Yoshimoto, T. Kimoto, J. Suda, A. Henry, I. G. Ivanov, J. P. Bergman, B. Monemar, T. Onuma, , and S. F. Chichibu, “Extremely high quantum efficiency of donor-acceptor-pair emission in N-and-B-doped 6H-SiC,” Journal of Applied Physics **99**, 093108 (2006).

3 S. Kamiyama, M. Iwaya, T. Takeuchi, I. Akasaki, M. Syväjärvi, and R. Yakimova, “Fluorescent SiC and its application to white light-emitting diodes” Journal of Semiconductors **32**(1), 013004 (2011).

4 S. Kamiyama, M. Iwaya, T. Takeuchi, I. Akasaki, R. Yakimova, and M. Syväjärvi, “White light-emitting diode based on fluorescent SiC” Thin Solid Films **522**, 23-25 (2012).

5 Y. Ou, doctoral dissertation “Fluorescent Silicon Carbide and its Applications in White Light-Emitting Diodes,” Technical University of Denmark (DTU) (2012).

6 C. Shen, K. Li, Q. L. Hou, H. J. Feng, and X. Y. Dong, “White LED based on YAG: Ce,Gd phosphor and CdSe-ZnS core/shell quantum dots,” IEEE Photonics Technology Letters **22**, 884–886 (2010).

7 Y. Ou, D. Corell, C. Dam-Hansen, P. Petersen, and H. Ou, “Antireflective sub-wavelength structures for improvement of the extraction efficiency and color rendering index of monolithic white light-emitting diode,” Optics Express **19**, A166–A172 (2011)

8 H. Yamamoto, “White LED phosphors: the next step,” Optical Components and Materials VII, International Society for Optics and Photonics, 759808 (2010).

9 M. Syväjärvi, J. Müller, J. W. Sun, V. Grivickas, Y. Ou, V. Jokubavicius, P. Hens, M. Kaisr, K. Ariyawong, K. Gulbinas, P. Hens, R. Liljedahl, M. K. Linnarsson, S. Kamiyama, P. Wellmann, E. Spiecker, and H. Ou, “Fluorescent SiC as a new material for white LEDs,” Physica Scripta **T148**, 014002 (2012).

10 Y. Ou, V. Jokubavicius, S. Kamiyama, C. Liu, R. W. Berg, M. Linnarsson, R. Yakimova, Mikael Syväjärvi, and H. Ou, “Donor-acceptor-pair emission characterization in NB doped fluorescent SiC” Optical Materials Express **1**(8), 1439-1446 (2011).

11 M. Razeghi, and M. Henini, *Optoelectronic devices: III-nitrides* (Elsevier, Oxford, 2004), Chap. III-nitride ultraviolet light emitting sources.

12 R. M. Guijt, and M. C. Breadmore, “Maskless photolithography using UV LEDs,” Lab on a Chip **8**(8), 1402-1404 (2008).

13 R. Ji, M. Hornung, M. A. Verschuuren, R. van de Laar, J. van Eekelen, U. Plachetka, M. Moeller, and C. Moormannc, “UV enhanced substrate conformal imprint lithography (UV-SCIL) technique for photonic crystals patterning in LED manufacturing,” Microelectronic Engineering **87**(5-8), 963-967 (2010).

14 M. A. Würtele, T. Kolbe, M. Lipsz, A. Külberg, M. Weyers, M. Kneissl, and M. Jekel, “Application of GaN-based ultraviolet-C light emitting diodes–UV LEDs–for water disinfection,” Water Research **45**(3), 1481-1489 (2011).

15 C. Y. Bing, A. A. Mohanan, T. Saha, R. N. Ramanan, R. Parthiban, and N. Ramakrishnan, “Microfabrication of surface acoustic wave device using UV LED photolithography technique,” Microelectronic Engineering **122**, 9-12 (2014).

16 A. Kheyrandish, M. Mohseni, and F. Taghipour, “Development of a method for the characterization and operation of UV-LED for water treatment,” Water Research **122**, 570-579 (2017).

17 Y. Muramoto, M. Kimura, and S. Nouda, “Development and future of ultraviolet light-emitting diodes: UV-LED will replace the UV lamp,” Semiconductor Science and Technology **29**(8), 084004 (2014).

18 H. P. Maruska, and W. C. Rhines, “A modern perspective on the history of semiconductor nitride blue light sources,” Solid-State Electronics **111**, 32-41 (2015).

19 R. M. Potter, J. M. Blank, and A. Addamiano, “Silicon Carbide Light-Emitting Diodes,” Journal of Applied Physics **40**(5), 2253-2257 (1969).

20 J. A. Edmond, H. S. Kong, and C. H. Carter, “Blue LEDs, UV photodiodes and high-temperature rectifiers in 6H-SiC,” Wide-Band-Gap Semiconductors, 453-460 (1993).

21 H. G. Grimmeiss, and H. Scholz, “Efficiency of recombination radiation in GaP,” Physics Letters **8**(4), 233-235 (1964).

22 H. P. Maruska, and J. J. Tietjen, “The preparation and properties of vapor-deposited single-crystal-line GaN,” Applied Physics Letters **15**(10), 327-329 (1969).

23 G. Siddiqi, Z. Pan, and S. Hu, *Semiconductors and Semimetals* (Elsevier, 2017), Chap. III–V Semiconductor Photoelectrodes, P. 87.

24 J. I. Pankove, E. A. Miller, and J. E. Berkeyheiser, “GaN blue light-emitting diodes,” Journal of Luminescence **5**(1), 84-86 (1972).

25 H. P. Maruska, W. C. Rhines, and D. A. Stevenson, “Preparation of Mg-doped GaN diodes exhibiting violet electroluminescence,” Materials Research Bulletin **7**(8), 777-781 (1972).

26 H. P. Maruska, D. A. Stevenson, and J. I. Pankove, “Violet luminescence of Mg-doped GaN,” Applied Physics Letters **22**(6), 303-305 (1973).

27 T. Mukai, M. Yamada, and S. Nakamura, “Characteristics of InGaN-based UV/blue/green/amber/red light-emitting diodes,” Japanese Journal of Applied Physics **38**(7R), 3976 (1999).

28 T. Mukai, S. Nagahama, N. Iwasa, M. Senoh, and T. Yamada, “Nitride light-emitting diodes,” Journal of Physics: Condensed Matter **13**(32), 7089 (2001).

29 S. Nakamura, and T. Mukai, “High-quality InGaN films grown on GaN films,” Japanese Journal of Applied Physics **31**(10B), L1457 (1992).

30 S. Nakamura, M. Senoh, and T. Mukai, “P-GaN/N-InGaN/N-GaN double-heterostructure blue-light-emitting diodes,” Japanese Journal of Applied Physics **32**(1A), L8 (1993).

31 S. Nakamura, M. Senoh, N. Iwasa, S. I. Nagahama, T. Yamada, and T. Mukai, “Superbright green InGaN single-quantum-well-structure light-emitting diodes,” Japanese Journal of Applied Physics **34**(10B), L1332 (1995).

32 T. Mukai, D. Morita, and S. Nakamura, “High-power UV InGaN/AlGaN double-heterostructure LEDs,” Journal of Crystal Growth **189**, 778-781 (1998).

33 T. Mukai, and S. Nakamura, “Ultraviolet InGaN and GaN single-quantum-well-structure light-emitting diodes grown on epitaxially laterally overgrown GaN substrates,” Japanese Journal of Applied Physics **38**(10R), 5735 (1999).

34 H. M. Manasevit, and K. L. Hess, “The use of metalorganics in the preparation of semiconductor materials,” Journal of the Electrochemical Society **126**(11), 2031-2033 (1979).

35 S. Nakamura, “GaN growth using GaN buffer layer,” Japanese Journal of Applied Physics **30**(10A), L1705 (1991).

36 B. L. Liu, M. Lachab, A. Jia, A. Yoshikawaa, and K. Takahashi, “MOCVD growth of device-quality GaN on sapphire using a three-step approach,” Journal of Crystal Growth **234**(4), 637-645 (2002).

37 X. G. Zhang, B. Soderman, E. Armour, and A. Paranjpe, “Investigation of MOCVD growth parameters on the quality of GaN epitaxial layers,” Journal of Crystal Growth **318**(1), 436-440 (2011).

38 J. L. Zilko, *Handbook of Thin Film Deposition Processes and Techniques (Second Edition)* (Noyes, 2001), Chap. Metal organic chemical vapor deposition: technology and equipment.

39 P. R. Hageman, J. J. Schermer, and P. K. Larsen, “GaN growth on single-crystal diamond substrates by metalorganic chemical vapour deposition and hydride vapour deposition,” Thin Solid Films **443**(1-2), 9-13 (2003).

40 S. Nakamura, M. Senoh, and T. Mukai, “Highly p-typed Mg-doped GaN films grown with GaN buffer layers,” Japanese Journal of Applied Physics **30**(10A), L1708 (1991).

41 H. Fu, X. Zhang, K. Fu, H. Liu, S. R. Alugubelli, X. Huang, H. Chen, I. Baranowski, T. H. Yang, K. Xu, F. A. Ponce, B. Zhang, and Y. Zhao, “Demonstration of nonpolar m-plane vertical GaN-on-GaN pn power diodes grown on free-standing GaN substrates,” Applied Physics **18**(06), 05308 (2018).

42 C. D. Lee, V. Ramachandran, A. Sagar, R. M. Feenstra, D. W. Greve, W. L. Sarney, L. Salamanca-Riba, D.C. Look, S. Bai, W.J. Choyke, and R. P. Devaty, “Properties of GaN epitaxial layers grown on 6H-SiC (0001) by plasma-assisted molecular beam epitaxy,” Journal of Electronic Materials **30**(3), 162-169 (2001).

43 L. Zhang, J. Yu, X. Hao, Y. Wu, Y. Dai, Y. Shao, H. Zhang, and Y. Tian, “Influence of stress in GaN crystals grown by HVPE on MOCVD-GaN/6H-SiC substratem,” Scientific Reports **4**, 4179 (2014).

44 S. P. DenBaars, D. Feezell, K. Kelchner, S. Pimputkar, C. C. Pan, C. C. Yen, S. Tanaka, Y. Zhao, N. Pfaff, R. Farrell, M. Iza, S. Keller, U. Mishra, J. S. Speck, and S. Nakamura, “Development of gallium-nitride-based light-emitting diodes (LEDs) and laser diodes for energy-efficient lighting and displays,” Acta Materialia **61**(3), 945-951 (2013).

45 C. H. Tien, S. H. Chuang, H. M. Lo, S. Tasi, C. L. Wu, S. L. Ou, and D. S. Wuu, “ITO/nano‐Ag plasmonic window applied for efficiency improvement of near-ultraviolet light emitting diodes,” Physica Status Solidi (a) **214**(3), 0609 (2017).

46 S. H. Hong, C. Y. Cho, S. J. Lee, S. Y. Yim, W. Lim, S. T. Kim, and S. J. Park, “Localized surface plasmon-enhanced near-ultraviolet emission from InGaN/GaN light-emitting diodes using silver and platinum nanoparticles,” Optics Express **21**(3), 3138-3144 (2013).

47 R. Windisch, C. Rooman, S. Meinlschmidt, P. Kiesel, D. Zipperer, G. H. Döhler, B. Dutta, M. Kuijk, G. Borghs, and P. Heremans, “Impact of texture-enhanced transmission on high-efficiency surface-textured light-emitting diodes,” Applied Physics Letters **79**(15), 2315-2317 (2001).

48 T. N. Oder, K. H. Kim, J. Y. Lin, and H. X. Jiang, “III-nitride blue and ultraviolet photonic crystal light emitting diodes,” Applied Physics Letters **84**(4), 466-468 (2004).

49 M. Khizar, Z. Y. Fan, K. H. Kim, J. Y. Lin, and H. X. Jiang, “Nitride deep-ultraviolet light-emitting diodes with microlens array,” Applied Physics Letters **86**(17), 173504 (2005).

50 M. R. Krames, M. Ochiai-Holcomb, G. E. Höfler, C. Carter-Coman, E. I. Chen, I. H. Tan, P. Grillot, N. F. Gardner, H. C. Chui, J. W. Huang, S. A. Stockman, F. A. Kish, M. G. Craford, T. S. Tan, C. P. Kocot, M. Hueschen, J. Posselt, B. Loh, G. Sasser, and D. Collins, “High-power truncated-inverted-pyramid (Al x Ga 1-x) 0.5 In 0.5 P/GaP light-emitting diodes exhibiting > 50% external quantum efficiency,” Applied physics letters **75**(16), 2365-2367 (1999).

51 N. Lobo, H. Rodriguez, A. Knauer, M. Hoppe, S. Einfeldt, P. Vogt, M. Weyers, and M. Kneissl, “Enhancement of light extraction in ultraviolet light-emitting diodes using nanopixel contact design with Al reflector,” Applied Physics Letters **96**(8), 081109 (2010).

52 A. Fadil, Y. Ou, T. Zhan, K. Wu, D. Suyatin, W. Lu, P. M. Petersen, Z. Liu, and H. Ou, “Fabrication and improvement of nanopillar InGaN/GaN light-emitting diodes using nanosphere lithography,” Journal of Nanophotonics **9**(1), 093062 (2015).

53 R. H. Horng, D. S. Wuu, Y. C. Lien, and H. W. Lan, “Low-resistance and high-transparency Ni/indium tin oxide ohmic contacts to p-type GaN,” Applied Physics Letters **79**(18), 2925–2927 (2001).

54 S. N. Mohammad, “Contact mechanisms and design principles for nonalloyed ohmic contacts to n-GaN,” Journal of Aapplied Physics **95**(9), 4856-4865 (2004).

55 M. Funato, M. Ueda, Y. Kawakami, Y. Narukawa, T. Kosugi, M. Takahashi, and T. Mukai, “Blue, green, and amber InGaN/GaN light-emitting diodes on semipolar {11-22} GaN bulk substrates,” Japanese Journal of Applied Physics **45**(26), L659 (2006).

56 Y. C. Lin, S. J. Chang, Y. K. Su, T. Y. Tsai, C. S. Chang, S. C. Shei, C. W. Kuo, and S. C. Chen, “InGaN/GaN light emitting diodes with Ni/Au, Ni/ITO and ITO p-type contacts,” Solid-State Electronics **47**(5), 849-853 (2003).

57 H. W. Huang, C. C. Kao, J. T. Chu, H. C. Kuo, S. C. Wang, and C. C. Yu, “Improvement of InGaN-GaN light-emitting diode performance with a nano-roughened p-GaN surface,” IEEE Photonics Technology Letters **17**(5), 983-985 (2005).

58 T. Abbas, and L. Slewa, “Transmission line method (TLM) measurement of (metal/ZnS) contact resistance,” International Journal of Nanoelectronics and Materials **8**, 111-120 (2015).

59 J. K. Sheu, Y. K. Su, G. C. Chi, P. L. Koh, M. J. Jou, C. M. Chang, C. C. Liu, and W. C. Hung, “High-transparency Ni/Au ohmic contact to p-type GaN,” Applied Physics Letters **74**(16), 2340-2342 (1999).

60 J. K. Ho, C. S. Jong, C. C. Chiu, C. N. Huang, C. Y. Chen, and K. K. Shih, “Low-resistance ohmic contacts to p-type GaN,” Applied Physics Letters **74**(9), 1275-1277 (1999).

61 J. K. Ho, C. S. Jong, C. C. Chiu, C. N. Huang, K. K. Shih, L. C. Chen, F. R. Chen, and J. J. Kai, “Low-resistance ohmic contacts to p-type GaN achieved by the oxidation of Ni/Au films,” Journal of Applied Physics **86**(8), 4491-4497 (1999).

62 D. Qiao, L. S. Yu, S. S. Lau, J. Y. Lin, H. X. Jiang, and T. E. Haynes, “A study of the Au/Ni ohmic contact on p-GaN,” Journal of Applied Physics **88**(7), 4196-4200 (2000).

63 S. H. Chuang, C. Y. Lin, S. L. Ou, C. S. Tsung, C. H. Chen, and D. S. Wuu, “Improved UV LED performance using transparent conductive films embedded with plasmonic structures,” Light-Emitting Diodes: Materials, Devices, and Applications for Solid State Lighting XIX, International Society for Optics and Photonics, California, USA (2015).

64 T. Fujii, Y. Gao, R. Sharma, E. L. Hu, S. P. DenBaars, and S. Nakamura, “Increase in the extraction efficiency of GaN-based light-emitting diodes via surface roughening,” Applied Physics Letters **84**(6), 855-857 (2004).

65 M. H. Mustary, B. D. Ryu, M. Han, J. H. Yang, V. V. Lysak, and C. H. Hong, “Light enhancement of surface nano-textured GaN based light emittingdiodes using self-assembled Ni nano-masks,” Optik **127**, 1622-1626 (2016).

66 R. Dylewicz, A. Z. Khokhar, R. Wasielewski, and P. F. Rahman, “Nanostructured graded-index antireflection layer formation on GaN for enhancing light extraction from light-emitting diodes,” Applied Physics B **107**, 393–399 (2012).

67 Y. Ou, A. Fadil, and H. Ou, “Fabrication of InGaN/GaN nanopillar light-emitting diode arrays,” 3rd European-Asian Workshop on Light-Emitting Diodes, Lyngby, Denmark (2015).

68 T. Takeuchi, C. Wetzel, H. Amano, and I. Akasaki, “Piezoelectric Effect in GaInN/GaN Heterostructure and Quantum Well Structure,” Meijo University (2003).

69 A. Yildiza, F. Dagdelenb, S. Acarc, S. B. Lisesivdinc, M. Kasapc, Y. Aydogdub, and M. Bosid, “Stokes Shift and Band Gap Bowing in InxGa1− xN (0. 060≤ x≤ 0. 105) Grown by Metalorganic Vapour Phase Epitaxy,” Acta Physica Polonica A **113**(2), 731-739 (2008).

70 H. M. Ng, D. Doppalapudi, D. Korakakis, R. Singh, and T. D. Moustakas, “MBE growth and doping of III–V nitrides,” Journal of Crystal Growth **189**, 349-353 (1998).

71 J. K. Ho, C. S. Jong , C. C. Chiu, C. N. Huang, K. K. Shih, L. C. Chen, F. R. Chen, and J. J. Kai, “Low-resistance ohmic contacts to p-type GaN achieved by the oxidation of Ni/Au films,” Journal of Applied Physics **86**(8), 4491-4497 (1999).

72 H. Ishikawa, S. Kobayashi, Y. Koide, S. Yamasaki, S. Nagai, J. Umezaki, M. Koike, and M. Murakami, “Effects of surface treatments and metal work functions on electrical properties at p-GaN/metal interfaces,” Journal of Applied Physics **81**(3), 1315-1322 (1997).

73 J. S. Jang, I. S. Chang, H. K. Kim, T. Y. Seong, S. Lee, and S. J. Park, “Low-resistance Pt/Ni/Au ohmic contacts to p-type GaN,” Applied Physics Letters **74**(1), 70-72 (1999).

74 X. A. Cao, S. J. Pearton, F. Ren, and J. R. Lothian, “Thermal stability of W and WSi x contacts on p-GaN,” Applied Physics Letters **73**(7), 942-944 (1998).

75 G. G. Pethuraja, R. E. Welser, A. K. Sood, C. Lee, N. J. Alexander, H. Efstathiadis, P. Haldar, and J. L. Harvey, “Current-voltage characteristics of ITO/p-Si and ITO/n-Si contact interfaces,” Advances in Materials Physics and Chemistry **2**(2), 59-62 (2012).

76 M. Muztoba, and M. Rana, “Rectifying and Schottky characteristics of a-SixGe1− xOy with metal contacts,” Canadian Journal of Physics **92**(7/8), 606-610 (2014).

77 Z. Li, *The Source/Drain Engineering of Nanoscale Germanium-based MOS Devices* (Springer, 2016), Chap. Ge-based Schottky barrier height modulation technology.

78 S. Hwang, and J. Shim, “A method for current spreading analysis and electrode pattern design in light-emitting diodes,” IEEE Transactions on Electron Devices **55**(5), 1123-1128 (2008).

79 H. Y. Lee, K. H. Pan, C. C. Lin, Y. C. Chang, F. J. Kao, and C. T. Lee, “Current spreading of III-nitride light-emitting diodes using plasma treatment,” Journal of Vacuum Science & Technology B: Microelectronics and Nanometer Structures Processing, Measurement, and Phenomena **25**(4), 1280-1283 (2007).

80 B. H. Kong, H. K. Cho, M. Y. Kim, R. J. Choi, and B. K. Kim, “InGaN/GaN blue light emitting diodes using Al-doped ZnO grown by atomic layer deposition as a current spreading layer,” Journal of Crystal Growth **326**(1), 147-151 (2011).

81 J. K. Sheu, Y. K. Su, G. C. Chi, P. L. Koh, M. J. Jou, C. M. Chang, C. C. Liu, and W. C. Hung, “High-transparency Ni/Au ohmic contact to p-type GaN,” Applied Physics Letters **74**(16), 2340-2342 (1999).

82 Y.C. Lin, S.J. Chang, Y.K. Su, T.Y. Tsai, C.S. Chang, S.C. Shei, C.W. Kuo, and S.C. Chen, “InGaN/GaN light emitting diodes with Ni/Au, Ni/ITO and ITO p-type contacts,” Solid-State Electronics 47, 849–853 (2003).

83 Y. Geng, L. Guo, S. S. Xu, Q. Q. Sun, S. J. Ding, H. L. Lu, and D. W. Zhang, “Influence of Al doping on the properties of ZnO thin films grown by atomic layer deposition,” The Journal of Physical Chemistry C **115**(25), 12317-12321 (2011).

84 T. Minami, “Transparent conducting oxide semiconductors for transparent electrodes,” Semiconductor Science and Technology **20**(4), S35 (2005).

85 K. Schulze, B. Maennig, K. Leo, Y. Tomita, C. May, J. Hüpkes, E. Brier, E. Reinold,, and P. Bäuerle, “Organic solar cells on indium tin oxide and aluminum doped zinc oxide anodes,” Applied Physics Letters **91**(7), 073521 (2007).

86 B. Yaglioglu, H. Y. Yeom, R. Beresford, and D. C. Paine, “High-mobility amorphous In2O3-10 wt% ZnO thin film transistors,” Applied Physics Letters **89**(6), 062103 (2006).

87 S. Cornelius, M. Vinnichenko, N. Shevchenko, A. Rogozin, A. Kolitsch, and W. Möller, “Achieving high free electron mobility in ZnO: Al thin films grown by reactive pulsed magnetron sputtering,” Applied Physics Letters **94**(4), 042103 (2009).

88 S. M. Pan, R. C. Tu, Y. M. Fan, R. C. Yeh, and T. J. Hsu, “Enhanced output power of InGaN–GaN light-emitting diodes with high-transparency nickel-oxide–indium–tin-oxide ohmic contacts,” IEEE Photonics Technology Letters **15**(5), 646–648 (2003).

89 C. H. Kuo, S. J. Chang, Y. K. Su, R. W. Chuang, C. S. Chang, L. W. Wu, W. C. Lai, J. F. Chen, J. K. Sheu, H. M. Lo, and J. M. Tsai, “Nitride-based near-ultraviolet LEDs with an ITO transparent contact,” Materials Science and Engineering: B **106**(1), 69-72 (2004).

90 S. L. Ou, D. S. Wuu, S. P. Liu, Y. C. Fu, S. C. Huang, and R. H. Horng, “Pulsed laser deposition of ITO/AZO transparent contact layers for GaN LED applications,” Optics Express **19**(17), 16244-16251 (2011).

91 S. J. Pearton, D. P. Norton, K. Ip, Y. W. Heo, and T. Steiner, “Recent advances in processing of ZnO,” Journal of Vacuum Science & Technology B: Microelectronics and Nanometer Structures Processing, Measurement, and Phenomena **22**(3), 932-948 (2004).

92 L. Schmidt-Mende, and J. L. MacManus-Driscoll, “ZnO–nanostructures, defects, and devices,” Materials Today **10**(5), 40-48 (2007).

93 S. Ilican, Y. Caglar, M. Caglar, and B. Demirci, “Polycrystalline indium-doped ZnO thin films: preparation and characterization,” Journal of Optoelectronics and Advanced Materials **10**, 2592-2598 (2008).

94 Q. B. Ma, Z. Z. Ye, H. P. He, S. H. Hu, J. R. Wang, L. P. Zhu, Y. Z. Zhang, and B. H. Zhao, “Structural, electrical, and optical properties of transparent conductive ZnO: Ga films prepared by DC reactive magnetron sputtering,” Journal of Crystal Growth **304**(1), 64-68 (2007).

95 T. Minami, and T. Miyata, “Present status and future prospects for development of non-or reduced-indium transparent conducting oxide thin films,” Thin Solid Films **517**(4), 1474-1477 (2008).

96 S. Chu, J. H. Lim, L. J. Mandalapu, Z. Yang, L. Li, and J. L. Liu, “Sb-doped p-ZnO/Ga-doped n-ZnO homojunction ultraviolet light emitting diodes,” Applied Physics Letters **92**(15), 152103 (2008).

97 C. H. Kuo, C. L. Yeh, P. H. Chen, W. C. Lai, C. J. Tun, J. K. Sheu, and G. C. Chia, “Low operation voltage of nitride-based LEDs with Al-doped ZnO transparent contact layer,” Electrochemical and Solid-State Letters **11**(9), H269–H271 (2008).

98 P. H. Chen, Y. A. Chen, L. C. Chang, W. C. Lai, and C. H. Kuo, “Low operation voltage of GaN-based LEDs with Al-doped ZnO upper contact directly on p-type GaN without insert layer,” Solid-State Electronics **109**, 29-32 (2015).

99 K. C. Park, D. Y. Ma, and K. H. Kim, “The physical properties of Al-doped zinc oxide films prepared by RF magnetron sputtering,” Thin Solid Films **305**(1-2), 201-209 (1997).

100 B. Du Ahn, S. H. Oh, D. U. Hong, D. H. Shin, A. Moujoud, and H. J. Kim, “Transparent Ga-doped zinc oxide-based window heaters fabricated by pulsed laser deposition,” Journal of Crystal Growth **310**(14), 3303-3307 (2008).

101 C. H. Kuo, C. L. Yeh, P. H. Chen, W. C. Lai, C. J. Tun, J. K. Sheu, and G. C. Chi, “Low operation voltage of nitride-based LEDs with Al-doped ZnO transparent contact layer,” Electrochemical and Solid-State Letters **11**(9), H269-H271 (2008).

102 M. E. Fragala, G. Malandrino, M. M. Giangregorio, M. Losurdo, G. Bruno, S. Lettieri, L. S. Amato, and P. Maddalena, “Structural, Optical, and Electrical Characterization of ZnO and Al‐doped ZnO Thin Films Deposited by MOCVD,” Chemical Vapor Deposition **15**(10-12), 327-333 (2009).

103 H. Y. Liu, V. Avrutin, N. Izyumskaya, M. A. Reshchikov, Ü. Özgür, and H. Morkoç, “Highly conductive and optically transparent GZO films grown under metal-rich conditions by plasma assisted MBE,” physica status solidi (RRL)-Rapid Research Letters **4**(3-4), 70-72 (2010).

104 B. H. Kong, M. K. Choi, H. K. Cho, J. H. Kim, S. Baek, and J. H. Lee, “Conformal coating of conductive ZnO: Al films as transparent electrodes on high aspect ratio Si microrods,” Electrochemical and Solid-State Letters **13**(2), K12-K14 (2010).

105 J. O. Song, K. K. Kim, S. J. Park, and T. Y. Seong, “Highly low resistance and transparent Ni/ZnO ohmic contacts to p-type GaN,” Applied Physics Letters **83**(3), 479-481 (2003).

106 C. J. Tun, J. K. Sheu, B. J. Pong, M. L. Lee, M. Y. Lee, C. K. Hsieh, C. C. Hu, and G. C. Chi, “Enhanced light output of GaN-based power LEDs with transparent Al-doped ZnO current spreading layer,” IEEE Photonics Technology Letters **18**(1), 274-276 (2006).

107 H. K. Lee, D. H. Joo, Y. H. Ko, Y. Yeh, Y. P. Kim, and J. S. Yu, “Improved light extraction of GaN-based blue light-emitting diodes with ZnO nanorods on transparent Ni/Al-doped ZnO current spreading layer,” Japanese Journal of Applied Physics **51**(12R), 122102 (2012).

108 J. O. Song, K. K. Kim, S. J. Park, and T. Y. Seong, “Highly low resistance and transparent Ni/ZnO ohmic contacts to p-type GaN,” Applied Physics Letters **83**(3), 479-481 (2003).

109 S. P. Jung, D. Ullery, C. H. Lin, H. P. Lee, J. H. Lim, D. K. Hwang, J. Y. Kim, E. J. Yang, and S. J. Park, “High-performance GaN-based light-emitting diode using high-transparency Ni/Au/Al-doped ZnO composite contacts,” Applied Physics Letters **87**(18), 181107 (2005).

110 B. J. Kim, M. A. Mastro, J. Hite, C. R. Eddy, and J. Kim, “Transparent conductive graphene electrode in GaN-based ultra-violet light emitting diodes,” Optics Express **18**(22), 23030-23034 (2010).

111 T. H. Seo, T. S. Oh, S. J. Chae, A. H. Park, K. J. Lee, Y. H. Lee, and E. K. Suh, “Enhanced light output power of GaN light-emitting diodes with graphene film as a transparent conducting electrode,” Japanese Journal of Applied Physics **50**(12R), 125103 (2011).

112 B. J. Kim, C. Lee, Y. Jung, K. H. Baik, M. A. Mastro, J. K. Hite, C. R. Eddy, and J. Kim, “Large-area transparent conductive few-layer graphene electrode in GaN-based ultra-violet light-emitting diodes,” Applied Physics Letters **99**(14), 143101 (2011).

113 B. J. Kim, C. Lee, M. A. Mastro, J. K. Hite, C. R. Eddy, F. Ren, S. J. Pearton, and J. Kim, “Buried graphene electrodes on GaN-based ultra-violet light-emitting diodes,” Applied Physics Letters **101**(3), 031108 (2012).

114 J. P. Shim, T. H. Seo, J. H. Min, C. M. Kang, E. K. Suh, and D. S. Lee, “Thin Ni film on graphene current spreading layer for GaN-based blue and ultra-violet light-emitting diodes,” Applied Physics Letters **102**(15), 151115 (2013).

115 D. Xu, Z. Deng, Y. Xu, J. Xiao, C. Liang, Z. Pei, and C. Sun, “An anode with aluminum doped on zinc oxide thin films for organic light emitting devices,” Physics Letters A **346**(1-3), 148-152 (2005).

116 H. Kim, A. Pique, J. S. Horwitz, H. Murata, Z. H. Kafafi, C. M. Gilmore, and D. B. Chrisey, “Effect of aluminum doping on zinc oxide thin films grown by pulsed laser deposition for organic light-emitting devices,” Thin Solid Films **377**, 798-802 (2000).

117 H. Kim, C. M. Gilmore, J. S. Horwitz, A. Piqué, H. Murata, G. P. Kushto, R. Schlaf, Z. H. Kafafi, and D. B. Chrisey, “Transparent conducting aluminum-doped zinc oxide thin films for organic light-emitting devices,” Applied Physics Letters **76**(3), 259-261 (2000).

118 S. M. Choi, S. H. Jhi, and Y. W. Son, “Effects of strain on electronic properties of graphene. Physical Review,” Physical Review B **81**(8), 081407 (2010).

119 W. C. Lai, C. N. Lin, Y. C. Lai, P. Yu, G. C. Chi, and S. J. Chang, “GaN-based light-emitting diodes with graphene/indium tin oxide transparent layer,” Optics Express **22**(102), A396-A401 (2014).

120 S. A. Khayatian, A. Kompany, N. Shahtahmassebi, and A. K. Zak, “Preparation and characterization of Al doped ZnO NPs/graphene nanocomposites synthesized by a facile one-step solvothermal method,” Ceramics International **42**(1), 110-115 (2016).

121 W. Wang, T. Ai, W. Li, R. Jing, Y. Fei, and X. Feng, “Photoelectric and Electrochemical Performance of Al-Doped ZnO Thin Films Hydrothermally Grown on Graphene-Coated Polyethylene Terephthalate Bilayer Flexible Substrates,” The Journal of Physical Chemistry C **121**(50), 28148-28157 (2017).

122 K. Xu, Y. Xie, H. Ma, Y. Du, F. Zeng, P. Ding, Z. Gao, C. Xu, and J. Sun, “ZnO nanorods/graphene/Ni/Au hybrid structures as transparent conductive layer in GaN LED for low work voltage and high light extraction,” Solid-State Electronics **126**, 5-9 (2016).

123 A. Crovetto, T. S. Ottsen, E. Stamate, D. Kjær, J. Schou, and O. Hansen, “On performance limitations and property correlations of Al-doped ZnO deposited by radio-frequency sputtering,” Journal of Physics D: Applied Physics **49**(29), 295101 (2016).

124 A. C. Ferrari, J. C. Meyer, V. Scardaci, C. Casiraghi, M. Lazzeri, F. Mauri, S. Piscanec, D. Jiang, K. S. Novoselov, S. Roth, and A. K. Geim, “Raman spectrum of graphene and graphene layers,” Physical Review Letters **97**(18), 187401 (2006).

125 Z. Ni, Y. Wang, T. Yu, and Z. Shen, “Raman spectroscopy and imaging of graphene,” Nano Research **1**(4), 273-291 (2008).

126 J. D. Carey, L. L. Ong, and S. R. P. Silva, “Formation of low-temperature self-organized nanoscale nickel metal islands,” Nanotechnology **14**(11), 1223-1227 (2003).

127 F. Niklaus, G. Stemme, J. Q. Lu, and R. J. Gutmann. “Adhesive wafer bonding,” Journal of Applied Physics **99**(3), 031101 (2006).

128 G. Yacobi, S. Martin, K. Davis, A. Hudson, and M. Hubert, “Adhesive bonding in microelectronics and photonics,” Journal of Applied Physics **91**(10), 6227-6262 (2002).

129 F. Niklaus, H. Andersson, P. Enoksson, and G. Stemme, “Low temperature full wafer adhesive bonding of structured wafers,” Sensors and Actuators A: Physical **92**(1-3), 235-241 (2001).

130 F. Bu, Q. Ma, and Z. Wang, “Delamination of bonding Interface between benzocyclobutene (BCB) and silicon dioxide/silicon nitride,” Microelectronics Reliability **65**, 225-233 (2016).

131 B. Bilenberg, T. Nielsen, B. Clausen, and A. Kristensen, “PMMA to SU-8 bonding for polymer based lab-on-a-chip systems with integrated optics,” Journal of Micromechanics and Microengineering **14**(6), 814 (2004).

132 S. Li, C. B. Freidhoff, R. M. Young, and R. Ghodssi, “Fabrication of micronozzles using low-temperature wafer-level bonding with SU-8,” Journal of Micromechanics and Microengineering **13**(5), 732 (2003).

133 X. Zhang, O. Adelegan, F. Y. Yamaner, and Ö. Oralkan, “An optically transparent capacitive micromachined ultrasonic transducer (CMUT) fabricated using SU-8 or BCB adhesive wafer bonding,” Ultrasonics Symposium, 2017 IEEE International, Washington, USA (2017).

134 T. S. Chang, T. C. Chang, P. T. Liu, S. W. Tsao, and F. S. Yeh, “Investigation of the low dielectric siloxane-based hydrogen silsesquioxane (HSQ) as passivation layer on TFT-LCD,” Thin Solid Films **516**(2-4), 374-377 (2007).

135 J. N. Kuo, C. C. Hsieh, S. Y. Yang, and G. B. Lee, “An SU-8 microlens array fabricated by soft replica molding for cell counting applications,” Journal of Micromechanics and Microengineering **17**(4), 693 (2007).

136 Q. Wang, A. Z. Zhang, A. Bergström, V. Z. Huo, S. Almqvist, W. Kaplan, and J. Y. Andersson, “Micro-optical elements functioning in non-visible spectral range,” Micro-Optics, International Society for Optics and Photonics **7716**, 771609 (2010).

137 St. Trellenkamp, J. Moers, A. Van der Hart, P. Kordoš, and H. Lüth, “Patterning of 25-nm-wide silicon webs with an aspect ratio of 13,” Microelectronic Engineering **67**, 376-380 (2003).
138 Y. Chen, J. Tao, X. Zhao, Z. Cui, A. S. Schwanecke, and N. I. Zheludev, “Nanoimprint lithography for planar chiral photonic meta-materials,” Microelectronic Engineering **78**, 612-617 (2005).
139 D. Lauvernier, S. Garidel, C. Legrand, and J. P. Vilcot, “Realization of sub-micron patterns on GaAs using a HSQ etching mask,” Microelectronic Engineering **77**(3-4), 210-216 (2005).
140 K. K. Ryu, J. W. Chung, B. Lu, and T. Palacios, “Wafer bonding technology in nitride semiconductors for applications in energy and communications,” ECS Transactions **33**(4), 125-135 (2010).
141 H. Chen, and R. E. Tecklenburg, “Characterization of low and intermediate molecular weight hydrogen silsesquioxanes by mass spectrometry,” The Journal of the American Society for Mass Spectrometry **17**(10), 1438-1442 (2006).
142 J. W. Chung, E. Piner, and T. Palacios, “N-face GaN/AlGaN transistors through substrate removal,” IEEE Device Research Conference 2008, California, USA (2008).
143 J. W. Chung, E. L. Piner, and T. Palacios, “N-face GaN/AlGaN HEMTs fabricated through layer transfer technology,” IEEE Electron Device Letters **30**(2), 113-116 (2009).
144 S. Sergent, M. Arita, S. Kako, K. Tanabe, S. Iwamoto, and Y. Arakawa, “High-Q AlN photonic crystal nanobeam cavities fabricated by layer transfer,” Applied Physics Letters **101**(10), 101106 (2012).
145 S. Lis, R. Dylewicz, J. Myśliwiec, A. Miniewicz, and S. Patela, “Application of flowable oxides in photonics,” Materials Science-Poland **26**(1), 189-194 (2008).
146 W. S. Wong, and T. Sands, “InxGa1− xN light emitting diodes on Si substrates fabricated by Pd–In metal bonding and laser lift-off,” Applied Physics Letters **77**(18), 2822-2824 (2000).
147 https://en.wikipedia.org/wiki/Thermal_expansion
148 J. B. Casady, and R. W. Johnsonm, “Status of silicon carbide (SiC) as a wide-bandgap semiconductor for high-temperature applications: A review,” Solid-State Electronics **39**(10), 1409-1422 (1996).
149 W. Xie, J. A. Cooper, and M. R. Melloch, “Monolithic NMOS digital integrated circuits in 6H-SiC,” IEEE Electron Device Letters **15**(11), 455-457 (1994).

Acronyms

ALD	Atomic layer deposition
AlGaN	Aluminum gallium nitride
AZO	Aluminum-doped zinc oxide
CRI	Color rendering index
CSL	Current spreading layer
DAP	Donor-acceptor-pair
DI	Deionized
DUV	Deep ultraviolet
EL	Electroluminescence
EQE	External quantum efficiency
f-SiC	Fluorescent silicon carbide
FWHM	Full width at half maximum
GaN	Gallium nitride
HCl	Hydrogen chloride
HF	Hydrofluoric acid
HSQ	Hydrogen silsesquioxane
ICP	Inductively coupled plasma
InGaN	Indium gallium nitride

IQE	Internal quantum efficiency
ITO	Indium tin oxide
LED	Light emitting diode
LEE	Light extraction efficiency
MIBK	Methyl isobutyl ketone
MOCVD	Metalorganic chemical vapor deposition
MQW	Multiple quantum well
NUV	Near ultraviolet
PECVD	Plasma-enhanced chemical vapor deposition
RIE	Reactive-ion etching
SBH	Schottky barrier height
SEM	Scanning electron microscopy
SiC	Silicon carbide
SLG	Single layer graphene
SQW	Single quantum well
TCO	Transparent conductive oxide
TLM	Transfer line method
TMA	Trimethylaluminum
TMG	Trimethylgallium
TMIn	Trimethylindium
UV	Ultraviolet
VSI	Vertical scanning interferometry
YAG	Yttrium aluminum garnet
ZnO	Zinc oxide

Appendix A. Standard fabrication of GaN based LEDs

Step	Equipment	Procedure
1 Preparation		
1.1 Wafer cutting	Diamond pen	
1.2 Wafer cleaning	Bench	Step 1: 5 min in Acetone Step 2: 1 min in IPA Step 3: Rinse by DI water Step 4: Blow dry by N_2 gun
2 Lithography – Mesas		
2.1 SiO_2 deposition	PECVD 4	Aim: 300 nm SiO_2 Recipe: LF SiO_2 with wafer clean Rate: 78 nm/min Gases: N_2O 1420 sccm SiH_4 12 sccm N_2 392 sccm Power: 60 W Pressure: 550 Throttle Substrate temperature: 300℃
2.2 Surface treatment	Oven: HMDS-2	Step 1: 5 min prebake time Step 2: 5 min HMDS prime time
2.3 Coat wafers	Spin Coater: Labspin 02	Aim: 1.6 µm AZ5214E Step 1: 400 rpm, 1000 rpm/sec, 5 sec Step 2: 4000 rpm, 1000 rpm/sec, 30 sec Step 3: Bake at 90 ℃ for 90 sec
2.4 Exposure	Aligner MA 6-2	Mode: Vacuum contact Exposure time: 10 sec

		Intensity: 13 mW/cm^2 Mask: Mesas
2.5 Develop	Developer: TMAH Manual	Chemical: TMAH Time: 30 sec Recipe name: SP 30s
2.6 Residual removal	III-V Plasma Asher	Recipe: O_2 plasma Time: 2 min Power: 40 W
2.7 SiO_2 wet etch	SiOetch	Aim: Etch of 300 nm exposed SiO_2 Time: 2 min
2.8 Resist removal	III-V Plasma Asher	Step 1: 5 min Acetone clean Step 2: Rinse by DI-water Step 3: 20 min O_2 plasma at 100 W
2.9 GaN etch	III-V ICP	Gases: Cl_2 27 sccm BCl_3 3 sccm Ar 3 sccm Coil power: 400 W Platen power: 75 W Pressure: 4 mTorr GaN etch rate: 345 nm/min SiO_2 etch rate: 44 nm/min Time: 245 sec (for around 1400 nm)
2.10 SiO_2 Removal	5% HF	Time: 10 min Rate: 190 nm/min
2.11 Post-etch surface treatment	Furnace of Rapid Thermal Annealing	Step 1: Temperature: 500 ℃ Ramping time: 1 min Annealing time: 10 min Gas: N_2 150 sccm Recipe: llin500N_2 Step 2: 37%-38% HCl: immersion of 60 min
3. Lithography – Current Spreading Layers		
3.1 Coat wafers	Spin Coater: Manual All Resist	Aim: 2 µm N-LOF 2020 Step 1: 3800 rpm, 2000 rpm/sec, 30 sec Step 2: Bake at 110 °C for 1 min
3.2 Exposure	Aligner MA 6-2	Mode: Vacuum contact Exposure time: 10 sec Intensity: 13 mW/cm^2 Mask: Current spreading layers
3.3 Post-exposure bake	Hotplate	Bake at 110 °C for 1 min
3.4 Develop	Developer: TMAH Manual	Chemical: AZ 726 MIF (2.38% TMAH) Time: 30 sec Recipe name: SP 30s

3.5 Metal deposition	Physimeca (E-beam Evaporation)	Materials: Step 1: 10 nm Ni with a rate of 5Å/s Step 2: 40 nm Au with a rate of 10Å/s Pressure: 1.0×10^{-6} mbar
3.6 Lift-off	Fumehood	Chemical: Remover 1165 Time of ultrasonic bath: 15 min Rinse by DI-water
3.7 Thermal annealing	Furnace of Rapid Thermal Annealing	Temperature: 525 ℃ Ramping time: 1 min Annealing time: 5 min Gas: air Recipe: llin525air
4 Lithography – Pads		
4.1 Coat wafers	Spin Coater: Manual All Resist	Aim: 2 µm N-LOF 2020 Step 1: 3800 rpm, 2000 rpm/sec, 30 sec Step 2: Bake at 110 °C for 1 min
4.2 Exposure	Aligner MA 6-2	Mode: Vacuum contact Exposure time: 10 sec Intensity: 13 mW/cm^2 Mask: Pads
4.3 Post-exposure bake	Hotplate	Bake at 110 °C for 1 min
4.4 Develop	Developer: TMAH Manual	Chemical: AZ 726 MIF (2.38% TMAH) Time: 30 sec Recipe name: SP 30s
4.5 Metal deposition	Physimeca (E-beam Evaporation)	Materials: Step 1: 30 nm Ti with a rate of 5Å/s Step 2: 200 nm Au with a rate of 10Å/s Pressure: 1.0×10^{-6} mbar
4.6 Lift-off	Fumehood	Chemical: Remover 1165 Time of ultrasonic bath: 15 min Rinse by DI-water